Numerical and Experimental Investigation of Heat Transfer Enhancement in Flat Plate Collector Using Nanofluids

By: **Tiko Rago Desisa**

A Thesis Submitted to the Department of Thermal and Aerospace Engineering

School of Mechanical, Chemical and Material Engineering

A thesis submitted to the School of Graduate Studies of Adama Science and Technology University in partial fulfillment of the Degree of Masters of Science in Thermal and Aerospace Engineering

Adama Science and Technology University

Adama, Ethiopia

September 2019

Numerical and Experimental Investigation of Heat Transfer Enhancement in Flat Plate Collector Using Nanofluids

By**: Tiko Rago Desisa**

Advisor**: Dr.V.Chandraprabu**

A Thesis Submitted to the Department of Thermal and Aerospace Engineering

School of Mechanical, Chemical and Material Engineering

A thesis submitted to the School of Graduate Studies of Adama Science and Technology University in partial fulfillment of the Degree of Masters of Science in Thermal and Aerospace Engineering

Adama Science and Technology University

Adama, Ethiopia

September 2019

DECLARATION

Firstly, I want to declare that this thesis is the result of my own work and that all source or materials used for this thesis have been duly acknowledged. This thesis is submitted in partial fulfillment of the requirements for Master's Degree in Thermal and Aerospace Engineering at Adama Science and Technology University and to be made available at the University's Library under the rule of the Library. I confidently declare that this thesis has not been submitted to any other institutions anywhere for the award of any academic degree, diploma, or certificate.

------------------------------	----------------------	---------------------
Student	Signature	Date

This is to certify that the above statement made by the candidate is correct to the best of our knowledge and belief. This has been submitted for examination with our approval.

------------------------------	----------------------	---------------------
Advisor	Signature	Date

Adama Science and Technology University

School Of Mechanical, Chemical and Material Engineering

Thermal and Aerospace Engineering Program

Approval of Board of Examiners

We, the undersigned, members of the Board of Examiners of the final open defense by Tiko Rago Desisa have read and evaluated his thesis entitled "Numerical and Experimental Investigation of Heat Transfer Enhancement in Flat Plate Collector Using Nanofluids" and examined the candidate. This is, therefore, to certify that the thesis has been accepted in partial fulfillment of the requirement of the Degree of Master of science in Thermal Engineering.

------------------------------	----------------------	---------------------
Chairperson	Signature	Date
------------------------------	----------------------	---------------------
Internal examiner	Signature	Date
------------------------------	----------------------	---------------------
External examiner	Signature	Date

ACKNOWLEDGMENT

First, I would like to give an Enormous thanks to the Almighty God who gives me patient, courage and wisdom to finish this work.

Next, I would like to thank my thesis advisor Dr. V.Chandraprabu. His office was always open whenever I run into a trouble spot or had a question about my research or writing. He consistently allowed this paper to be my own work, but steered me in the right the direction whenever he thought I needed it. also I have great thanks for Mr.Paouls.

I have great thanks for all 'Adama Science and Technology University technicians' and workers for their continuous support in preparing necessary material, allowing work place, and guidance in my work.additionally I whould like to aknowledge Adama Science and Technology University Material Science Department for their support.

Finally yet importantly, I would like to thank my family and friends who were always besides me and played a great role in completion of my work.

ABSTRACT

Solar energy collectors are special kind of heat exchangers that transform solar radiation energy to internal energy of the transport medium. Researches in heat transfer have carried out over the previous several decades, leading to the development of the currently used heat transfer enhancing techniques in solar flat plate collector. This study uses different nanofluids to enhance the heat transfer due to their high thermal conductivity. The solar radiation estimation (for Adama, Ethiopia) is done using MS excel, and The CFD model used to simulate the steady, laminar flow process occur in solar flat plate collector using ANSYS fluent 17.2. The pressure velocity coupling is done using the SIMPLE algorithm and discretization is made using second order upwind scheme. The Nusselt number (heat transfer coefficient) of different nanofluids is analyzed and compared to the SFPC using water. The numerical simulation results shows for 3% volume concentration of Si_2O, Ti_2O, Al_2O_3 *and CuO, 0.6887%, 3.3011%, 3.3429%, 4.1423% increment in Nusselt number is achieved respectively. The CuO nanoparticle has greater improvement than other nanoparticles and* Si_2O *has lower improvement than the other nanoparticles. In the same way the experimental results shows the addition of nanofluids increases the thermal efficiency of the flat plate collector. Finally, the result shows the pressure drop is insignificant in all cases.*

Keywords: *solar radiation; heat transfer; CFD; nanoparticles; nanofluids; SFPC*

CONTENTS

LISTS OF FIGURES

LISTS OF TABLES

NOMENCLATURE

Acronym

SFPC	Solar Flat Plate Collector
SWH	Solar Water Heater
GSR	Global Solar Radiation
NMAE	Normalized Mean Absolute Error
CMSC	Coordinate Metrology Systems Conference
CSM	Chemical Solution Method
CPSC	Compound Parabolic Solar Concentrator
ETC	Evacuated-Tube Collector
GRP	Glass Reinforced Plastic
EPDM	Ethylene Propylene Diene Monomer
PVC	Polyvinylchloride
DSG	Direct Steam Generator
PH	a numeric scale specifies acidity and basicity of aqueous solution
MWCNT	Multi-walled Carbon Nanotube
AGI	Absorber Galvanized Iron plate with pipe

Symbols

A	surface area of solar collector (m^2)
C	the specific heat coefficient of fluid (J/kg K)
It	global solar radiation (W/m^2)
t_b	thickness of back of collector
K	thermal conductivity (W/ (Km))
L	length of the tube (m)
$\dot{m}$	Mass flow rate of fluid flow (kg/s)
Nu	Nusselt number
P	fluid pressure (pa)
Pr	Prandtl number
Q	rate of useful energy gained (W)
t	time (s)
T	air temperature (K)
T	inlet fluid temperature of solar collector (K)
T	outlet fluid temperature of solar collector (K)
u, v, w	the velocity vectors (m/s)
V	the wind speed (m/s)
Nu	length of flat plate collector (m)
F	view factor
R_b	tilt factor

D	diameter (m)
t	thickness (m)
r	distance between tubes (m)
t	back insulation thickness (m)
E	emittance

Greek Letters

$\boldsymbol{\delta}$	Declination angle
$\boldsymbol{\alpha}$	Absorptivity
$\propto$	Thermal diffusivity (m^2/s)
$\boldsymbol{\rho_g}$	Ground Reflectance
$\boldsymbol{\rho}$	Density (kg/m^3)
τ	Transmissivity
φ	Latitude (^{o})
$\emptyset$	Volume fraction of nanoparticles in nanofluid
$\boldsymbol{\mu}$	The viscosity of the fluid (Pa-s)
$\boldsymbol{\beta}$	Tilt angle (^{o})

Subscripts

s	sunshine
o	extraterrestrial
sc	solar constant
d	diffuse
b	beam, back
ag	air gap
nf	nanofluids
bf	base fluid
np	nanoparticle
m	mean
fd	fully developed flow
w	wall
eff	effective
p	pressure, plate
u	useful
a	air
i	inlet
o	outlet
c	collector
g	glass

CHAPTER ONE

INTRODUCTION

Energy is one of an important entity for the economic development of one country. The demand for energy is significantly increasing with increases in population and the rapid development of the world's economy (Bozorgan, 2015). As a result, the price of energy from conventional sources such as fossil fuels and nuclear power, are escalating through time. Nowadays, about 80 percent of the global primary energy demand is coming from fossil fuels, which are limited and thus become too expensive to exploit in the future (Uyan, 2013). While a majority of the world's energy supply is generated from fossil fuels, the release of fossil carbon into the atmosphere has a tremendous impact on the global climate. Hence, in order to overcome this problem and meet the future demand for energy, renewable energy resources should be utilized to an optimum level. Since solar energy is the most abundant source, more focus has to be on it.

Ethiopia, because of its proximity to the equator, receives adequate sunshine throughout the year. The average daily radiation intensity on the horizontal surface is 5.2 kWh/m^2. Hence, Ethiopia can use solar energy for domestic and commercial applications (Bekele, 2007).

Ethiopia has a total energy consumption of around 40,000 GWh, in which 92% are consumed by domestic appliances, 4% by the transport sector and 3% by industry. Most of the energy supply thereby is covered by bioenergy, which in case of domestic use is usually stemming from unsustainable sources.

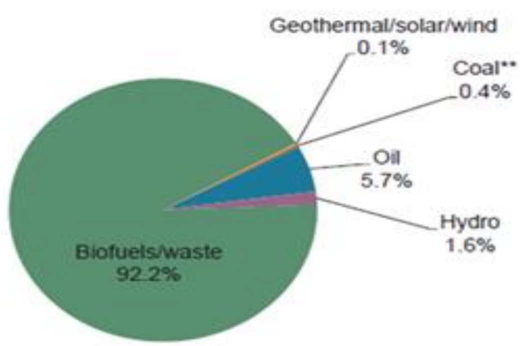

Figure 1.1 Share total energy supply in Ethiopia in 2014 (International Energy Agency, 2014).

The Ethiopian Government took considerable action under the course of the Ethiopian Integrated Housing Development Program (I-HDP). In this grant program, the government constructed thousands of condominium houses in different towns in the country. If we take Addis Ababa city only, in the last two-registration program 2005 and 2013 974,835 residents registered for the condominium houses, and within 12 years 176,065.00 houses are constructed and transferred to beneficiaries (AAHCPO, 2016). Each household uses the electric water heater for washing, shower, and other purposes, which result in a high consumption of electricity. This problem can be reduced solved by replacing each household electric water heater by solar flat plate collector (SFPC) and save money.

In another angle, substituting the solar energy instead of coal reduce the CO_2 and SO_2 emissions significantly. Coal-fired power plants are selected for the comparison of energy and pollution in this study, because the energy that can be generated and the amount of pollutants released from coal are known. When 1 kg of coal burned, 29.306 MJ of energy can be generated, and concurrently, greenhouse gases, such as CO_2 and SO_2, are released. The CO_2 and SO_2 generated per 1 kg of coal burned are 2.93 kg and 0.0123 kg, respectively Faizal et al., (2014). The graph shown in Fig. 1.2 is per capital of CO_2 emmision of Ethiopia.

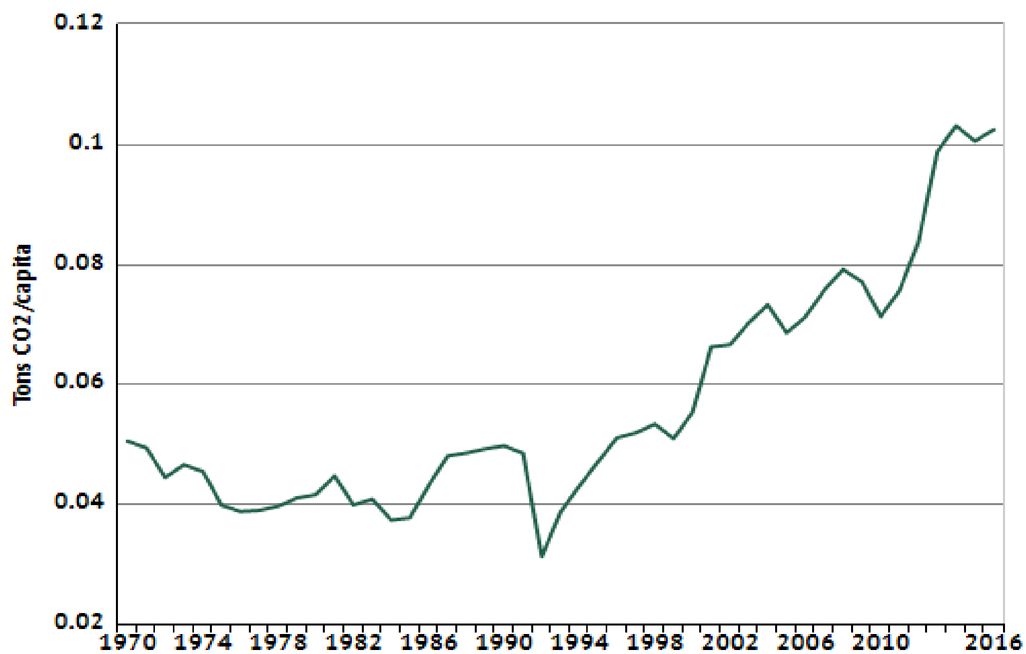

Figure 1.2. Ethiopia's CO_2 emissions per capita (Knoema Corporation{US}, {1970-2016}).

The CO_2 emmisions inceasing due to the fact that the consumption of fossil fuels are increasing enormously. Now a day's solar systems produce energy by converting the renewable source of solar radiation into useful heat or electricity. Heat transfer enhancement in solar devices is one of the key issues of energy saving and compact designs. Researches in heat transfer have carried out over the previous several decades, leading to the development of the currently used heat transfer enhancing techniques in solar flat plate collector. Using nanofluids as working fluid in solar collectors is one method of enhancing the heat transfer in solar collectors.

Nanofluids are two-phase fluids engineered by mixing nanometer-sized nanoparticles with sizes ranging below 100 nm in base fluids (**Das et al.,** 2008). At present time Nano fluids plays vital role in various thermal applications such as automotive industries, heat exchangers and solar power generation etc. There are different types of nano fluids prepared by dispersing and oscillating TiO_2, Al_2O_3, ZnO, Ag, Cu, CuO, SiO_2, and Fe_3O_4 graphite nanoparticles, carbon nanotubes into the base fluids Natarajan, (2009).

1.1.0 Solar water heating system

Solar energy collectors are special kind of heat exchangers that transform solar radiation energy to internal energy of the transport medium. This is a device which absorbs the incoming solar radiation, converts it into heat, and transfers this heat to a fluid (usually air, water, or oil) flowing through the collector. The solar energy thus collected is carried from the circulating fluid either directly to the hot water or space conditioning equipment or to a thermal energy storage tank (Dimitrios, 2015).

1.1.1 Types of solar collectors

There are two types of solar collectors: non-concentrating or stationary and concentrating. A non-concentrating collector has the same area for intercepting and for absorbing solar radiation, whereas a sun-tracking concentrating solar collector usually has concave reflecting surfaces to intercept and focus the sun's beam radiation to a smaller receiving area, thereby increasing the radiation flux (Mohamed, 2016). The classification of solar collectors is shown in Fig. 1.3 in block diagram form.

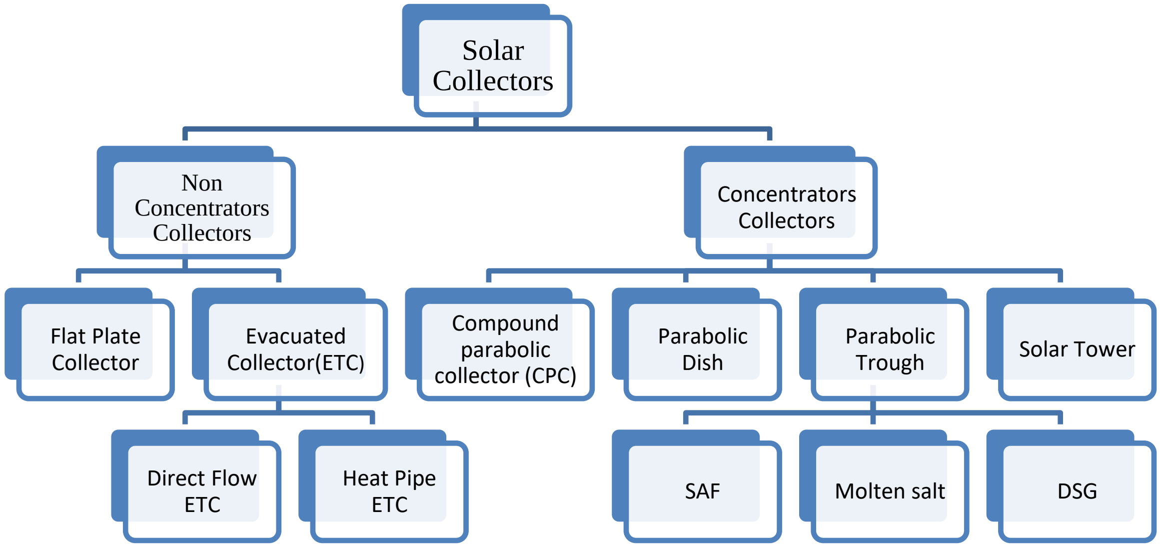

Figure 1.3. Classification chart of solar collectors (https://images.search.yahoo.com/yhs/search?p=, n.d.)

There are different types of collectors based on the motion of collector and range of temperature. The capacity of solar collectors are shown in Table 1.1.

Table 1.1 Solar collector's capacity (http://slideplayer.com/slide/images/Types+of+solar+collectors., n.d.)

No.	Motion	Collector	Absorber Type	Concentration Ratio	Indicative temperature range (°C)
1.	Stationary	Flat plate collector	Flat	1	30 – 80
		Compound parabolic collector	Tubular	1 – 5	60 – 240
2.	Single-axis tracking			5 – 15	60 – 300
		Linear Fresnel reflector (LFR)	Tubular	10 – 40	60 – 250
		Parabolic collector (PTC)	Tubular	15 – 45	60 – 300
		Cylindrical trough collector (CTC)	Tubular	10 – 50	60 – 300
3.	Two axes tracking	Parabolic dish reflector(PDR)	Point	100 – 1000	100 – 500
		Heliostat field collector(HFC)	Point	100 – 1500	150 – 2000

Table 1.1 shows the flate plate collector is the low range water heating collector due to its lower concentration ratio. Whereas the heliostat field collector (HFC) is the high range water heating collector with high concentration ratio.

1.1.1.1 Flat plate collectors (FPC)

FPC is a device used to collect solar energy and transform into thermal energy (low-grade energy) by using water as working fluid, and medium temperature range is below 100℃. They use both beam and diffuse solar radiation, do not require tracking mechanism and require little maintenance. They are mechanically simpler than concentrating collectors.

The principle behind a flat collector is simple. If a metal sheet is exposed to solar radiation, the temperature will rise until the rate at which energy is received is equal to the rate at which heat is lost from the plate; this temperature is termed as the ‘equilibrium’ temperature. If the back of the plate is protected by a heat insulating material, and the exposed surface of the plate is painted black and is coved by one or two glass sheets, then the equilibrium temperature will be much higher than that for the simple exposed sheet. This plate may be covered into a heat collector by adding a water circulating system, either by making it hollow or by soldering metal pipes to the surface, and transferring the heated liquid to a tank for storage.

FPC is usually fixed in position and require no tracking of the sun. The collector should be oriented directly towards the equator, facing south in the northern hemisphere and north in the southern. The optimum tilt angle of the collector is equal to the latitude of the location with angle variations of 10–158 more or less depending on the application (Mohamed, 2016).

The basic components of SFPC which are shown in Fig.1.4 are listed below:

- **Glazing cover**-transparent cover usually glass puts on the top the FPC.
- **Glazing frame**-used to hold the glass.
- **Absorber plate-**to harvest the solar radiation to gain heat and allowing efficient heat transfer to working fluid.
- **Fluid pipes/tubes-** facilitating the flow of working fluids.
- **Insulation** –minimize the heat loss from bottom and sides.

- **Casing -** A waterproof box surrounds the foregoing components and keeps them free from dust and moisture.

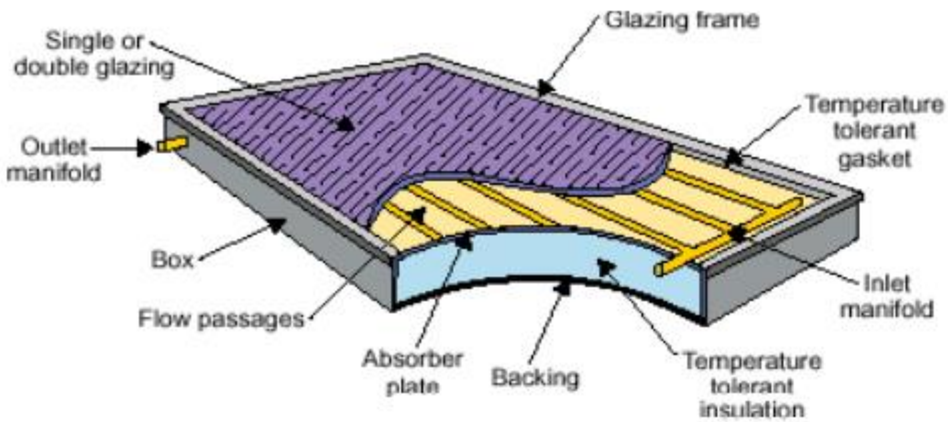

Figure 1.4. Flat plate solar collector (U.S.A Department of Energy)

1.1.1.2 Materials used in flat plate collectors

Glazing

The main purposes of glazing are:

- ✓ Transmit maximum solar radiation.
- ✓ Minimize upward heat loss from absorber plate to environment.
- ✓ Protecting the absorber plate from weather.

Transparent plastic is also generally used as glazing material in FPC. This plastic poses high short wave transmittance but because most of the plastic properties which cannot stand the ultra-violet radiation for a long time period, transparent plastic is unpopular as glazing material in flat plate collector. Crystal clear and window glass have highest transmittance of solar radiation as shown in Table 1.2. The ability of the glass makes it suitable as heat trap in the collector. Thus, window glass is suitable because it is widely used in local flat plate collector.

The most critical factors for the cover plate materials are:

1. Strength
2. Durability
3. Non-degradability

4. Cost
5. Solar-energy and thermal energy transmittance

Table 1.2. Transmittance of various glazing material. (Dimitrios, 2015)

No.	Material	Transmittance (τ)
1.	Crystal glass	0.91
2.	Window glass	0.85
3.	Acrylate, Plexiglass	0.84
4.	Polycarbonate	0.84
5	Polyester	0.84
6.	Polyamide	0.80

Table 1.2 shows list of different glass transmittance. The cost of the glass increase with increase in transmitivity. The polyamide glass has lower transmittance whereas crystal glass has higher transmittance. For this study the window glass is used for its better transmittance and proper cost.

Tubing

The pipework in a solar system must be able to withstand circulating fluid at temperatures up to 100°C without corroding. The most commonly used material is copper. Copper has good corrosion resistance. Stainless steel is also known to have excellent corrosion resistance but it is more expensive than copper. It has several advantages like lower thermal conductivity (leading to lower heat losses) lower thermal expansion coefficient and higher strength to mass ratio allowing the use of thinner sections (Dimitrios, 2015).

Copper is considered as fluid passageways tube material, because of the following reasons:

- Its higher thermal conductivity.
- High absorbance of material
- Low emissivity of material
- Suitability to high temperatures

- Higher corrosion resistant
- High durability and strength.
- Lower cost per the rate of heat energy transfer

Even though, copper is expensive compared to aluminum and stainless steel, copper is used in this paper due to its better physical and thermal properties. There are two types of tube configuration usually found in flat plate collector namely parallel and serpentine flow configuration.

Parallel configuration

The parallel tube as shown in Fig.1.5 is designed to transport working fluid from the bottom of the flat plate collector to the top of the flat plate collector. The fluids pressure is higher at the base of the collector and least at the top. If the top and bottom pipes are large, the pressure difference is moderated and the flow rate in each of the parallel pipes is more uniform (Canivan, 2009). Unfortunately, the flow rate is minimal at the center where most of the heat is concentrated. Other problems associated with this configuration are the cost and leaking problems. One small leak can cause catastrophic mess in experimentation and calculation (Billy, 2010).

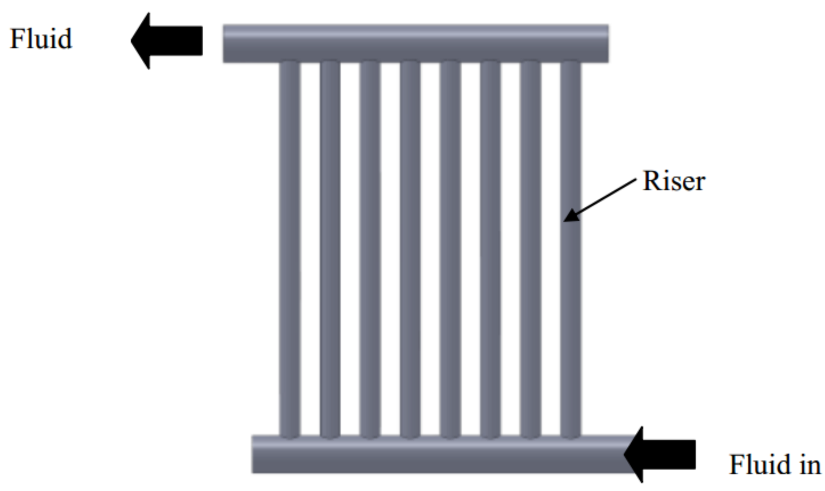

Figure 1.5. Parallel flow configuration (Canivan, 2009).

Serpentine configuration

The serpentine flow in Fig.1.6 below consists of one long continuous flexible tube so there is no problem with uniform flow rate. The working fluids flow continuously from bottom to the top of the collector. This results in steady heat transfer from the heat absorber to the working fluid. Since the flow rate of the fluid through the serpentine tube shown in Fig. 1.6 is uniform, the heat collection process is uniform (Billy, 2010).

Sometimes, serpentine configuration is used due to uniform fluid flow resulting uniform heat transfer from absorber plate to working fluid. Furthermore, serpentine configuration is easier to construct compare to parallel which have many welding joints. The probability of leaking in serpentine configuration is low compare to parallel configuration (Manickavasagan et al., 2002). However, there is significant pressure drop in pipe.

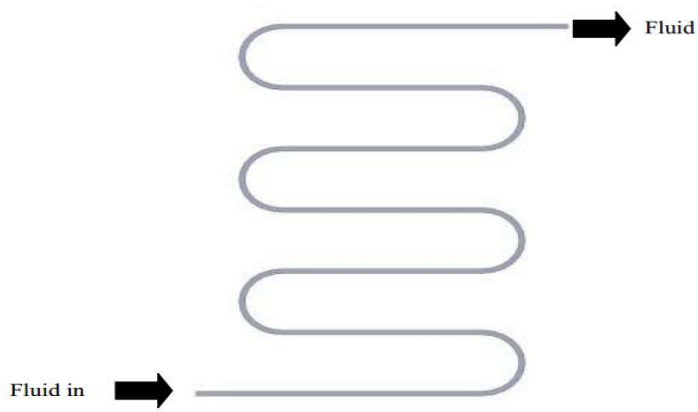

Figure 1.6. Serpentine tube configuration (Canivan, 2009)

Absorber material

The absorber is the central component of the solar collector. Heat transfer to the fluid depends on the thermal conductivity of the plate material and on the distance between fluid passageways. High thermal conductivity materials such as copper and aluminum can be economically used in plate and tubes, where heat conduction takes place along the plate (Billy, 2010). The thermal conductivities of different materials are given in Table 1.3.

Table 1.3. Thermal conductivities of absorber materials (Dimitrios, 2015)

Materials	Thermal conductivity ($Wm^{-1}K^{-1}$)
Copper	376
Aluminum	205
Mild steel	50
Stainless steel	24
Acrylic	0.2
Polyethylene	0.3-0.44
Polypropylene	0.2

The thermal conductivity of copper is greater than other materials given in Table 1.3. Collectors with selective coating have high efficiency either in increased operating temperature of the collector. Collector heat losses can be substantially reduced by the use of selective coatings, which have a high absorbance greater than 0.95 for solar radiation, but a low emissivity of around 0.1 for thermal radiation.

Insulation material

A layer of insulating material can reduce heat losses from the back of an absorber. Insulation materials are commonly cellular, fibrous or granular. The insulation material in a solar collector is generally in contact with the absorber. Therefore, it should be able to withstand the collector stagnation temperatures.

Inorganic materials such as glass, fiber, mineral fiber, calcium silicate and perlite can withstand high temperatures. Rockwool insulation material is selected due to their higher resistance to the water, low thermal conductivity properties and higher thermal resistance.

Casing

The majority of solar collectors use aluminum as the major casing material. Other materials commonly used are glass (fiber) reinforced plastic (GRP) and galvanized mild steel. Occasionally polypropylene, polyvinyl chloride (PVC) and stainless steel are also used. Many materials with adequate properties are available. The choice of the material for casing is largely one of cost of the metallic materials; stainless steel and aluminum have good mechanical and weather properties (Blaga, 1978).

Seal

Sealing materials are applied to ensure the solar collector is not affected from weather conditions. The most common materials used are ethylene propylene diene monomer (EPDM) and silicone rubbers. Seals must also withstand the high temperatures encountered under stagnation conditions, which can be in excess of 100 °C.

1.1.1.3 Evacuated tube collectors

Evacuated tube collectors are mostly used to heat water in residential applications that require higher temperatures. Sunlight enters through the outer glass tube and strikes the absorber tube(s) and changes to heat. The heat is transferred to the liquid flowing through the absorber tube.

The collector consists of rows of parallel transparent glass Fig.1.7. Each tube contains an absorber tube with selective coating. In such type of solar collectors, tubes can be either added or removed (Dimitrios, 2015).

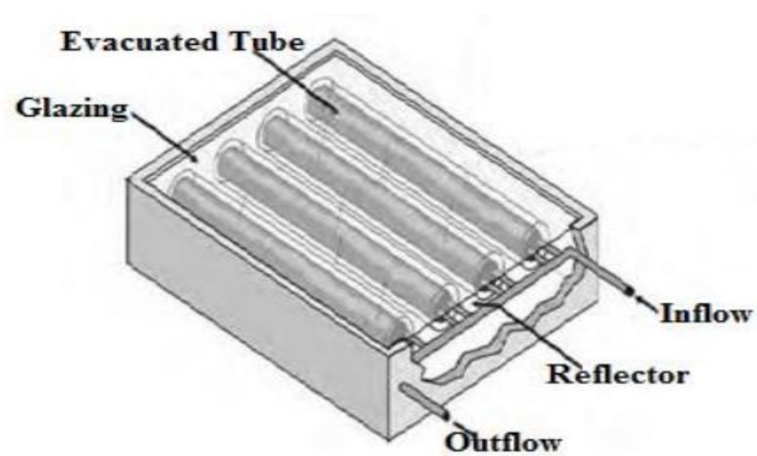

Figure 1.7. Evacuated tube collector (Dawit, 2016)

The tubes are designed in such a way that air is evacuated from the space between the two tubes forming a vacuum. Conductive and convective heat losses are eliminated because there is no air to conduct heat nor to circulate and cause convective losses. Positive fact of ETC is due to its shape. The circular shape absorbs the sunlight perpendicularly for most of the day. However, the disadvantage of such collectors is that are more expensive compared to flat plate.

1.1.1.4 Solar concentrators

Solar concentrators may be broadly classified as follows:

I. **Tracking type**: These types of solar concentrators are classified based on tracking type (continuous, intermittent, one-axis, or two-axis) or based on the moving device (focusing part or receiver or both) for tracking.
II. **Non-tracking type**: In this case, the axis of concentrator is fixed. There is no moving part.

Tracking Solar Concentrators

Solar concentrators are used to achieve moderate concentration with one-axis tracking. A few of them are discussed below:

Fixed-mirror solar concentrator (FMSC)

The fixed mirror consists of long, narrow flat strips arranged on a reference circular cylinder of a chosen radius R. The width of the mirror strip is compatible with the diameter of a given absorber/receiver pipe. The angle of each element is adjusted in such a way that the focal distance of the array is twice the radius of the reference cylinder.

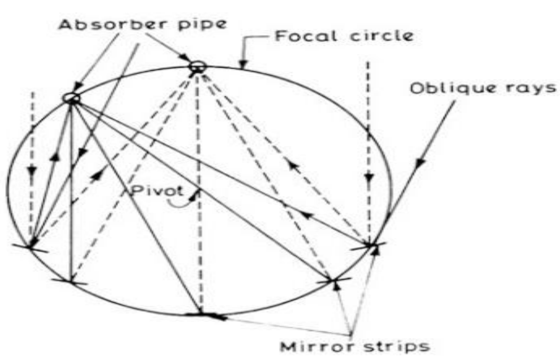

Figure 1.8. View of fixed-mirror solar concentrator (Dimitrios, 2015).

Cylindrical parabolic solar concentrator (CPSC)

A cylindrical parabolic trough solar concentrator comprises a cylindrical parabolic reflector and a metal tube receiver at the focal plane as shown in Fig.1.9. The blackened receiver is covered by the concentrator and rotated about one axis to track the Sun. The heat-transfer fluid is heated as it flows through the absorber tube (Duffie and Beckman, 1991).

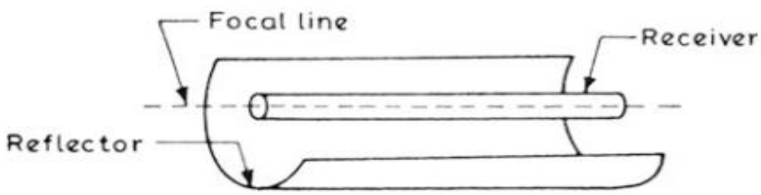

Figure 1.9.View of cylindrical parabolic concentrator (CPC) (Dimitrios, 2015).

Linear Fresnel lens/reflector

A linear Fresnel lens solar concentrator, as shown in Fig.1.10, consists of linear grooves on one surface of the refracting material. The groove angles are chosen with reference to a particular wavelength of incident beam radiation so that the lens acts as a converging one for the light, which is incident normally. The Fresnel lens may be installed with either of the following:

- **Sun-facing grooves**: In this case, the ineffective faces of the grooves prevent a part of the input beam light from being transmitted to the focus.
- **Downward-facing grooves**: In this case, the solar concentrator has a high surface reflection loss and large off-axis aberrations.

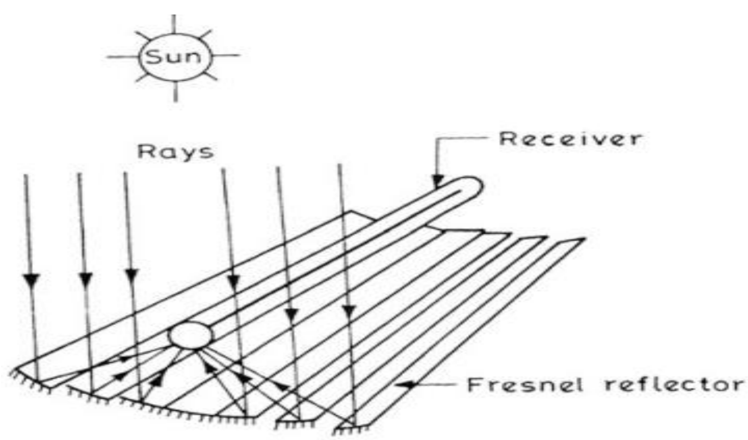

Figure 1.10.Schematic view of fresnel reflectors (Dimitrios, 2015).

Two-Axes Tracking Concentrators

These require two-axes tracking of the Sun. Some of these are briefly discussed as follows:

Paraboloidal dish solar concentrator (PDSC)

In a paraboloidal dish solar concentrator (PDSC), a parabola rotates about the optical axis as shown in Fig.1.11. In this case, a higher concentration ratio C is achieved (Duffie and Beckman, 1991) and (Mohamed, 2016).

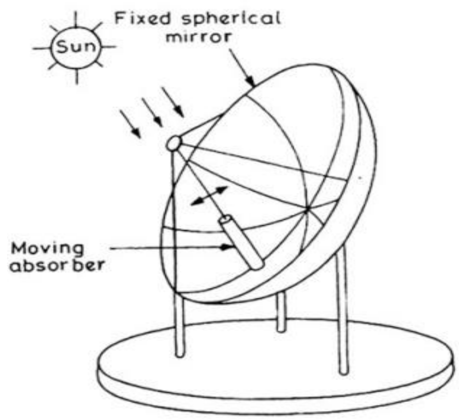

Figure 1.11. Schematic view of a paraboloidal concentrator (Duffie and Beckman, 1991).

Central tower receiver (CTR)

The central tower receiver (CTR) consists of a central stationary receiver and heliostats (composed of a large array of mirrors fixed to a supporting frame, which reflect the beam radiation toward receiver as shown in Fig.1.12.

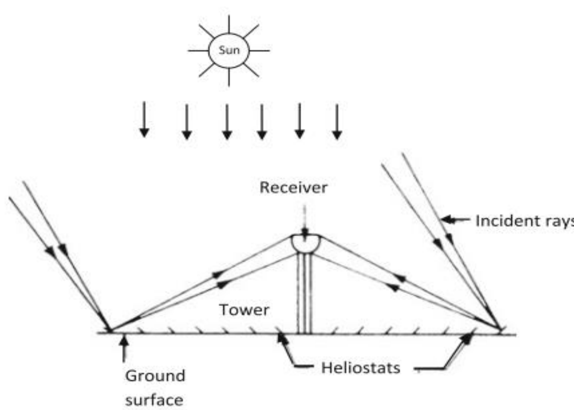

Figure 1.12. Schematic view of central receiver–heliostat system (Duffie and Beckman, 1991).

Circular Fresnel lens (CFL)

Lenses are not usually used in solar energy applications due to their high cost and weight.

Hemispherical bowl mirror

It has a fixed mirror and a moveable receiver-type concentrator.

1.1.1.5 Non-tracking solar concentrators

Tracking solar concentrators provide high delivery temperatures due to an accurate tracking device and fine surface; and hence they are expensive. Some of these concentrators are discussed in brief as follows:

a. **Flat receiver with booster mirror**: Fig.1.13 shows Flat-plate collector with flat booster mirrors in which the concentration ratio of such a concentrator is relatively low, but it is higher than that of the conventional FPC.
b. **Tabor–Zeimer circular cylinder**: It is a very simple cylindrical optical system. It consists of an inflated plastic cylinder with a triangular pipe receiver.
c. **Compound parabolic solar concentrator (CPSC):** This CPSC is a non-imaging one. It belongs to a family of concentrators with maximum permissible concentration under thermodynamic limit for a particular acceptance angle.

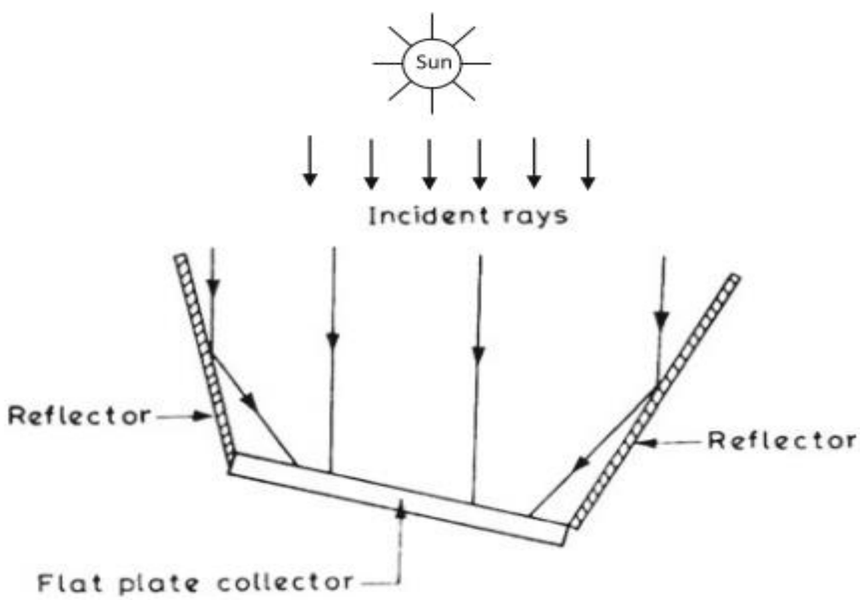

Figure 1.13. Flat-plate collector with flat booster mirrors (Duffie and Beckman, 1991)

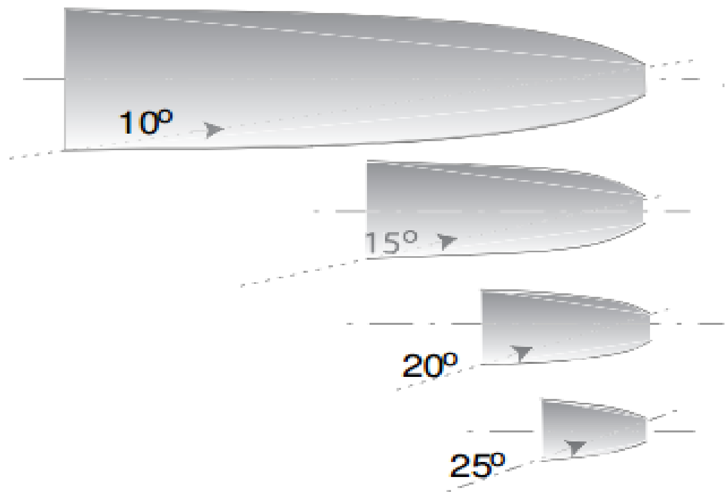

Figure 1.14. CPSC for the same exit aperture, the larger the entrance aperture, the smaller the acceptance angle (Ald Vieira, 2012).

1.1.2 Flow configuration in solar collectors

A conventional solar water-heating system essentially consists: (a) the collection unit and (b) the insulated storage unit. The collection unit is a combination of flat-plate collectors (FPC). The hot water, available at outlet (T_{out}) is transferred to the insulated storage tank to reduce possible heat losses for the storage of hot water during off-sunshine hours (nighttime). Transportation of the hot water from the flat-plate collector (FPC) to the insulated storage tank can be performed by two modes, namely (Tiwari, 2016):

i. The thermosiphon/natural mode
ii. Forced-circulation mode

1.1.2.1 The thermosiphon/natural mode

As the sun shines on the collector, the water inside the collector flow - tubes is heated. As it heats up, this water expands slightly and becomes lighter than the cold water in the solar storage tank mounted above the collector. In this case, the hot water is circulated between the FPC to the insulated tank under gravitational force. To achieve this, an insulated storage tank should be placed above the flat-plate collector modules.

There are three type of such water heater, namely:

Non-pressure type

In this case, an insulated storage tank is filled with cold water once in the morning, and hot water can be withdrawn per requirement at any time in the day or night.

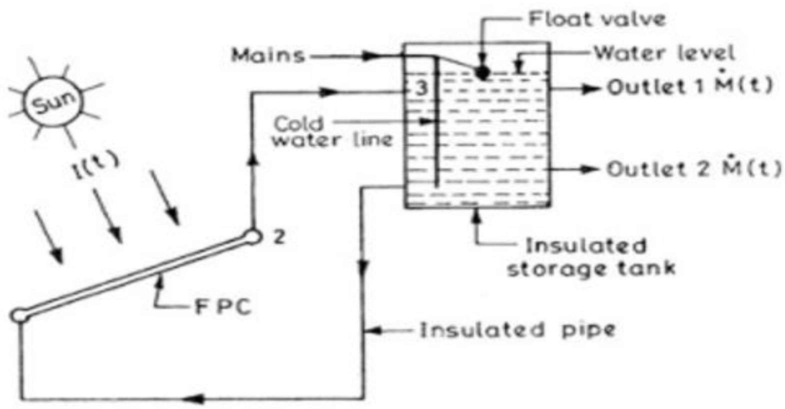

Figure 1.15. Schematic diagram of a non-pressure-type solar water heater with natural circulation (Duffie and Beckman, 1991).

Pressure type

In this case, too, an insulated storage tank is filled with cold water once in the morning. However, hot water can only be withdrawn if main water line has water with sufficient pressure.

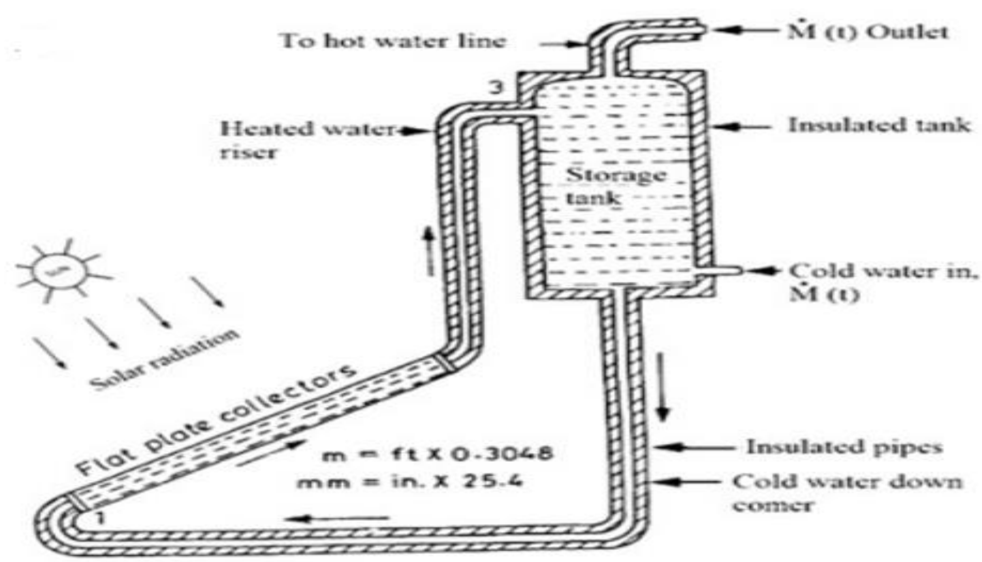

Figure 1.16. Schematic diagram of a pressure-type solar water heater with natural circulation (Duffie and Beckman, 1991).

Pressure type with heat exchanger

It is important to mention here that the heat exchanger is used only for the withdrawal of hot water from the insulated storage tank.Fig.1.17 shows Schematic diagram of a pressure-type solar water heater with natural circulation and a heat exchanger.

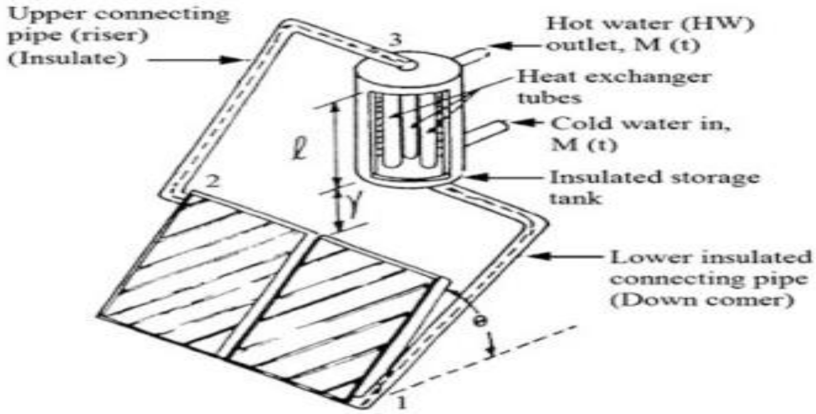

Figure 1.17. Schematic diagram of a pressure-type solar water heater with natural circulation and a heat exchanger (Duffie and Beckman, 1991).

1.1.2.2 Forced-circulation mode

In this case, there is no need of placing an insulated storage tank above the FPC module due to the forced circulation of hot water between the FPC and the insulted tank. Here a water pump for a given capacity is required for the flow of water as shown in Fig.1.18.

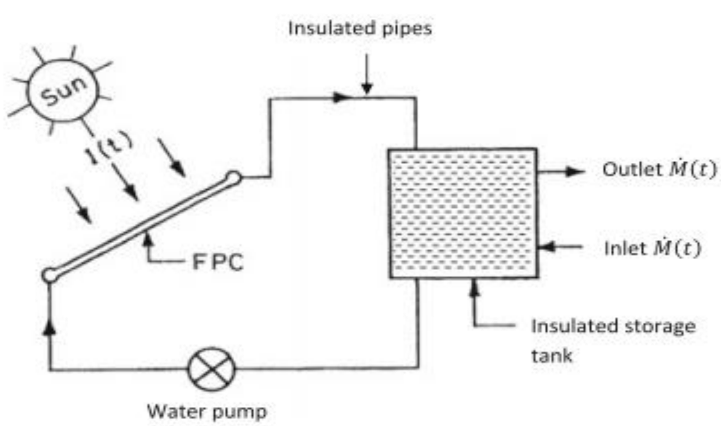

Figure 1.18. Schematic diagram of a simple single-loop water-heating system (Duffie and Beckman, 1991).

1.1.3 Nanofluids

A nanofluid is a heterogeneous mixture of solid and liquids (water, ethylene glycol, propylene glycol, or oil). Here the solids are tiny particles such as metal (Ag, Au, and Cu) metal oxides (TiO_2, SiO_2, CuO, Al_2O_3, ZrO_2), or carbon (diamond, graphite, CNT, fullerene, graphene) of nanometer size (< 100 nm) which can be nanoparticles, nanotubes, or nanowires. The liquid can be a single base fluid or a mixture of different fluids. This mixture forms a colloidal suspension in stable conditions with or without the addition of dispersants. Fig.1.19 shows The structure of CuO nanofluids with different size.

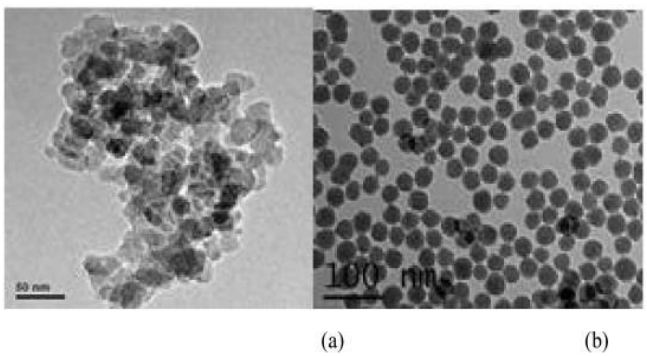

Figure 1.19. The structure of CuO nanofluids with different size Zhu et al., (2011).

As nanofluids have more enhanced heat transfer properties than the base fluid, much research has conducted during the past two decades. The heat transfer augmentation found in nanofluids is mainly due to a small concentration of nanoparticles that dramatically change or enhance the thermo-physical properties of the base fluid. It shows promise in enhancing heat transfer characteristics in applications such as electronics cooling, nuclear reactors, and engine cooling, as well as solar energy applications.

As today's systems become increasingly complex with decreasing size, adequate cooling systems become more critical. A nanofluid can supplement the heat transfer capabilities of the base fluids, potentially, leading to a reduction in energy consumption (Debashis, 2017).

Applications of Nanotechnology:

- ✓ Nano-medicine
- ✓ Nano-biotechnology

- ✓ Green nanotechnology
- ✓ Energy applications of nanotechnology
- ✓ Industrial applications of nanotechnology
- ✓ Potential applications of carbon nanotubes
- ✓ Nanoart

Properly engineered nanofluids possess the following advantages:

- ❖ High specific surface area and therefore more heat transfer surface between particles and fluids.
- ❖ High dispersion stability with predominant Brownian motion of particles.
- ❖ Reduced pumping power as compared to pure liquid to achieve equivalent heat transfer intensification.
- ❖ Reduced particle clogging as compared to convention slurries, thus promoting system miniaturization,
- ❖ Adjustable properties, including thermal conductivity and surface wet ability, by varying particle concentrations to suit different applications.

1.1.3.1 Nanofluid preparations

Nanofluid preparation is the first and most significant step, because this determines whether nanoparticles will remain in colloidal suspension or as a sediment or aggregate in the base fluid. There are generally two methods:

1. The two-step method and
2. The one-step method (single step).

One-step method

The one-step process consists of simultaneously making and dispersing the particles in the fluid. **Eastman et al**. developed a one-step physical vapor condensation method to prepare Cu/ethylene glycol nanofluids (Ali, 2018).

In this method, the processes of drying, storage, transportation, and dispersion of nanoparticles are avoided, so the agglomeration of nanoparticles is minimized, and the stability of fluids is increased.

The one-step processes can prepare uniformly dispersed nanoparticles, and the particles can be stably suspended in the base fluid. However, there are some disadvantages for one-step method. The most important one is that the residual reactants are left in the nanofluids due to incomplete reaction or stabilization. It is difficult to elucidate the nanoparticle effect without eliminating this impurity effect. Additionally, One-step physical method cannot synthesize nanofluids in large scale, and the cost is high (Xie, 2011).

Two-step method

Two-step method is the most widely used method for preparing nanofluids as shown in Fig.1.20. Nanoparticles, nanofibers, nanotubes, or other nanomaterials used in this method are first produced as dry powders by chemical or physical methods. Then, the nanosized powder dispersed into a fluid in the second processing step with the help of intensive magnetic force agitation, ultrasonic agitation, high-shear mixing, homogenizing, and ball milling. Two-step method is the economic method to produce nanofluids in large scale, because nanopowder synthesis techniques have already scaled up to industrial production levels. Due to the high surface area and surface activity, nanoparticles have the tendency to aggregate. The important technique to enhance the stability of nanoparticles in fluids is the use of surfactants. However, the functionality of the surfactants under high temperature is also a big concern, especially for high-temperature applications.

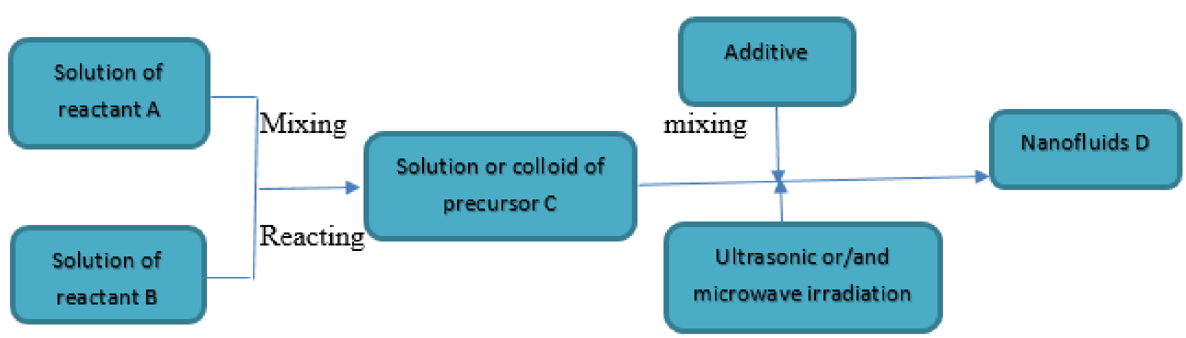

Figure 1.20. Flow chart of chemical solution method (CSM) (Debashis, 2017).

1.1.3.2 The stability of nanofluids

One of the most important challenges faced during the preparation of nanofluids is their poor stability. Because of strong van der Waals forces of attraction, nanoparticles in the nanofluid adhere together and form aggregates of increasing size, which may settle due to gravity.

The agglomeration of nanoparticles results in not only the settlement and clogging of microchannel but also the decreasing of thermal conductivity of nanofluids.

The Stability Evaluation Methods for Nanofluids

Sedimentation method

It is the simplest method to evaluate the stability of nanofluids. The sediment weight or the sediment volume of nanoparticles in a nanofluid under an external force field is an indication of the stability of the characterized nanofluid. Sedimentation photograph of nanofluids in test tubes taken by a camera is also a usual method for observing the stability of nanofluids (Xie, 2011). Zhu et al. used a sedimentation balance method to measure the stability of the graphite suspension (Li, 2009).

Zeta Potential Analysis

Zeta potential is electric potential in the interfacial double layer at the location of the slipping plane versus a point in the bulk fluid away from the interface, and it shows the potential difference between the dispersion medium and the stationary layer of fluid attached to the dispersed particle.

Spectral Absorbency Analysis

Spectral absorbency analysis is another efficient way to evaluate the stability of nanofluids.

The Ways to Enhance the Stability of Nanofluids

There are several methods to attain stability, which are discussed by different researchers. These methods include sonication (ultrasonic vibration), high shear homogenization, and high-pressure homogenization, varying or controlling PH, and addition of surfactants, surface modification techniques, and ball milling.

Ultrasonication

In ultrasonication, supersonic waves are generated which disintegrate larger particles into smaller fragments. There are generally two types of ultrasonicators available, the bath and the probe type. Researchers consider the probesonicator better in terms of improved performance. Several researchers have used this technique to stabilize the nanofluid.

High shear and high-pressure homogenization method

A high shear homogenizer comprises a rotor and a stator rotating at a very high speed. This device breaks down the agglomerated particles present in the nanofluid into the primary particle size.

Controlling the pH

The pH is related to electrostatic charge present on the surface of the particle, which helps in maintaining the stability of a colloidal solution. On changing the pH value of the base fluid, the charges on the surface of particles change and thus modify the interaction behavior of the particles, which may affect the stability of the fluid.

Using Surfactants in Nanofluids

Dispersants are Surfactants used in nanofluids. Adding dispersants in the two-phase systems is an easy and economic method to enhance the stability of nanofluids.

Surface Modification Techniques

Use of functionalized nanoparticles is a promising approach to achieve long-term stability of nanofluid. It represents the surfactant-free technique.

1.1.3.3 Nanofluids thermal properties

Thermo-physical properties of the nanofluids are quite essential to predict their heat transfer behavior. Nanofluids are considered effective than the base fluid because of their better thermos-physical properties i.e. density, specific heats, thermal conductivity, thermal diffusivity and viscosity. The term effective used to show the mixed property of both base fluid and nanoparticles. The thermal conductivity of basic nanoparticles are given in Table 1.4.

Table 1.4. Commonly used nanoparticles thermal properties (Dimitrios, 2015).

Nanoparticles	**Density (kg/m^3)**	**Thermal conductivity (W/m K)**	**Specific heat (J/kg K)**
Al_2O_3	3880	36	773
CuO	6350	69	535
Fe_2O_3	5180	80.4	670
SiO_2	2220	1.4	754
TiO_2	4175	8.4	692
ZnO	5600	29	514

Table 1.4 shows CuO nanoparticles has higher density than other nanoparticles whereas SiO_2 has lower density. Also the thermal conductivity of Fe_2O_3 is greater than other nanoparticles and SiO_2 has lower thermal conductivity as given in Table 1.4.

1.2 Problem of statement

The Ethiopian population will continue growing for several decades to come. Urbanization in the country keeps in increasing sharply and energy demand is likely to increase even faster. Even though the huge renaissance dam is undergoing construction the country facing the shortage of energy. As a part of ongoing fast economic growth noted in the country many residential, i.e. condominium house have been established, adding that this had increased local demands especially big cities like Addis Ababa and Adama to replace electric water heater. Additionally, to increase per capita of the individuals and create the job opportunity the emphasis should be towards the small-scale energy production i.e. solar collectors. Solar collectors are solar energy devices used to convert solar energy into heat energy. In order to enhance heat transfer in solar application, nanofluids as absorber fluid is an effective approach due to their high thermal conductivity.

Researches have been conducted on different situations in solar energy field to improve the quality, increase productivity, and consequently, save money by using nanofluids based solar collector. However, most review concentrates only on single nanofluid. Since there are no sufficient numerical studies on the thermal efficiency of FPSC using different nanofluids as working fluids, there is no enough comparison between different nanofluids.

Using nanofluid in place of water as working fluid can reduces the size of collector, increases the performance collector and saves money than the domestic solar flat plate collector. However, the problem for the same collectors size the energy harvested from the collector is low in domestic flat plate collector. In addition, for the same outlet temperature of fluid the size of FPC becomes large, which takes more space, costly and difficult to maintain as well. Though there are a number of studies on improvement of flat plate solar collectors, the studies done with nanofluids is very limited in number.

Lastly, there is a few study that is done on solar flat plate collector based on nanofluids using ANSYS FLUENT 17.2 software. Therefore the numerical simulation for different nanofluids and volume fractions are done using ANSYS FLUENT 17.2 software.

1.3 Objectives

1.3.1 General objective

The main objective of this thesis is to study the effect of varying concentration of water-based nano-fluids on SFPC performance to determine the optimum heat transfer efficiency of the system.

1.3.2 Specific objectives

- ✓ To estimate solar radiation at Adama.
- ✓ To model the solar FPC geometry using Solid work software.
- ✓ To conduct performance analysis of conventional FPC.
- ✓ To conduct performance analysis and comparison of FPC with nanofluids of different concentrations and types with conventional fluid.
- ✓ To experimentally validate on aluminum oxide nanofluids and solar collecting medium with the performance of conventional fluid based SFPC.

1.4 Overview of study area

Adama is a large city located about 60 miles southeast of Addis ababa in central part of Ethiopia. The city is large; with the population close to one third of a million people .the city has the importance as a transportation spot as well as educational center, with a large university located in the city. The city located at latitude and longitude coordinates of 8.514477^{o} and 39.269257^{o} respectively and at elevation of 1712 m above sea level.

1.5 Significance of study

Currently, in Adama construction of thousands of housing units (close to 10,000 at present) is either completed or underway throughout the country. Therefore, even if a fraction of existing electric water heaters were replaced by solar water heaters (SWHs) over the next several years the market would remain attractive enough for private investment.

The major focus of this study will be to fulfill the hot water demands of nation with SFPC's that use water based nanoparticles. This nanofluid solar collector has better efficiency than the domestic solar collector due to thermodynamic properties of nanofluid. Additionally, solar FPC with nanoparticles is known to significantly reduce the size of collectors and increase the performances of the collector.

1.6 Scope and limitation of study

The numerical simulation of this research is based on the meteorology data of Ethiopia, Adama city. The Study can be applicable to wide range of application however this study focuses on the low temperature water heating system. The CFD simulation is done for internal flow of fluid in SFPC using ANSYS FLUENT 7.2. Four nanoparticles (i.e. Si_2O, Ti_2O, Al_2O_3 and CuO) of different concentration are selected and their performances are compared with water. The experimental setup and test was done, and production of nanoparticles and nanofluids discussed in this study.

1.7 Organization of the study

The rest of this thesis is organized in to five chapters each having a distinct and related purpose. The next chapter, chapter two, explains the theoretical and empirical literature review. The appropriate methodology and method is developed at chapter three that clearly identifies the empirical techniques, correlations, and software tools used. Chapter four is devoted to the discussion, analysis and its outcome related to the result while chapter five is prepared to deal with economic aspect of the study. Finally, chapter six draws conclusions, recommendations and future work.

CHAPTER TWO

LITERATURE REVIEW

The efficiency of the flat plate collector depends on the temperature of the plate, ambient temperature, solar insolation, top loss coefficient, the emissivity of the plate, transmittance of a cover sheet, number of glass cover and tracking system.

Until now different geometric configuration, mechanism, design, and modeling was performed to increase the performance of solar FPC. For instance, **Matuska**, (2009) performed the detailed modeling of SFPC with design tool KOLEKTOR 2.2. The mathematical model and design software tool KOLEKTOR 2.2 was built and experimentally validated for different solar thermal FPC concepts. The collector performance with three fin widths (50, 125, 200 mm) has compared at lower temperature difference and the efficiencies reported were 68, 78, and 82%, respectively. In addition, the authors found between the collector with an insulation thickness of 40 and 60 mm, there is no considerable efficiency difference (almost 79%), however, for a thickness of 20 mm, the 76% efficiency was achieved using the model.

Saleh, (2012) studied on the modeling of flat plate collector operation in transient states. The model considers the time-dependent thermos-physical properties and the differential equations are solved using the implicit finite difference scheme and executed by using Matlab. The result showed a good agreement between the predicted and measured results. The maximum error was 3.65% for inlet temperature and 4.1% for the outlet temperature.

Ebrahimi and Sahb (2017) studied on predicting efficiency of SFPC using a fuzzy inference system and compare with multiple linear regression. Fuzzy Logic is a multi-valued logic that uses approximate values rather than crisp values of 0 and 1 for reasoning. Experimental results showed that the predicted efficiency values found to be in close agreement with the experimental counterparts with a coefficient of determination of 0.9469, root mean square error of 3.13 and average forecasting error of 6.98, respectively.

2.1 Parameters affecting solar flat plate collector SFPC

There are a lot of parameters affecting the solar flat plate collector performance:

2.1.1 Shapes of tube

Kumar, (2014) investigated the performance of the solar flat plate by using a semi-circular cross-sectional tube as shown in Fig. 2.1. The useful heat gains improved from 200 to 250 W/m^2 for 30 ^{o} C inlet temperature. A flat plate collector is such a type of solar thermal collector, which is used in locations where moderate heat is required. It can increase the temperature of the fluid up to 100 ^{o} C above ambient temperature. It is also simple in design, no moving parts and requires little maintenance. They are also relatively cheap and can be used in a variety of applications.

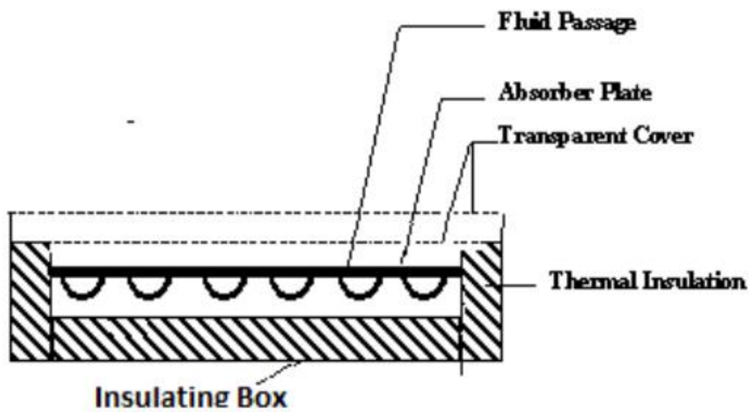

Figure 2.1 Flat plate collector with semi-circular cross-sectional tube

Muhammed & paul, (2015) studied the analysis of heat transfer performance of SFPC using CFD. The study presented results of analytical investigations on the effects of variations in the shape of tubes for flat plate solar collector performance. The numerical analysis was carried out with ANSYS CFD FLUENT software. Efficiency values reported corresponding to mass flow rates of 0.025, 0.035 and 0.05 kg/s were 45, 45.5, and 45.4%, respectively at reduced temperature parameter (T_i-T_a)/G of 0.005. Moreover, FPC with copper, aluminum and steel absorber material 45, 45.25, and 45.4% achieved accordingly. Additionally the outlet temperature 300 and 360 K is harvested at 878.5 W/m^2 solar radiation and 0.025 kg/s for semi-circular and circular tube, respectively.

Mahesh and Deshmukh (2016) investigated on a new flat plate collector performance for the solar water heating system. The authors used the collector made-up of rectangular aluminum pocket having size 0.35 m X 0.1 m and aluminum pipe. Finally, the maximum temperature of water achieved at the collector outlet is about 69 ^{o} C. Also, **Thakare and Khot** (2016) puts the performance investigation of formed tubes of different geometries for an SFPC experimentally. At the inclination angle of 30 ^{o} C and flow rate of 100 LPH, the efficiency of the triangular, square and elliptic tube are 78, 68.12 and 74.11%, respectively. In addition, the result showed an increasing mass flow rate from 75 to 100 LPH improves efficiency from 64 to 68% for the case of a triangular tube.

Similarly, **Vasudeva and Cornelio** (2017) performed a CFD analysis of SFPC for improvement in thermal performance with the different geometric treatment of the absorber tube. Two distinct criteria's are adopted which influence the Nusselt number. They are i) Constant area criteria and ii) constant perimeter. The standard k-epsilon model adopted to take into account the turbulent conditions that might occur in the flow domain. For the criterion with constant perimeter interestingly, geometry with rectangular cross section provided the highest net temperature rise of 6 K while for the configuration with trapezium cross-section, and the highest drop in the pressure of 310 Pa inferred.

2.1.2 Design of SFPC

The most common designs for flat plate collectors are the header and riser collector and the serpentine design. The serpentine design collector does not present the potential problem of uneven flow distribution in the various riser tubes of the header and riser design, but serpentine collectors cannot work effectively in thermosiphon mode and need a pump to circulate the heat transfer fluid Tsirakoglou, (2011).

John and Koshy (2014) made an experimental analysis of the SFPC system for small-scale desalination applications. The experimentation on a solar flat plate collector carried out at Coimbatore, India (11 °N Latitude and 74 °E Longitude). The maximum temperature of water obtained on a typical day in the month of April was 64 °C with solar radiation of 932.2 W/m^2. The two-pass flow of water across the absorber plate results in a maximum temperature gain with an overall collector efficiency of 43.7%.

Birhanu et al., (2016) did the Computational fluid dynamic simulation and experimental testing of a serpentine flat plate SWH at a latitude of 7.7 ^{o} (Jimma, Ethiopia). The study is to improve the thermal performance of passive serpentine SFPC's using the striped technique. Striped absorber plate of the serpentine solar collector in various modes designed by ANSYS 14.5 relase FLUENT and simulated using computational fluid dynamics. The Heat flux of 650 W/m^2 calculated from average based on solar radiation collected on June 30, 2014. Absorber plate (‘T_p’) and water at the exit of the collector (‘T_0’) during the experimental test attained the maximum temperature of 353 and 336.9 K, respectively.

Later, **Malvi et al.,** (2017) performed an experimental investigation of heat removal factor (FR) in SFPC for various flow configurations. These configurations are Serpentine Flow, Parallel-Wall-to-wall flow and Spiral Flow. The results indicate the superior thermal performance of parallel wall-to-wall flow relative to the serpentine flow for the mass flow rate of 4 kg/hr. that is the maximum mass flow rate where FR for serpentine and parallel wall-to-wall flow is 0.47 and 0.96 respectively since the FR does not change significantly above that.

2.1.3 Absorber plate and tube material

Rajasekaran et al., (2015) have studied the effect of coated solar FPC. They have conducted the experiment by using copper, stainless steel and aluminum tubes as header and riser tubes. The results showed the maximum temperature of the peak solar insolation during a test at a maximum water temperature of 70 ^{o}C for copper 66 ^{o}C for aluminum coated with copper oxide, and 62.5 ^{o}C in stainless steel coated epoxy polyether. In addition, the collector efficiency at 9.00 hr is 39.42, 31.79 and 27.79% for copper, aluminum and stainless steel tubes, respectively. Similarly, **Irfan et al.,** (2015) investigated on the performance analysis of SFPC. Mild steel and galvanized iron used for absorber plate and tube respectively. For this selection of material, the maximum efficiency obtained was 9.75% at a temperature of 67 ^{o}C.

Additionally, **Saravanan and Krishna** (2016) did an experimental investigation on the flat plate solar water heater with glass as absorber material. Three different absorber materials like Absorber Black painted clear toughened glass plate sandwich type (ABPCTG), Absorber Tinted toughened glass plate sandwich-type (ATTG) and Absorber Galvanized Iron plate with pipe (AGI) used for comparison. For different mass flow rates, the ABPCTG found to show the highest thermal efficiency throughout the day.

2.1.4 Mass flow rate

Stanciu et al., (2016) studied on the analysis of FPC for hot water domestic use. A comparison provided between the cases of constant and time-dependent mass flow rate. Numerical simulation was done for a constant mass flow rate to the user, corresponding to 3 L/hr. in the volume flow rate. The authors found the smooth variation and maximum temperature of about 55 ºC in the storage tank in Romania's climate condition. However, for the time-dependent mass flow rate to the user the steep variation of storage tank temperature and the maximum temperature of 50 ºC reached.

2.1.5 Wind speed

Gowda et al., (2014) Investigated the mathematical modeling to assess the performance of solar flat plate collectors. The well-known Hottel-Whiller-Bliss equations used to assess the performance of the solar collector system. Effect of various parameters like cold-water inlet temperature, ambient temperature, insulation thickness, wind speed, the transmission coefficient of the glass cover, on the performance of the solar collector system for Bangalore (13 ^{o} N, 77.56 ^{o} E) climatic conditions was analyzed. Accordingly, the effect of wind speed was found to be 6% and the maximum efficiency of the system reported was 51% from noon at 12:00 pm to 13:00 pm and gradually decreases.

2.1.6 Reflector

The solar reflector used here with the solar collector to increase the reflectivity of the collector. **Baccoli, et al.,** (2015) studied a mathematical model of a solar collector augmented by a flat plate reflector. Moreover, identified the optimum collector and reflector inclination at which the maximum performance achieved. The anisotropic sky model used and takes into account a finite length system with different angular configurations and reciprocal shading. Computer simulation has carried out in order to find the optimum angles of the reflector with respect to the plane of the collector. The authors found the yearly energy up taken by tilt collector is 7500 MJ/m^2 at 500 optimal inclination of the collector and reflector for each month at 39 ° N latitude.

In addition, **Bhowmik and Amin** (2017) investigated the efficiency enhancement of SFPC using a reflector. The solar reflector used here with the solar collector to increase the reflectivity of the collector. A prototype of a solar water heating system was constructed and obtained the improvement of the collector efficiency around 10% by using the reflector.

However, throughout the above works, it is difficult in order to increase the temperature of fluid more than 85 ^{o}C due to low thermal conductivity of fluid is often the primary limitation. Recent advances in nanotechnology have allowed the development of a new category of fluids termed as Nano-fluids, which first used by a group in **Argonne national laboratory USA (Choi, 1995).**

2.2 Nanofluid

Nanofluid is liquid suspensions containing nanoparticles with thermal conductivities orders of magnitudes higher than the base liquids, and with sizes, significantly smaller than 100nm. Recently, there is an interest in using nanoparticles as additives to modify heat transfer fluids to improve their performance.

2.2.1 Preparation of nanofluids

Preparation of nanofluids is a challenging issue due to agglomerate formation. This settling of nanoparticles in base fluids is a natural phenomenon due to gravity. The degree of agglomeration has significant influence on the thermal properties of nanofluids .it can cause sedimentation during transportation.

Colloidal theory states that the sedimentation in suspension ceases when the particles size is below a critical radius, due to counter balancing of gravity forces by the brownian forces application of smaller size of nanoparticles can be a good practice to prepare stable nanosuspensions. However smaller particles exhibit high surface energy which affects the formation of agglomerates among them to prepare the stable nanofluids optimum diameter and concentration should be known. The two methods used to prepare nonafluids **Suhaib et al.,** (2014).

2.2.1.1 Two step method

The two-step method is most widely used to produce nanofluids. First dry powder is created by physical or chemical methods. Then the dry powder is mixed with the base fluids to form nanofluids. Different investigators used this method for preparation of nanofluids . **Barrett et al.,** (2013) studied the nanofluids preparation using two-step method. Nanoparticles Al_2O_3 with diameter of 50 nm and concentration of 1% mixed with water. As a result, the authors found the agglomerate size reduced after 5h of sonication. **Lee et al.,** (2008) examined the stability of nanofluids by using two step method with Al_2O_3 nanoparticle of size 30 nm and concentration of 0.01- 0.03%. The result showed that the stable nanofluids obtained after 5 h of sonication. Also (**Rajaeiyan**, 2013) compare the sol gel and co-precipitation methods of synthesizing Al_2O_3. The authors found that the synthesis method and reaction temperature on phase transformation of alumina nanocrystals.

Qinbo et al., (2015) did experimental investigation on the efficiency of SFPC with nanofluids. Cu-H_2O Nanofluids with different mass fraction and size prepared through two-step method. Accordingly, the result showed that the highest temperature and heat gain of water in the Nanofluid 25 nm, 1.1 wt% tank can increased up to 12.24% and 24.52% compared with water tank, respectively.

2.2.1.2 Single step method

The production of nanoparticles and their dispersion in liquids occur simultaneously. Nanofluids produced by this method exhibit less agglomeration. However, there is high production cost and this method cannot synthesis nanofluids in large scale. **Eastman et al.,** (1997) developed a one-step physical vapor condensation method to prepare Cu/ethylene glycol nanofluids. **Zhu et al**., (2004) a novel one-step chemical method for preparing Cu nanofluids.

2.2.2 Sedimentation in nanofluids

The knowledge of sedimentation characteristics can be useful in evaluating the stability of nanofluids. The common method is the visualization technique, which uses the photographs of static nanofluids in a batch sedimentation column to estimate the rate of settling and type of agglomeration. **Brunelli et al.,** (2013) investigated sedimentation and agglomeration effects of Ti_2O nanofluids in water using a fluorescence spectrophotometer. Sedimentation rates is calculated by the first order decay equation as:

$$k = \frac{-\ln\frac{C}{C_o}}{t} \quad \text{……………………………………………………………….. (2.1)}$$

Where k is the frist order rate constant, C is the concentration at time t and C_o is the concentration at time 0. Also **Garrido et al.,** (2004) come with a simulation method to measure the settling velocity of flocculated particles in a suspension during batch and continuous sedimentation based on sedimentation consolidation theory.

Different researchers used various nanoparticles to increase the thermal conductivity of the fluid for many thermal applications i.e. automotive radiator, refrigeration and air conditioning, heat exchangers and solar collectors. **Chandraprabu et al.**, (2013) did an experiment on the performance of CuO/Water Nanofluid as Outer Fluid in the Tube Condensing Unit of Air Conditioner. With the concentration of 1 - 4% and a size of 30 nm of CuO nanoparticles in water as cooling fluid, the heat transfer rate of CuO nanofluid improved by 35%. Where as **Vandaarkuzhali and Elansezhian** (2014) studied the performance evaluation of air conditioning using nanofluids. Experimental measurements performed for three types of Nano-fluids namely (CuO, ZnO, and Al_2O_3) has analyzed. Simulation has shown for the same geometric characteristics of the system performance increased from 12 to 18% by the application of nanofluid as a fluid in vapour compression cycle (VCS).

Harsh et al., (2018) studied the heat transfer characteristics of nanofluids in an automotive radiator. This study presented an experimental study on heat transfer using Nano-fluid as coolants in engines. Particles having a diameter in the range 10^{-3} to 10^{-6} m have low thermal conductivities and cause clogging in the flow section along with significant friction and are highly unstable in solution. The nanoparticles used in this experiment are CuO and TiO_2 having a particle size less than 80nm. The result shows that there is an improvement of 24.5% in the overall heat transfer coefficient and there was an increase of 13.9% in the heat transfer rate compared to the base fluid (80:20 Water: ethylene glycol EG solution).

Additionally, **Patel and Mavani** (2014) studied the effect of nanofluids and mass flow rate of air on the heat transfer rate in automobile radiators by CFD analysis. They present a CFD modeling simulation of the mass flow rate of air passing across the tubes and coolants into the tubes of an automotive radiator. Solid modeling of automobile radiator in Cre O software and then the solid model transferred to Hypermesh_64 for water type geometric cleanup and geometric model transferred to STAR CCM+ for meshing and CFD Analysis. STAR CCM+ analysis showed there is a 380 K inlet temperature of water+ ethanol, CuO/water, and TiO_2/water decreased up to 375, 357 and 359 K, respectively. Heat transfer rate higher in nanofluids than base fluids at 1.2 Kg/s mass flow rate of air. It is found that the optimum performance of the radiator achieved having CuO /water nanofluid as a coolant and 4 kg/s mass flow rate of air.

Nanofluids can be used in different types of heat exchangers**. Kabeel et al.**, (2014) investigated the enhancement of modified solar still integrated with external condenser using nanofluids. The experimental attempts made to enhance the solar still productivity by using nanofluids and by integrating the still basin with an external condenser. The results showed that integrating the solar still with external condenser increases the distillate water yield by about 53.2% and using Nano-fluids improves the solar still water productivity by about 116% when the still integrated with the external condenser. And also, **Sarafraz and Hormozi** (2016) studied heat transfer, pressure drop and fouling studies of multi-walled carbon nanotube Nanofluids inside a plate heat exchanger. Experiments performed at three different inlet temperatures of 50, 60 and 70 ^{o}C. The experiment showed that thermal conductivity could be enhanced up to 21, 41 and 68% for the volumetric percentage of 0.5, 1 and 1.5%, respectively.

Reza et al., (2016) put an effort on an experimental study of nanofluid effects on heat transfer in a closed cycle system in shell and tube heat exchangers at Isfahan power plant. The study investigated the effect of distilled-water/ silver nanofluid (with a size of 0.01%, 0.025%, 0.05%, and 0.075%) on heat transfer in a closed cooling system of one of the electrical energy generation units at Isfahan power plant. The authors come with nanofluid increased heat transfer coefficient by 16%. The pressure drop of nanofluid, however, has no significant change compared with the pressure drop of pure water.

Gabriela and Angel (2013) are performed experimental and numerical investigations of the thermal performances of wickless heat pipes using nanofluids. The operating temperatures of the wickless heat pipe (50, 60, 70, 80, 90 and 95 °C) and two nanoparticles concentrations (2.0 and 5.3 vol.%) Used for numerical investigation. The numerical results showed the temperatures significantly decrease in the evaporator when nanofluids used as the working fluid. Also, increases the particle concentration decrease the temperature difference between the evaporator and condenser sections. **Kumaresan and Venkatachalapathy** (2014) emphasized the enhancement of the convective heat transfer coefficients of the evaporator and condenser section of the mesh wick-heat pipe. CuO/DI water nanofluid with the concentrations of 0.5, 1.0 and 1.5% wt.

respectively used in the experiment as a working fluid and its results compared with DI water. For an optimum concentration of 1.0% weight the evaporator and condenser, the heat transfer coefficient increases by about 40.1% and 64.8%, respectively.

Jaydev et al., (2016) did an experimental investigation of hybrid nanofluid on thermosiphon type wickless heat pipe heat exchanger thermal performance. Hybrid Nano-fluid of 2% volume concentration with 75% of copper oxide (CuO) and 25% of carbon Nano-tube (CNT) was prepared. The heat transfer coefficient of heat pipe heat exchanger increases as air velocity increases. Heat transfer coefficient ranges 45.9 to 123.5 W/m^2K and 58.1 to 158.1 W/m^2K for condenser and evaporator section respectively. **Ebrahimnia et al.,** (2016) experimental and numerical investigation of nanofluids heat transfer characteristics for potential application in solar heat exchangers. The thermal conductivity and dynamic viscosity of the prepared nanofluids haven measured and modeled at different temperatures and nanoparticle concentrations. The results indicated that the maximum enhancement of the heat transfer coefficient at a lower concentration of 2.3 vol.% to be 21%.

Elmir et al., (2012) demonstrated the effect of Al_2O_3/water nanofluids as coolant simulated for a silicon solar cell using the finite element method. The author showed the maximum local Nusselt number along the outlet for Re = 5.0 varies for a concentration of 0, 4 and 8% are 0.45, 0.5 and 0.55 respectively. The addition of nanoparticles to a basic fluid does not affect the structure of the flow but the increase in the thermal conductivity of the mixture increases the rate of heat transfer.

Nasrin et al., (2014) investigated the behavior of different nanofluids related to performance such as temperature and velocity distribution, radiative and convective heat transfers, mean temperature and velocity of the nanofluid systematically. The governing partial differential equation with proper boundary conditions solved by FDM using Galerkin's weighted residual scheme. The result showed that the Ag nanoparticle with a 5% solid fraction has the highest rate of heat transfer and the efficiency of collector rises from 65% to 85% for water Cu nanofluid.

Miqdam et al., (2018) performed a numerical study on the effect of operating nanofluids of the photovoltaic thermal system (PV/T) on the convective heat transfer. The heat transfer coefficient for different nanofluids was higher than the conventional ones by 3.9% for SiO_2, 2.67% for CuO and 4.42% for Al_2O_3. The pressure drops higher than the numerical ones the reduction was 0.487% for CuO nanofluid and nanofluid it was 2.55% for Al_2O_3.

Benabderrahmane, (2016) did a 3D numerical investigation of heat transfer in a PTC receiver with longitudinal fins using different kinds of nanofluids. An operational temperature of 573 K and nanoparticle concentration of 1% in volume used for the study. The outer surface of the absorber receives a non-uniform heat flux (in which Monte Carlo ray tracing technique used to obtain it). A significant improvement of heat transfer is derived when the Reynolds number varies in the range $2.57\times10^4 \leq Re \leq 2.57\times10^5$ and the tube-side Nusselt number increases by 1.3 to 1.8 times.

Agabalaie (2017) examined the effect of different nanofluids in a parabolic solar collector. Puts the comparison of temperature, thermal efficiency and outlet average temperature for a conventional parabolic collector and a collector with nanofluids (water-silver and silver-copper). The results of the simulations demonstrated under the same working conditions the thermal efficiency upgraded from 27.8 to 95.2% for water and nanofluids, respectively. Moreover, the average outlet temperature increased from 33.2 to 97.8 K.

The nanofluid technology not limited to the a few applications rather it is used in various solar water-heating systems especially in FPC. **Luo et al.,,** (2014) presented the performance improvement of a nanofluid solar collector based on direct absorption collection (DAC) concepts. A 2D model built to analyze the radiation and conduction in the collector. The nanofluid flow horizontally from the right to the left in a solar collector covered with a glass plate. The simulation results in accordance with the experiments showed that the nanofluids improved the outlet temperature and efficiency by 30-100 K and 2-25% than the base fluid.

Ekramian et al., (2014) studied the numerical simulation of SFPC for the prediction of heat transfer coefficients and thermal efficiency of water and various nanofluids in SFPC.The author found the heat transfer coefficients and thermal efficiency of CuO/water nanofluid are greater than those of other nanofluids. The heat transfer coefficient of CuO /water nanofluid is about 4% and 2% higher than Al_2O_3/water and CNT/water nanofluids respectively.

Said et al., (2016) studied the energy and exergy efficiency of SFPC using PH treated Al_2O_3 nanofluid. The results revealed that nanofluids increased the energy efficiency by 83.5% for 0.3% v/v and 1.5 kg/min, whereas the exergy efficiency enhanced up to 20.3% for 0.1%v/v and 1 kg/min.

Delfani et al., (2014) did a Numerical Investigation of Nanofluid-based Solar Collectors. The radiative transfer and energy equations solved numerically. It found that the efficiency improvement of about 0.8% is obtained by adding 0.02 g/l carbon nanohorns (h=5 mm) to the base fluid (water) compare to a typical flat-plate collector. This increase is 9% and 17% for 0.05 g/l carbon nanohorns and collector heights 3 and 5 mm, respectively.

Rangababu et al., (2015) did the numerical and thermodynamic analysis to improve its performance of SFPC. Based on exergy analysis it has shown that the efficiency of SFPC has improved considerably. Heat transfer phenomenon inside the risers of SFPC analyzed numerically by developing a 3D model in commercial CFD software ANSYS FLUENT 14. They have proposed that the collector efficiency of CuO based SFPC increased by 22% as compared to water and 8% as compared to Al_2O_3.

Kumar et al., (2017) experimentally evaluated the SFPC using nanofluids. For 0.75% particle volume concentration at a mass flow rate of 0.025 kg/s, exergy efficiency for multi-walled carbon nanotube /water nanofluid enhanced by 29.32%. Similarly, by 21.46%, 16.67%, 10.86%, 6.97%, and 5.74%, for graphene/water, copper oxide/water, aluminum oxide /water, titanium oxide/water, and silicon oxide/water respectively instead of water as the base fluid.

Antony, (2017) put an effort on Performance Comparison of different Nanofluids in SFPC using Computational Fluid Dynamics (CFD). While comparing the maximum temperature is in the range of 59-61 ^{o}C for water, 61-65 ^{o}C for silicon carbide and 62-70 ^{o}C for aluminum nitride.

Sahi and Alrazzaq (2017) studied Experimental and numerical heat transfer of SFPC by using nanofluid. In addition, using nanoparticles Al_2O_3 with three different volume fraction (0.2, 0.4, and 0.6 %) for enhancement heat transfer of working fluid. The numerical CFD-Model did by using interfaces between laminar flow and heat transfer by COMSOL version 5.2a. The maximum temperature difference between inlet and outlet is 15.3 °C, at Nanofluid for the volume fraction of 0.6%.

Vincely and Natarajan (2017) studied the Performance enhancement of the thermosiphon flat plate solar water heater with CuO nanofluid. Experiments conducted on a thermosiphon type flat plate collector, inclined at 45°, for water heating application. The 3-D, steady state, conjugate heat transfer CFD analyses carried out using the ANSYS FLUENT 15.0 software. The nanofluid increases collector efficiency with increasing concentration. The highest efficiency enhancement of 5.7% observed for the nanofluid with $\zeta = 0.2$ having a mass flow rate of 0.0033 kg/s.

Khin et al., (2016) studied the theoretical analysis to determine the efficiency of a CuO-water nanofluid based-SFPC for the domestic SWH system in Myanmar. A mathematical model and a program, written in MATLAB code used for calculating the efficiency of SFPC for a domestic SWH system considering the weather conditions of a city in Myanmar. The author proposed that the use of the CuO-water nanofluid as a working fluid could improve the efficiency of SFPC up to 5% compared with water as a working fluid under the same ambient, radiant and operating conditions.

Nasrin and Alim (2015) investigated the effect of solar irradiance and the diameter of the riser pipe on the performance of SFPC. The water Cu nanofluid used as the working fluid inside the riser pipe of the solar collector. Finite Element Method using Galerkin's weighted residual scheme solves the governing differential equations with boundary conditions. The rate of heat transfer enhanced by 13% and 9% using 2% concentrated water-copper nanofluid and water respectively for rising solar irradiation (I) from 200 to 250 W/m^2 when D = 0.01 m. The output temperature of nanofluid becomes 312, 313, 315, and 317 K for nanofluid and 30, 310, 311 and 313 K for base fluid for I = 200, 215, 230 and 250 W/m^2, respectively. Additionally, the output temperature of nanofluid becomes 313, 312, 312 and 310 K for nanofluid and 310, 309, 308 and 307 K for base fluid D = 0.01m, 0.012, 0.013 and 0.15, respectively.

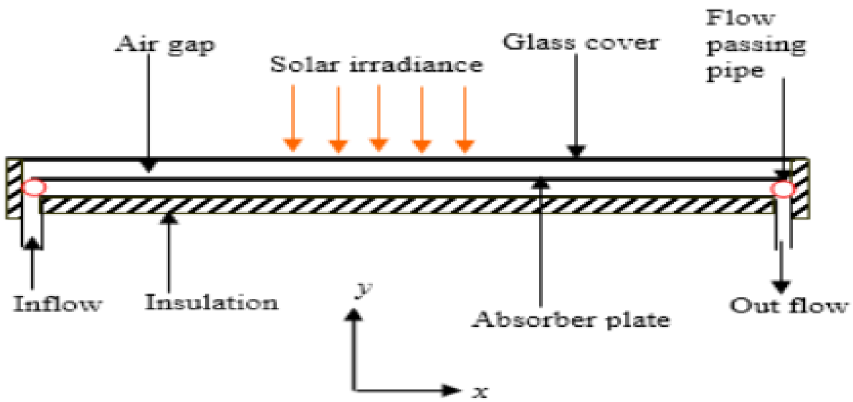

Figure 2.2 Systematic diagram of solar collector

Salavati et al., (2015) have performed an experimental investigation on SFPC using SiO_2 / EG-water nanofluids. With the increase of nanofluid concentration from 0 to 1%, the thermal efficiency increases approximately between 4 and 8%. The results explained the potential of SiO_2 nanoparticles to improve the efficiency of solar collectors despite its low thermal conductivity compared to other usual nanoparticles. SiO_2/water nanofluid (with a mass fraction of 1%) used by **Noghrehabadi et al.,** (2016) to perform an experimental investigation of the efficiency of square SFPC. The experimental setup shown in Fig.2.3 was used for sudy. At lower reduced temperature parameter $(T_i–Ta)/G_T$ values maximum efficiency of the water and SiO_2/water found to be 55.7 and 55.8%, respectively at a flow rate of 1.4 L/min.

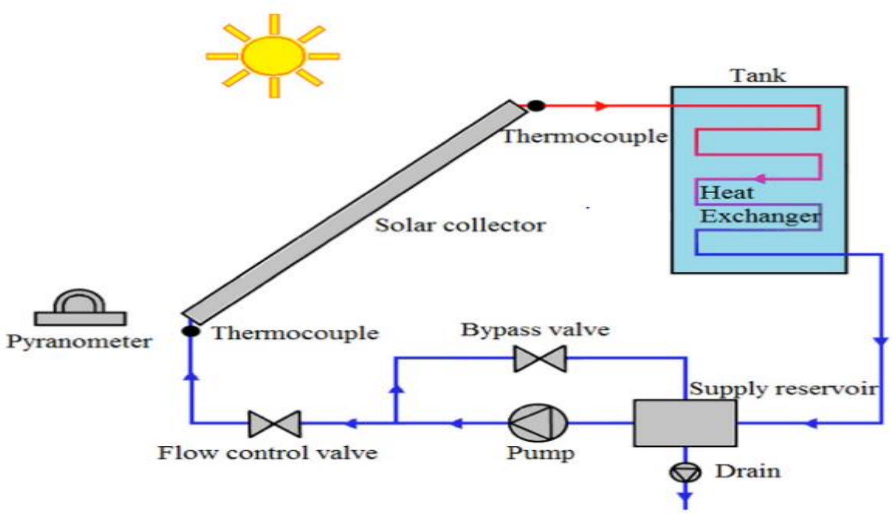

Figure 2.3 A schematic of the experimental setup.

Akhatov et al., (2017) come with the simulation results of the thermal performances of SFPC with nanofluid. The author shows the outlet temperature and gained useful energy of heat transfer fluid (SiO_2 + water with 5% concentration) depends on the flow rates (10, 15 and 20 L/h) at different ranges of incident solar radiation (500–1000 W/m^2).

Using the finite volume method **Nejad et al.,** (2017) have studied a numerical investigation of the laminar heat transfer in a three-dimensional SFPC. The authors found FPSC with Ag nanofluid shows the best thermal performance enhancement. The efficiency of a solar collector using Ag nanofluid with an inlet flow rate of 0.6 L/min increased by 17.65% compared to that of water. A small increment in pressure drop observed when using Ag nanofluids. **Sami** (2018) did a mathematical model to predict the thermal behavior of thermal solar collectors using nanofluids (AlO_2, CuO, and Fe_3O_4 and SiO_2). The model based upon energy conservation equations for nanofluids flow and at different mass flow rates (0.0107, 0.012, 0.005 and 0.001 kg/s). The result showed that the maximum efficiency of the solar panel occurs at 0.012 kg/s.

Hawwash, (2016) performed numerical and experimental verification of SFPC using nanofluid (double distilled water and alumina). Outdoor experiments conducted under the hot climate conditions in Egypt to test the performance of the FPSC, According to ASHRAE standard 86-93. The result indicated that using alumina nanofluid improves the collector thermal efficiency compared to DDW by about 3 and 18% at low and high-temperature differences.

Karanth et al., (2011) numerically simulated SFPC using DTRM (discrete Transfer Radiation Model). The results showed the differential temperature between the absorber plate and fluid keeps increasing with increase in flow velocity. Later, **Ammar et al.**, (2017) numerically studied the nanofluid heat transfer SiO_2 through a SFPC. CFD simulation is used in the analysis. The effectiveness of different vol.concentration of SiO_2 is compared with conventional water SFPC. Accordingly, the simulation result showed 10% of SiO_2 increase.

It can be noticed from the comprehensive literature review that most review concentrates only on single nanofluid. Since there are no sufficient numerical studies on the thermal efficiency of FPSC using different nanofluids as working fluids, there is no enough comparison between different nanofluids in the literature.

This study will focus on the thermal performance enhancement of flat-plate solar collector applying four different nanofluids, namely Al_2O_3, SiO_2, TiO_2 and CuO nanofluids with water as a base fluid at different volume fractions of (i.e. 1%, 2% and 3%). The numerical simulation is done by using CFD Fluent and MS Excel software and real meteorological data taken in Adama, Ethiopia. Whereas the experiment test is performed for water, 1% Al_2O_3 and 2% Al_2O_3.

CHAPTER THREE

DATA ANALYSIS and METHODOLOGY

3.0 Solar radiation estimation

Time series solar radiation data is important for modeling and design of solar radiation related devices or systems. Moreover, complete time series data is significant for performance prediction to ensure reliability of the system. However, this solar radiation data are not always available for every area, even if there is a weather station near the area, the data access is often limited. Furthermore, the available data may contain missing data for several days in the absence of measurement. Sometimes this missing data only occurred for some parameter in meteorological data set, while other parameters are complete data. This might happen due to sensor error or damage.

In Ethiopia, due to absence or malfunction of measuring instruments, reliable solar radiation data is not available. In the absence and scarcity of trustworthy solar radiation data, the use of an empirical model to predict and estimate solar radiation seems inevitable. These models use climatological parameters of the location under study. Among all such parameters, sunshine hours are the most commonly used.

3.1 Data collection

This study uses data of solar radiation and ambient temperature from Eastern and Central Oromia Meteorological Service Center (ECOMSC) for the targeted area (Adama city). Solar radiation data available in ECOMSC is from Pyranometer SP-Lite and CMP3 (W/m^2), and only sunshine hours with a few years global radiation. Beam and diffuse solar radiation data calculated by using solar energy empirical relations, available global radiation data, location (latitude and longitude) and weather condition of Adama.

3.2 Estimation of solar radiation on horizontal surface

3.2.1 Monthly average daily global radiation on a horizontal surface

Angstrom first proposed the relation between solar radiation and sunshine duration in 1924 (Duffie and Beckman, 1991). Prescott presented the modified model in 1940. The popular Angstrom-Prescott Model was given by:

$$\frac{\bar{H}}{\bar{H}_o} = a + b\frac{\bar{n}_s}{\bar{N}_s} \quad \ldots\ldots\ldots\ldots\ldots\ldots\ldots\ldots\ldots\ldots\ldots\ldots (3.0)$$

Where $\bar{H}$ = monthly average daily global radiation (Wh/m^2/day),

$\bar{H}_o$= monthly average daily extraterrestrial radiation at the specific location,

$\bar{n}_s$ = monthly average daily maximum bright sunshine duration in hours,

$\bar{N}_s$= actual sunshine duration in a day in hours, and , are empirical coefficients.

These coefficients are location specific. The coefficients a and b are empirical constants, (Values are obtained by regression).

Monthly average daily extraterrestrial radiation is calculated from the following equation:

$$\bar{H}_o = \left(\frac{24*360}{\pi} I_{SC}\right)\left[1.0 + 0.033cos\left(\frac{360N}{365}\right)\right]\left[cos\varphi cos\delta sin\bar{\omega}_s + \frac{\pi\bar{\omega}_s}{180^o} sin\delta sin\varphi\right] \ldots\ldots\ldots\ldots\ldots (3.1)$$

The regression parameters are determined by (Duffie and Beckman, 1991):

$$a = -0.11 + 0.235\cos\varphi + 0.323\left(\frac{\bar{n}_s}{\bar{N}_s}\right) \ldots\ldots\ldots\ldots\ldots\ldots\ldots\ldots\ldots\ldots (3.2)$$

$$b = 1.449 - 0.533\cos\varphi - 0.694\left(\frac{\bar{n}_s}{\bar{N}_s}\right) \ldots\ldots\ldots\ldots\ldots\ldots\ldots\ldots\ldots\ldots (3.3)$$

Where, I_{SC} = the solar contact =1.367 kW/m^2, $\bar{\omega}_s$= sunrise hour angle

Declination angle

Declination angle is the angle between the earth’s equatorial plane and the line drawn between the center of the earth and the sun. The solar declination is calculated according to the following equation:

$$\delta = 23.45 sin\left[\frac{360}{365}(284 + N)\right] \quad \text{(3.4)}$$

Where: N = the representative days of the month.

Sunset hour angle

The sunset hour angle is calculated using the following equation:

$$\bar{\omega}_s = \cos^{-1}(tan\delta tan\varphi) \quad \text{(3.5)}$$

Sunshine duration

The Sunshine duration in a day

$$\bar{N}_s = \frac{2}{15}\bar{\omega}_s \quad \text{(3.6)}$$

3.2.2 Monthly average daily diffuse radiation on a horizontal surface

The solar radiation received from the sun after its direction has been changed by scattering the atmosphere. Diffuse radiation is referred to in some meteorological literature as sky radiation or solar sky radiation. The monthly average daily diffuse radiation on a horizontal surface can be determined from the monthly average daily global radiation on a horizontal surface and the number of bright sunshine hours.

$$\frac{\bar{H}_d}{\bar{H}} = 0.931 - 0.814\frac{\bar{n}_s}{\bar{N}_s} \quad \text{(3.7)}$$

3.2.3 Monthly average hourly global radiation on a horizontal surface

The monthly average hourly global radiation on a horizontal surface can be calculated from the knowledge of the monthly average daily global radiation on a horizontal surface (Duffie and Beckman, 1991).

$$\frac{\bar{I}}{\bar{H}} = \frac{\pi}{24}(a + b\cos\bar{\omega})\frac{\cos\bar{\omega} - \cos\bar{\omega}_s}{\sin\bar{\omega}_s - \frac{\pi}{180}\bar{\omega}_s\cos\bar{\omega}_s} \quad \text{(3.8)}$$

Where: $a=0.409+0.5016\sin(\bar{\omega}_s - 60)$ ……… (3.8a)

$b=0.6609+0.47676\sin(\bar{\omega}_s - 60)$ ……… (3.8b)

3.2.4 Monthly average hourly diffuse radiation on a horizontal surface

The monthly average hourly diffuse radiation on a horizontal surface can be calculated from the knowledge of the monthly average daily diffuse radiation on a horizontal surface.

$$\frac{\bar{I}_d}{\bar{H}_d} = \frac{\pi}{24}\frac{\cos\bar{\omega} - \cos\bar{\omega}_s}{\sin\bar{\omega}_s - \frac{\pi}{180}\bar{\omega}_s\cos\bar{\omega}_s} \quad (3.9)$$

Hour angle (ω)

The hour angle of a point on the earth's surface is defined as the angle through which the earth would turn to bring the meridian of the point directly under the sun. Hour angle and solar time in hour are related as:

$$\omega = (t - 12) * 15° \quad (3.10)$$

3.2.5 Monthly average hourly beam radiation on a horizontal surface

Beam Radiation is the solar radiation received from the sun without having been scattered by the atmosphere. Beam radiation is often referred to as direct solar radiation. The beam radiation incident on a surface is the deference between global radiation and diffuse radiation is given by :

$$I_b = I - I_d \quad (3.11)$$

Collector tilt angle

The tilt of a collector is the angle between the collector and the local horizontal. In most solar water heating applications, a tilt of approximately latitude plus 10º to 15º is near optimum because it is necessary to favor the summer season, when the collector operates under adverse conditions (due to lower ambient temperature) and load is greatest (John & Howell, 1982.).

$\beta = \varphi \pm 15°$ = 8.514477º +10º

= 18.514477º ≅ 20º

3.3 Total radiation on tilted surface

It can be assumed that the combination of diffuse and ground-reflected radiation is isotropic (Hotel and Woertz, {1942}). With this assumption, the sum of the diffuse from the sky and the ground-reflected radiation on the tilted surface is the same regardless of orientation, and the total radiation on the tilted surface is the sum of the beam contribution calculated as I_bR_b and the diffuse on a horizontal surface, I_d.

The radiation on the tilted surface was considered to include three components: beam, isotropic diffuse and solar radiation diffusely reflected from the ground (Liu and Jordan, {1963}) as shown in Fig.3.1. The tilted surface has a view factor to the ground $F_{c-g} = (1-\cos\beta)/2$, and if the surroundings have a diffuse reflectance of ρ_g for the total solar radiation, the reflected radiation from the surroundings on the surface will be $I\rho_g(1-\cos\beta)/2)$.

The radiation on the tilted surface was given as:

$$I_T = I_bR_b + I_d\left(\frac{1+\cos\beta}{2}\right) + I\rho_g\left(\frac{1-\cos\beta}{2}\right) \quad (3.12)$$

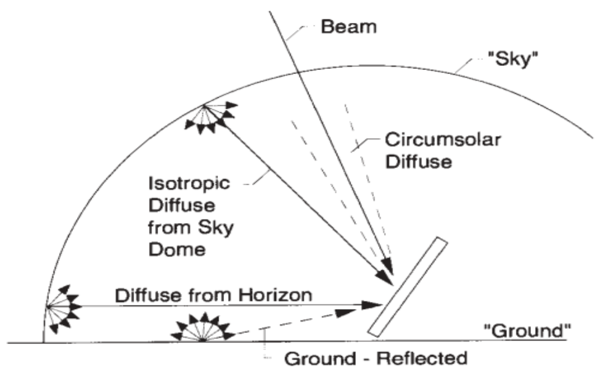

Figure 3.1 Components of radiation (Duffie and Beckman, 1991).

The ratio of the direct solar radiation falling on tilted surface to that falling on a horizontal surface is called **the tilt factor** R_b for the beam or direct radiation. The R_b for the collector surface facing south (γ=0˚) will be given as:

$$R_b = \frac{\cos(\beta-\varphi)\cos\delta\cos\omega+\sin(\beta-\varphi)\sin\delta}{\cos\beta\cos\delta\cos\omega+\sin\beta\sin\delta} \quad (3.13)$$

3.4 Estimation of diurnal cycle variation of temperature

Ambient temperature is one the critical parameters in every solar energy analysis. For climatological purposes, many of the available data consist of only the daily minimum and maximum temperatures. For many models, it is often useful to obtain an approximation of hourly temperature for a particular location and time of the year. For matter of study the model presented by Wilk-Erickson et al., (1983) used.

According to this model, the day is divided into 3 segments:

a. midnight to sunrise + 2 h,
b. daylight hours and
c. sunset to midnight

The method assumes a change from night to day temperature at sunrise + 2 h, and the night temperatures are linear with time. In addition to the current day's T_{MAX} and T_{MIN}, the method requires the T_{MAX} and T_{MIN} of the previous day and the T_{MIN} of the following day. The hourly temperatures are given by

a) Midnight to sunrise + 2 h

$$\mathrm{T_{AU}} = \frac{\pi(SET_{n-1} - RISE_{n-1} - 2)}{SET_{n-1} - RISE_{n-1}} \quad \text{(3.14a)}$$

$$\mathrm{T_{LIN}} = (\mathrm{T_{MIN}})_{n-1} + ((\mathrm{T_{MAX}})_{n-1} - (\mathrm{T_{MIN}})_{n-1})\sin(T_{AU}) \quad \text{(3.14b)}$$

$$SLOPE = \frac{(T_{LIN} - (\mathrm{T_{MIN}})_{n})}{24 - SET_{n-1} + RISE_{n} + 2} \quad \text{(3.14c)}$$

$$T(H) = \mathrm{T_{LIN}} - SLOPE(H + 24 - SET_{n-1}) \quad \text{(3.14d)}$$

Sunset to midnight

$$\mathrm{T_{AU}} = \frac{\pi(SET_{n} - RISE_{n} - 2)}{SET_{n} - RISE_{n}} \quad \text{(3.15a)}$$

$$\mathrm{T_{LIN}} = (\mathrm{T_{MIN}})_{n} + ((\mathrm{T_{MAX}})_{n} - (\mathrm{T_{MIN}})_{n})\sin(T_{AU}) \quad \text{(3.15a)}$$

$$SLOPE = \frac{(T_{LIN} - (\mathrm{T_{MIN}})_{n+1})}{(24 - SET_{n} + RISE_{n+1} + 2)} \quad \text{(3.15b)}$$

$$T(H) = \mathrm{T_{LIN}} - SLOPE(H - SET_{n}) \quad \text{(3.15c)}$$

Daylight hours

$$\mathrm{T_{AU}} = \pi(H - RISE_{n} - 2)(SET_{n} - RISE_{n}) \quad \text{(3.16a)}$$

$$T(H) = (\mathrm{T_{MIN}})_{n} + ((\mathrm{T_{MAX}})_{n} - (\mathrm{T_{MIN}})_{n})\sin(\mathrm{T_{AU}}) \quad \text{(3.16b)}$$

Where, T_{AU}, T_{LIN}, SLOPE are temporary variables in calculations

T (H) = temperature at hour H

n = current day of the year (1-365)

RISE = time of sunrise (h)

SET= time of sunset (h).

The ambient temperature variation for June 11 2018 is shown in Fig.3.2. However, for each representative months the hourly ambient temperatures are listed in table form in APPENDIX (Table A2)

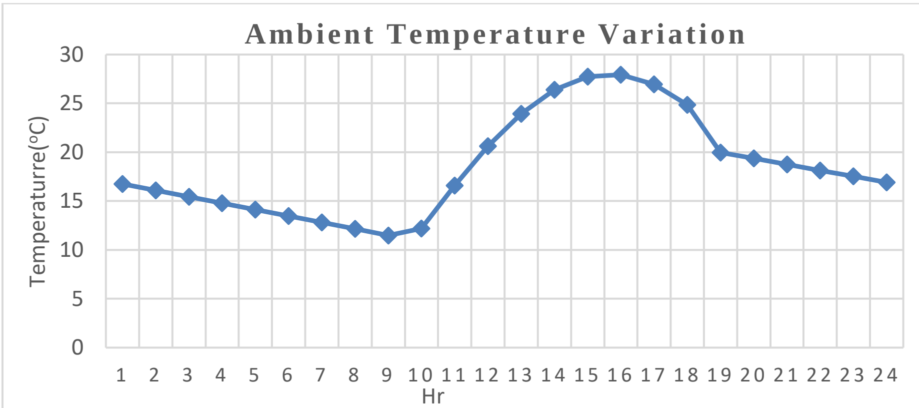

Figure 3.2 Ambient temperature variation for June 11, 2018.

The ambient temperature variation for June 11 2018 shown in Fig.3.2 is selected for study because, the minimum solar radiation occur in June. As shown from Fig.3.2 the night ambient temperature is linear with time for a given location. The effect of ground reflectance is given in Table 3.1.

Table 3.1 The ground reflectance

Ground cover	**Reflectivity (ρ_g)**
Water (large incidence angles)	7%
Coniferous forest (winter)	7%
Bituminous and gravel roof	13%
Dry bare ground	20%
Green grass	26%
Dry grassland	20–30%
Desert sand	40%
Light building surfaces	60%
Weathered concrete	22%

3.5 Conceptual frame work

The assembly and drawing of setup shown in Fig.3.3 and Fig.3.4 are done on solid work software respectively. The setup has three basic units i.e collector, pump and heat exchanger.

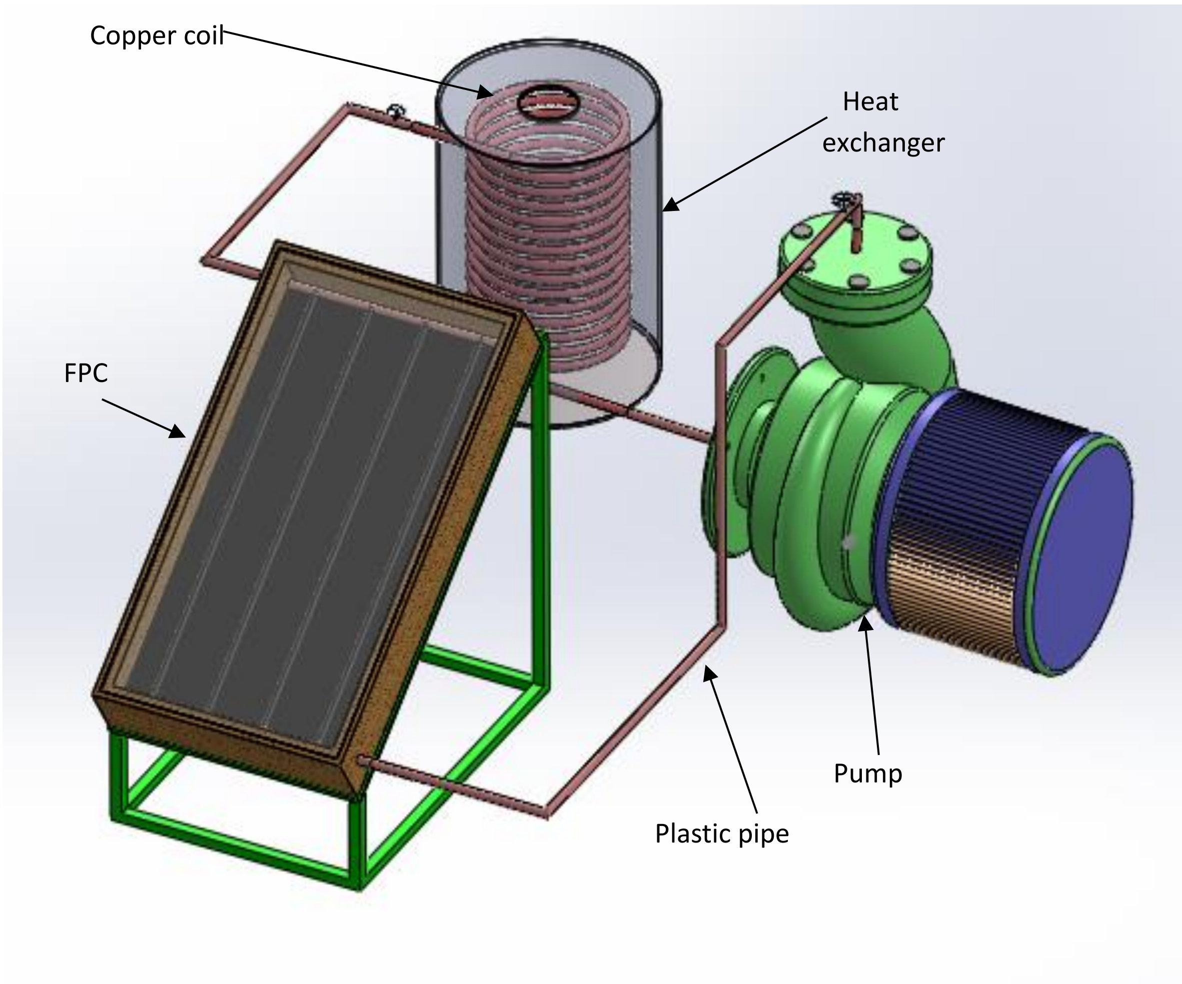

Figure 3.3 Solar flat plate collector system assembly

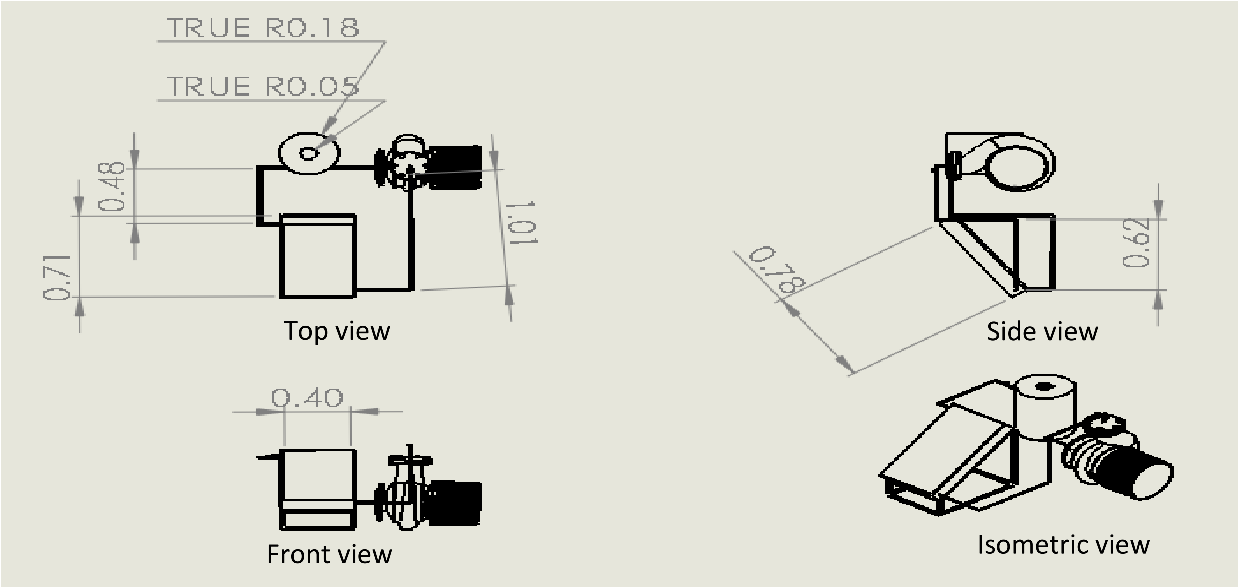

Figure 3.4 Solar flat plate collector system drawing views (all dimension is in {m})

3.6 Solar flat plate collector specification

The specific parameters shown in Table 3.2 was chosen depend the availability and cost of nanoparticles. If the collector size become large the amount of nanoparticles needed is also more. So for experimental porpuse the collector area become small purposely.

Table 3.2 Solar flat plate collector specification

No.	Parameters	Symbol	Magnitude
1.	Occupied area, absorption area	A_c	0.28 m^2
2.	Diameter of upper and lower header, OD		12.5 mm
3.	Length of the upper and lower header		400 mm
4.	length of the riser,	L	700 mm
5.	Diameter, OD	OD	14.5 mm
6.	Plate thickness	t_p	2 mm
7.	Distance b/n tubes	r	75 mm
8.	Tube inside diameter	d	12.5 mm
9.	Air gap thickness	t_{pg}	20 mm
10.	Plate thermal conductivity	k_p	385 W m^{-1} $^oC^{-1}$
11.	Collector slope angle	β	20^0
12.	Thickness of back insulation	t_b	0.03 m
13.	Back insulation thermal conductivity	k_b	0.014 W/m K
14.	Thickness of collector		0.075 m
15.	Mass flow rate	$\dot{m}$	0.0137 kg/s

3.7 Experimental setup

An experimental setup was developed in order to evaluate the performance of the SFPC using nanofluid as shown in Fig.3.6. A window glass having a length of 0.91 m and width of 0.505 m is used as transparent cover glass. A 0.80 mx0.45 mx2 mm thick copper plate coated black color used as absorber plate and a copper tube of 0.0125 m is used as a riser and header as shown in Fig.3.5.

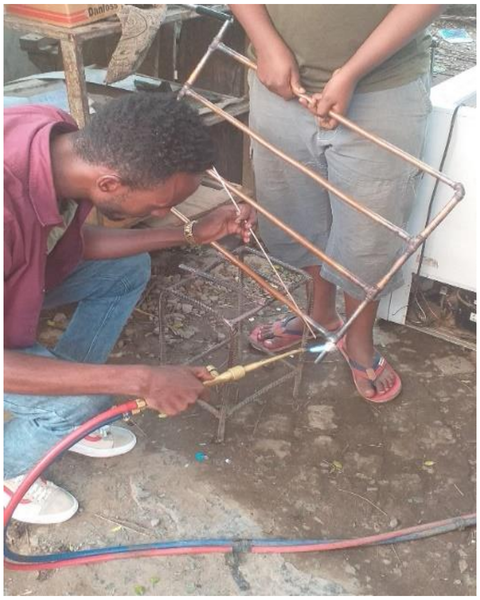

Figure 3.5 The image of welding the riser and header with elbows at joints using oxy-acetylene welding

The parallel flow configuration shown in Fig.3.5 is used instead of serpentine flow configuration. This is due to the fact that the heat removal factor in case of parallel flow configuration is greater than that of serpentine flow configuration at a given mass flow rate Malvi et al., (2017). The wooden frame has the dimension of 0.94 m length, 0.54 m width and 0.105 m. The wooden plate is used as insulator at the bottom of absorber plate. The 0.5 Hp water pump is used to pressurize and circulate water. Another component in the setup is a heat exchanger part, which contains 3 L water bucket and a copper coil. A copper coil is tube coil, which passes heat from circulating hot fluid inside it to the bucket water.

There are two-gate valve in a setup: one at the outlet of pump and one at the inlet of the copper coil in the bucket. These gate valves control the mass flow rate in the circuit. The rubber tube is used between collector, pump and heat exchanger. The amount of water circulating is 1500 gm. A K-type thermocouple was used to measure the temperature in the bucket.

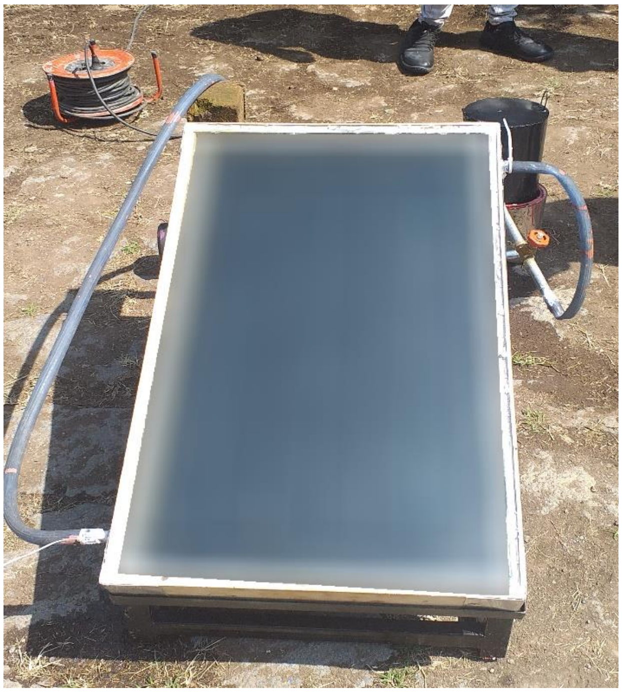 a).  b).

Figure 3.6 Experimental setup

Aluminum oxide nanoparticle, which has an average diameter of 27-32 nm, is mixed with circulating water to make nanofluid. The solar radiation is incident on the SFPC and the circulating fluid inside the copper tube absorbs the heat from the solar radiation. The circulating fluid then heats the water inside the bucket water while circulating inside the copper tube coil kept in the bucket.

3.8 Synthesis of aluminum oxide

In order to synthesise alumina, sol-gel method is used. Aluminum nitrate ($(Al(NO_3)_3.9H_2O$) shown in Fig.3.7, distilled water (DW), citric acid ($C_6H_8O_7$), ethylene glycol and ethanol (C_2H_5OH) and are used as raw material specifically for this purpose. Initially 0.1mol of aluminum nitrate and 30 mL ethylene glycol was gradually added to the aqueous alcoholic solution including 100 mL of DW and 100mL of ethanol, and then it is placed on a hot plate (Rajaeiyan, 2013). 0.3mol citric acid dissolved in 40 mL of DW was added to the solution. Then the solution is continuously stirred at 40 ℃ for 15 min until colloidal solution is prepared. Next, the solution was placed on water bath at 80 ℃ to evaporate solvent and prepare gel.

After 18 hr, the aerogel was placed on hot plate at 120 ℃ for 4hr the obtained sol-gel precursors was heated in oven for 3 hr at 200 ℃. Later the dried sol gel was grinded into powder and the brown powders was kept in furnace for 2 hr. at 1000 ℃. Finally, the fine aluminum oxide was obtained as shown in Fig.3.9. To get the required amount of Al_2O_3, the same steps can be followed.

Specification of Aluminum Nitrate

M.W. 375.13	
Assay	Min.98.0%
Chloride (Cl)	Max.0.005%
Sulphate (SO4)	Max.0.01%
Sodium (Na)	Max.0.01%
Iron (Fe)	Max.0.005%
Potassium (K)	Max.0.01%

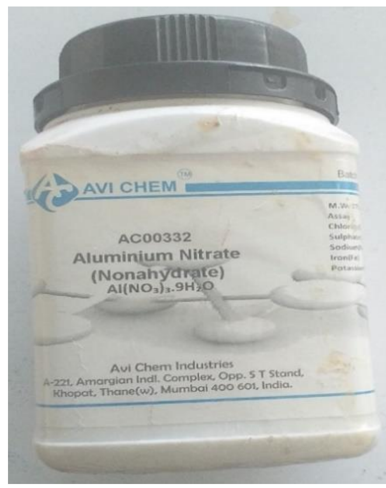

Figure 3.7 Specification of aluminum nitrate

The XRD test was done for this nanoparticle in Adama Science and Technology University, Material Science laboratory and the result was discussed in next chapter.

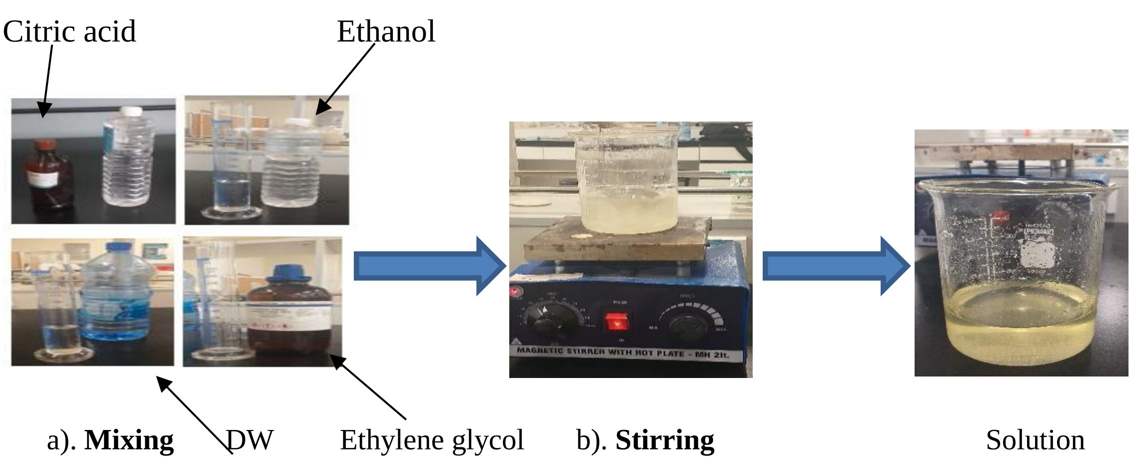

Figure 3.8 Solution preparation.

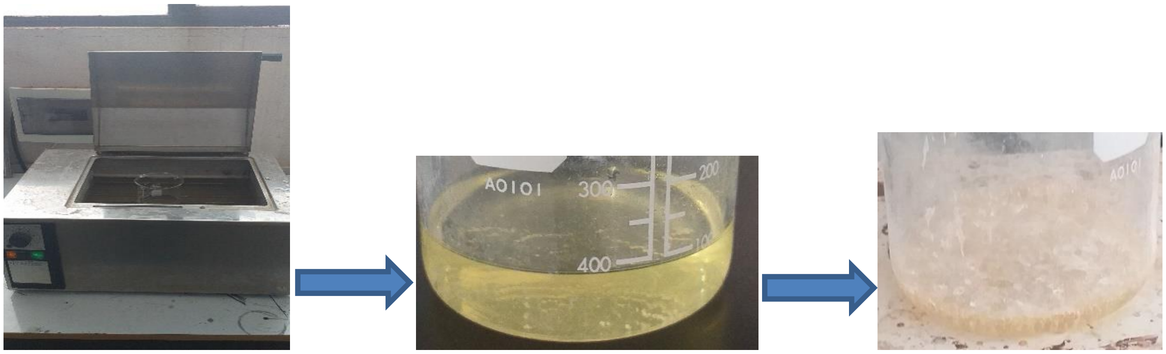

c). Evaporating sovent Sol-gel Sol-precurser

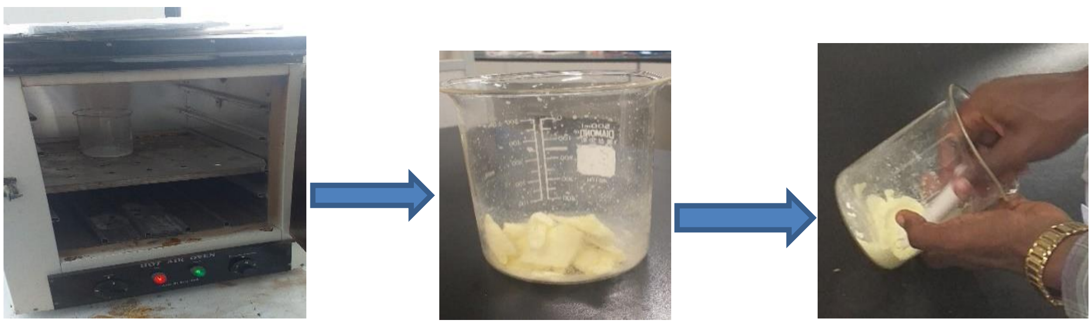

d). Drying in oven Dried sol-precurcer **e). Grinding**

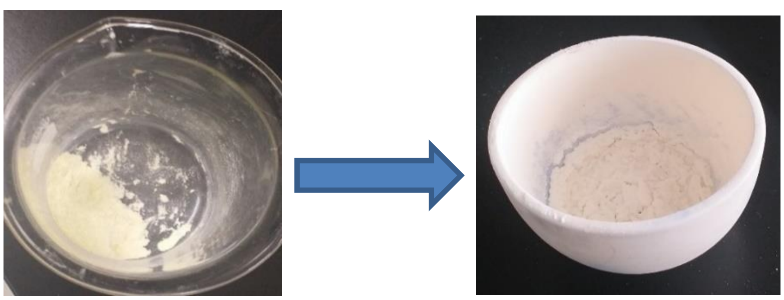

Sol powder **f).** After **heat-treating** in furnace at 1000 ℃ for 2hr.

Figure 3.9 Drying and grinding.

3.9 Nanofluid preparation

In present study, two-step process method of preparing nanofluid was used. The one-step process consists of simultaneously making and dispersing the particles in the fluid. In this study, 1% and 2% vol. concentration of Al_2O_3 in water is used for study. In order to increase dispersion and lowering aggregation the solution is sonicated with Ultrasonic Cleaner UC-20 as shown in

Fig.3.10. The confirmed ways for minimizing aggregation and clustering nanoparticles and improve suspension are to use high shear disperser and ultrasonic vibrator Hawwash et al. (2016).

Figure 3.10 Nanofluid sonication

In order to describe thermal performance test procedure for flat plate collector Indian standard (COLLECTOR TEST STANDARD EN 12975) used in this study. In this standard the instantaneous efficiency for various combinations of inlet temperature, ambient temperature and solar radiation are used to determine thermal performance of SFPC. The experimental measurement is performed under steady and quasi steady state. Fig.3.11 shows measurement taken for different working fluids at noon. Test is done in September (24-26), 2019.


a).

b).

c).

Figure 3.11 Outlet Temperature at noon a). Water, b). 1% Al_2O_3 and c). 2% Al_2O_3.

3.10 Mathematical formulation

The analysis of solar flat plate collector depends on the flow distribution in the riser. The laminar flow assumption gives the uniform flow and temperature distribution across each riser tubes (Dawit & Robi, 2016). The CFD model is developed to predict the temperature distribution in absorber plate and in single riser tube attached to the center of the absorber tube, and heat transfer coefficient for each nanofluids.

The flow domain consists of an absorber plate and circular absorber tube. Absorber plate of 700 mm length, 100 mm wide and 2 mm in thickness is used. A circular absorber tube is attached to the center of the absorber plate and the pipe has 12.5 mm internal diameter with a thickness of 1 mm. The glass transmittance and absorber plate absorptance $\{(\alpha\tau_g) = 0.9\}$ is considered and the domain is more simplified to absorber plate, tube and fluid part as shown Fig.3.12. The water tube has placed centrally and the water enters the tube from its back end.

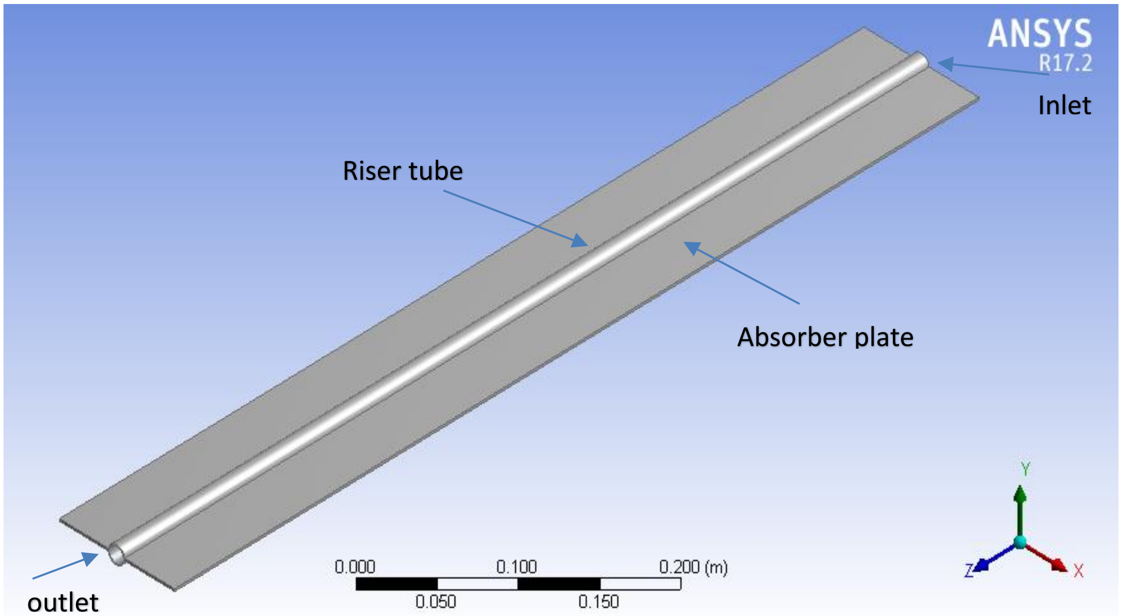

Figure 3.12 Flow domain geometry

The geometric dimensions of the flow domain geometry shown in Fig.3.12 is given in Table 3.3. The dimensions are used in ANSYS FLUENT 17.2 for numerical simulation.

Table 3.3 Design parameters of solar collector flow domain.

Geometric parameters in (mm)	Absorber plate (mm)	Absorber tube (mm)
Length	700	700
Width	100	-
Diameter	-	12.5
Thickness	2	1

3.10.1 Assumptions

I. The nanofluids used in SFPC are very thins (≤ 50nm), and then the mixture may easily fluidized and considered as single-phase fluid (Maouassi, 2017).

II. Thermal equilibrium and slip between the phases are negligible and the thermal properties are calculated from the classical correlation of the mixture (Maouassi, 2017).

III. The fluid is a continuous medium and incompressible.

IV. The flow is forced flow of nanofluids under the laminar and steady flow.

3.10.2 Governing equations

We can use CFD (computational fluid dynamics) to solve the full set of equations of motion (continuity plus Navier–Stokes) throughout the whole flow field. Based on the above assumptions and approximations for the governing equations are:

1. Continuity equation (conservation of mass)

The general continuity equation is given by:

$$\nabla . \rho\vec{V} + \frac{\partial \rho}{\partial t} = 0 \quad (3.17)$$

Since velocity varies along the flow direction u = u (x) for incompressible fluid flow;

$$\frac{\partial(\rho_{nf} u_j)}{\partial x_j} = 0 \quad (3.18)$$

Where the i and j represent direction unit vector along the x (longitudinal) and y direction.

2. **Momentum equation(Navier-stoke equation**):

For simplification the y and z component's represents the radial and the tangential components respectively while the x component represent the longitudinal direction of flow direction, since the former two will be removed later using scale analysis.

x-momentum equation:

$$\left(u\frac{\partial u}{\partial x}+v\frac{\partial u}{\partial y}+w\frac{\partial u}{\partial z}\right)=-\frac{1}{\rho}\frac{\partial P}{\partial x}+\frac{\mu}{\rho}\left(\frac{\partial^2 u}{\partial x^2}+\frac{\partial^2 v}{\partial y^2}+\frac{\partial^2 w}{\partial z^2}\right) \quad (3.19)$$

y-momentum equation:

$$\left(u\frac{\partial v}{\partial x}+v\frac{\partial v}{\partial y}+w\frac{\partial v}{\partial z}\right)=-\frac{1}{\rho}\frac{\partial P}{\partial y}+\frac{\mu}{\rho}\left(\frac{\partial^2 v}{\partial x^2}+\frac{\partial^2 v}{\partial y^2}+\frac{\partial^2 w}{\partial z^2}\right) \quad (3.20)$$

z-momentum equation:

$$\left(u\frac{\partial w}{\partial x}+v\frac{\partial w}{\partial y}+w\frac{\partial w}{\partial z}\right)=-\frac{1}{\rho}\frac{\partial P}{\partial z}+\frac{\mu}{\rho}\left(\frac{\partial^2 v}{\partial x^2}+\frac{\partial^2 v}{\partial y^2}+\frac{\partial^2 w}{\partial z^2}\right) \quad (3.21)$$

Using Scale Analysis it can be shown that the y-momentum and z-momentum equation reduces to

$$-\frac{1}{\rho}\frac{\partial P}{\partial y}=0 \quad (3.22)$$

$$-\frac{1}{\rho}\frac{\partial P}{\partial z}=0 \quad (3.23)$$

Thus, the *x*-component of the Navier–Stokes equation becomes Karanth et al. (2011)

$$\rho_{nf}\frac{\partial u_i u_j}{\partial x_j}=-\frac{dP}{dx}+\frac{\partial}{\partial x_j}\left(\mu_{nf}\frac{\partial u_i}{\partial x_j}\right) \quad (3.24)$$

Energy equation

The energy equation derived assuming temperature gradients $\frac{\partial T}{\partial x_j} \gg \frac{\partial T}{\partial x_i}$ (boundary layer approximation) (Karanth, Vasudeva, & Yagnesh, 2011)

$$\left(\frac{\partial u_j T}{\partial x_j}\right)=\alpha_{nf}\left(\frac{\partial^2 T}{\partial {x_j}^2}\right) \quad (3.25)$$

Where x_j - represent the radial direction component.

α_{nf} - represent thermal diffusivity of nanofluids

3.10.3 Boundary conditions

The velocity inlet and outflow boundary conditions are specified at inlet and outlet respectively.

- At inlet x = 0: $u(0, y) = U_\infty$, $u(0, y) = T_\infty$
- At pipe wall (interface) y = R: $u(x, R) = 0$, $v(0, R) = 0, q(0, R) = q_s$
- As $y \to r$: $u(x, r) = U_\infty$ $T(x, r) = T_\infty$

The glass made up of borosilicate, which has a thermal conductivity of 1.14 W/m-K, specific heat of 750 J/kg-K and a refractive index of 1.47 is exposed to the solar radiation. The analysis is carried out for June 11, 2019 at 1pm of the day. The interface between the water or nanofluids and the absorber tube is defined as the coupled wall.

3.11 Internal flow analysis

The internal flow configuration represents a convenient geometry for heating and cooling fluids used in chemical processing environment control and energy conversion technology.

Developing an appreciation for the physical phenomenon (solar harvesting system) associated with the internal flow and obtaining the convection coefficients for flow conditions of practical importance are very essential. This can be done first by considering velocity (hydrodynamic) effects pertinent to internal flows and determine fluid temperature variation in the flow directions. Finally, the correlations for estimating the convection heat transfer coefficient are presented for laminar flow conditions (Incropera & DeWitt, 2007).

The fluid velocity in a pipe changes from zero at the surface because of the no-slip condition to a maximum at the pipe center. The value of the average velocity u_m at some stream-wise cross-section shown in Fig.3.13 is determined from the requirement that the conservation of mass principle is satisfied. That is,

$$\dot{m} = \rho u_m A_c = \int_{A_c} \rho u(r) dA_c \quad \ldots\ldots (3.26)$$

Where $\dot{m}$ the mass flow rate, ρ is the density, A_c is the cross-sectional area, and u(r) is the velocity profile.

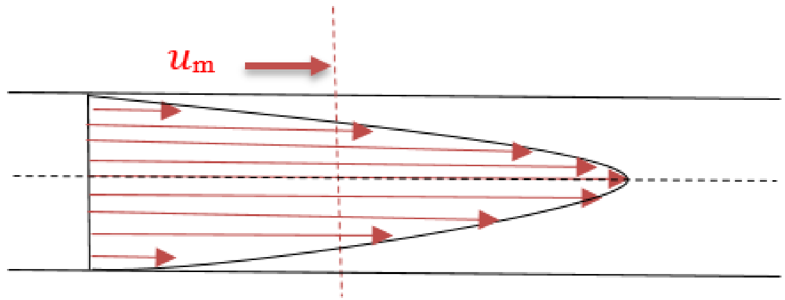

Figure 3.13 Average velocity u_m for fully developed laminar pipe flow, $\boldsymbol{u_m}$ is half of maximum velocity.

Then the average velocity for incompressible flow in a circular pipe of radius R can be expressed as:

$$u_m = \frac{2}{R^2}\int_0^R u(r)rdr \quad (3.27)$$

Assuming steady, incompressible flow and tube of uniform cross-sectional area, the mass flow rate and mean velocity are independent of the length of the tube.

Skin friction coefficient

The skin friction coefficient for the fully developed laminar flow in a circular tube is given by Karanth (2011).

$$\lambda = \tau_s \frac{\rho u_m^2}{2} \quad (3.28)$$

3.11.1 **Flow conditions**

When dealing with internal flows it is important to be cognizant of the extent of the entry region, which depends on whether the flow is laminar or turbulent. The laminar flow regimes are characterized by smooth streamlines and highly ordered motion. While turbulent in the second case, where it is characterized by velocity fluctuations and highly disordered motion.

The transition from laminar to turbulent flow does not occur suddenly; rather, it occurs over some region in which the flow fluctuates between laminar and turbulent flows before it becomes fully turbulent.

Reynolds number

The flow regime depends mainly on the ratio of inertial forces to viscous forces in the fluid. This ratio is called the Reynolds number and is expressed for internal flow in a circular pipe as: (Incropera & DeWitt, 2007)

$$Re = \rho u_m D/\mu \quad \text{……………} \quad (3.29)$$

Where u_m average flow velocity (m/s), D characteristic length of the geometry (diameter in this case, in m), and μ dynamic viscosity of the fluid (m^2/s).

The transition from laminar to turbulent flow depends on the degree of disturbance of the flow by surface roughness, pipe vibrations, and fluctuations in the flow. Under most practical conditions, the flow in a circular pipe is

- Laminar for Re ≤ 2300,
- Transitional for 2300 ≤ 4000, and
- Turbulent for Re ≥ 4000,

Entrance region

The region from the pipe inlet to the point at which the boundary layer merges at the centerline is called the hydrodynamic entrance region. The velocity profile in the fully developed region is parabolic in laminar flow and somewhat flatter (or fuller) in turbulent flow due to eddy motion and more vigorous mixing in the radial direction. The time-averaged velocity profile remains unchanged when the flow is fully developed, and thus

$$\frac{\partial u(r,x)}{\partial x} = 0 \longrightarrow \quad u = u(r) \quad \text{……………} \quad (3.30)$$

The wall shear stress is the highest at the pipe inlet where the thickness of the boundary layer is smallest, and decreases gradually to the fully developed value. Therefore, the pressure drop is higher in the entrance regions of a pipe, and the effect of the entrance region is always to increase the average friction factor for the entire pipe. This increase may be significant for short pipes but is negligible for long ones.

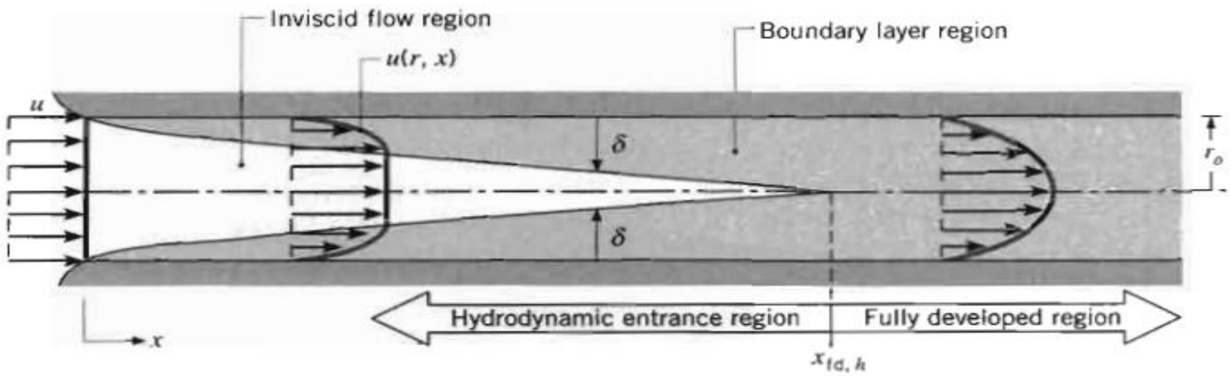

Figure 3.14 Laminar hydrodynamic boundary layer development in circular tube (Incropera & DeWitt, 2007).

The hydrodynamic entry length is usually taken to be the distance from the pipe entrance to where the wall shear stress (and thus the friction factor) reaches within about 2 percent of the fully developed value.

For laminar flow,

$$x_{fd} \cong 0.05ReD \quad \ldots\ldots\ldots\ldots\ldots\ldots\ldots\ldots\ldots\ldots\ldots\ldots\ldots\ldots (3.31)$$

For turbulent flow,

$$x_{fd} \cong 1.359(Re)^{1/4}D \quad \ldots\ldots\ldots\ldots\ldots\ldots\ldots\ldots\ldots\ldots\ldots\ldots (3.32)$$

The entry length for 0.01 m/s inlet velocity and 12.5 mm internal diameter was 0.0937 m which is less than collector length of 0.7 m.

3.11.2 Velocity profile in fully developed region

The form of the velocity profile may readily be determined for the laminar flow of an incompressible, constant property fluid in the fully developed region of a circular tube. In fully developed laminar flow, each fluid particle moves at a constant axial velocity along a streamline and the velocity profile u(r) remains unchanged in the flow direction. There is no motion in the radial direction, and thus the velocity component in the direction normal to flow and the velocity gradient of the axial velocity component is everywhere zero.

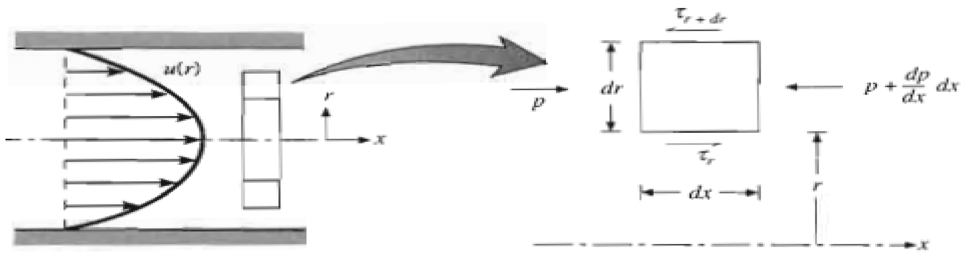

Figure 3.15 Force balance on differential element of fully developed, laminar flow in absorber riser tube (Incropera & DeWitt, 2007).

The net momentum flux is everywhere zero in this region. Hence, the momentum conservation requirement reduces to a simple balance between shear and pressure forces in the flow. For the annular differential element,

$$\tau_r(2\pi r dx) - \left\{\tau_r(2\pi r dx) + \frac{d}{dr}\left(\tau_r(2\pi r dx)\right)dr\right\} + \mathrm{p}(2\pi \mathrm{rdr}) - \{\mathrm{p}(2\pi \mathrm{rdr}) + \frac{d}{dx}[\mathrm{p}(2\pi \mathrm{rdr})]dx\} = 0 \quad (3.33)$$

Which reduced to

$$-\frac{d}{dr}(r\tau_r) = r\frac{dp}{dx} \quad (3.34)$$

Substituting for newton law of cooling ($\tau_r = -\mu\frac{du}{dr}$), applying boundary equation and simplifying, the equation is reduced to

$$\frac{u(r)}{u_m} = 2[1 - \left(\frac{r}{r_o}\right)^2] \quad (3.35)$$

3.11.3 **Pressure loss and head loss**

A quantity of interest in the analysis of pipe flow is the pressure drop Δp since it is directly related to the power requirements of the pump to maintain the flow.

For laminar flow:

$$\Delta p = p_1 - p_2 = \frac{8\mu L u_m}{r^2} = \frac{32\mu L u_m}{D^2} \quad \text{.........} \quad (3.36)$$

The pressure drop due to the viscous effects represents an irreversible pressure loss, and it is called pressure loss Δp_L and it is given by

$$\Delta p_L = f \frac{L}{D} \frac{\rho u_m^2}{2} \quad \text{.........} \quad (3.37)$$

Where, $\frac{\rho u_m^2}{2}$ is the dynamic pressure and f is the Darcy friction factor

The friction factor for fully developed laminar flow in circular pipe is (Incropera & DeWitt, 2007)

$$f = \frac{64}{Re} \quad \text{.........} \quad (3.38)$$

This equation shows that in laminar flow, the friction factor is a function of the Reynolds number only and is independent of the roughness of the pipe surface. Friction factor for a wide range of Reynolds number are presented in the moody diagram (Appendix (Fig.74)).

Head loss

The head loss h_L represents the additional height that the fluid needs to be raised by a pump in order to overcome the frictional losses in the pipe (Incropera & DeWitt, 2007).

$$h_L = \frac{\Delta p_L}{\rho g} = f \frac{L}{D} \frac{u_m^2}{2g} \quad \text{.........} \quad (3.33)$$

Once the pressure loss (or head loss) is known, the required pumping power to overcome the pressure loss is determined from

$$\dot{w}_{pump} = \dot{m} g h_L \quad \text{.........} \quad (3.34)$$

The average velocity for laminar flow from The Hagen–Poiseuille Flow equation (3.35) is

Horizontal pipe:

$$u_m = \frac{\Delta p D^2}{32\mu L} \quad \text{.........} \quad (3.35)$$

Inclined pipe:

$$u_m = \frac{(\Delta p - \rho g L sin\beta) D^2}{32\mu L} \quad \text{......} (3.36)$$

Whereas, the volume flow rate for laminar flow in pipe of length L and diameter D is given by;

Horizontal pipe:

$$\dot{V} = \frac{\Delta p \pi D^4}{128\mu L} \quad \text{......} (3.37)$$

Inclined pipe:

$$\dot{V} = \frac{(\Delta p - \rho g L sin\beta)\pi D^4}{128\mu L} \quad \text{......} (3.38)$$

3.12 Thermal consideration

The fluid enters the absorber tube at the temperature below the surface temperature, so that the convection heat transfer occurs and the thermal boundary layer begins to develop. Since the absorber tube is imposed to constant heat flux, a thermal fully developed condition is eventually reached. For laminar flow the entry length may be expressed as

$$\frac{x_{fd}}{D} = 0.05 Re_D pr \quad \text{......} (3.39)$$

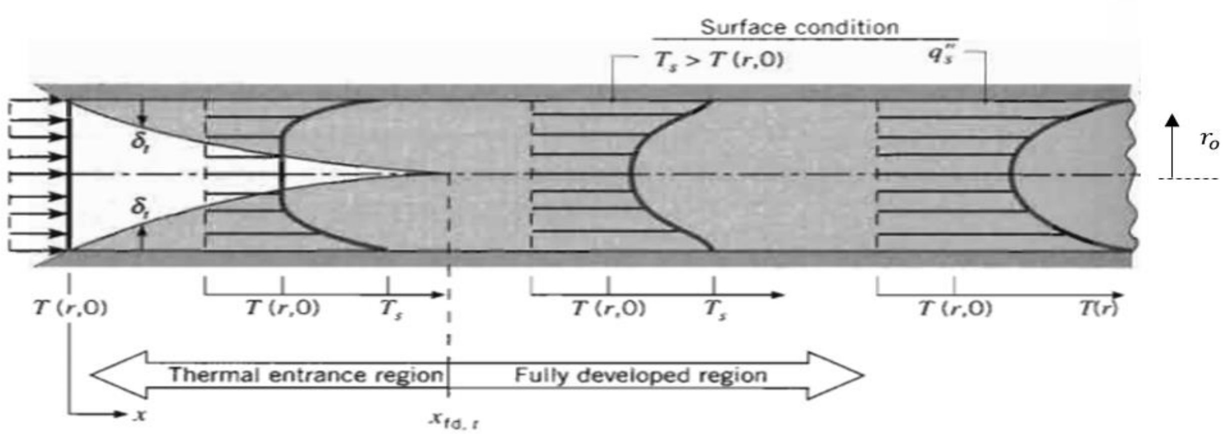

Figure 3.16 The thermal boundary layer development in a heated absorber tube (Incropera & DeWitt, 2007).

3.12.1 Mean temperature

The absence of a fixed free stream temperature necessitates using mean temperature.

From thermal energy of incompressible fluid

$$Q = \dot{m}c_p(T_{out} - T_{in}) \qquad (3.40)$$

The local heat flux at the surface is obtained by applying Fourier's law to the fluid at r = R

$$q_s'' = -k_{nf}\left(\frac{\partial T}{\partial r}|_{r=R}\right)_{sf} \qquad (3.41)$$

Near the wall of the tube absorber the surface heat flux is equal to the convective flux the fluid (no slip condition), which is expressed by the newton's law of cooling.

$$q_s'' = q_{conv}'' = h_{nf,x}\left(T_{w,x} - T_{m,x}\right) \qquad (3.42)$$

The true advection rate may be obtained by integrating the product of mass flux and enthalpy per unit mass over the cross section.

Therefore,

$$\dot{m}c_p T_m = \int_{A_c} \rho u c_p \, T dA_c \qquad (3.43)$$

For flow in circular tube, It follows from above equation that;

$$T_m = \frac{2}{u_m R^2}\int_0^R uTrdr \qquad (3.44)$$

From equation (3.41) and (3.42) the local convection coefficient of nanofluid are given by;

$$h_{nf,x} = -\frac{k_{nf}}{(T_{w,x} - T_{m,x})}\left(\frac{\partial T}{\partial r}|_{r=R}\right)_{nf} \qquad (3.45)$$

And the Nusselt number of nanofluid are given by;

$$Nu_{nf} = \frac{h_{nf,x}}{k_f}D \qquad (3.46)$$

Substituting for $h_{nf,x}$

$$Nu_{nf} = -\frac{2k_{nf}}{k_f}\frac{R}{T_{w,x}-T_{m,x}}\left(\frac{\partial T}{\partial r}|_{r=R}\right)_{nf} \quad \text{……………………………………………………… (3.47)}$$

The rate of the heat transfer improvement in heat transfer coefficient is calculated as follows

$$Nu(\%) = \frac{Nu_{nf}-Nu_w}{Nu_w} \quad \text{……………………………………………………………………… (3.48)}$$

Constant surface heat flux

For constant heat flux the total heat transfer rate is,

$$q_{conv} = q_s''(p.L) \quad \text{……………………………………………………………………… (3.49)}$$

Where p is perimeter $p = \pi D$ and L is the length of the tube.

Since $q_s''q$ is independent of x, and

$$\dot{m}c_p\frac{dT_m}{dx} = q_s''p \quad \text{……………………………………………………………………….. (3.50)}$$

Integrating from x=0, equation becomes,

$$T_m(x) = T_{mi} + \frac{q_s''p}{\dot{m}c_p}x \quad \text{…………………………………………………......…………..… (3.51)}$$

The mean temperature along the tube length x varies linearly.

3.13 Analysis nanofluids thermal properties

The transport properties of nanofluid (dynamic thermal conductivity and viscosity) are not only dependent on volume fraction of nanoparticle, also highly dependent on other parameters such as particle shape, size, mixture combinations and slip mechanisms, surfactant, etc.

3.13.1 Thermal conductivity

The effective thermal conductivity is given by the (Maxwell, 1881) model:

$$k_{eff} = \frac{k_p+2k_{bf}+2\vartheta(k_p-k_{bf})}{k_p+2k_{bf}-\vartheta(k_p-k_{bf})}k_{bf} \quad \text{…………………………………………..…..……… (3.52)}$$

Where k_p the thermal conductivity of the particles, k_{eff} is the effective thermal conductivity of nanofluid, k_{bf} is the base fluid thermal conductivity, and ϑ is the volume fraction of the suspended particles.

3.13.2 Viscosity

The effective viscosity of a suspension of spherical solids as a function of volume fraction (volume concentration lower than 5%) determined using the phenomenological hydrodynamic equation (Einstein, 1999).

The effective viscosity was expressed by:

$$\mu_{eff} = (1 + 2.5\vartheta)\mu_{bf} \quad \text{(3.53)}$$

3.13.3 Specific heat and density

Using classical formulas derived for a two-phase mixture, the specific heat capacity (Pak and Cho, 1998) and density (Xuan and Roetzel, 2000) of the nanofluid as a function of the particle volume concentration and individual properties can be computed using following equations (Eq. 3.54) and (Eq. 3.55) respectively:

$$\rho_{eff} = (1 - \vartheta)\rho_{bf} + \vartheta\rho_p \quad \text{(3.54)}$$

$$(\rho c_p)_{eff} = (1 - \vartheta)(\rho c_p)_{bf} + \vartheta(\rho c_p)_p \quad \text{(3.55)}$$

3.14 Efficiency of solar flat plate colletor

Thermal efficiency of SFPC is given by expression below

$$\eta = \frac{Q_u}{IAc} \quad \text{(3.56)}$$

Where,

$$Q_u = \dot{m}c_p(T_O - T_i) \quad \text{(3.57)}$$

3.15 Basic steps in ANSYS FLUENT

In order to provide easy access to their solving power all-commercial CFD packages include sophisticated user interfaces to input problem parameters to examine the results. Hence, all code contains three main elements:

1. Pre-processor

2. Solver

3. Post-processor

3.15.1 Geometry

The 3D geometry has done on Ansys design modeler as shown Fig.3.12. The geometry consists of an absorber plate and tube part and fluid part at center of plate. 3D model is created was used for meshing in next steps.

3.15.2 Meshing

The unstructured grid is been created using ANSYS ICEM CFD software as shown in Fig.3.17 and Fig.3.18. To solve the previous governing equations the 3D model is meshed with finite control volume method as used by several authors.

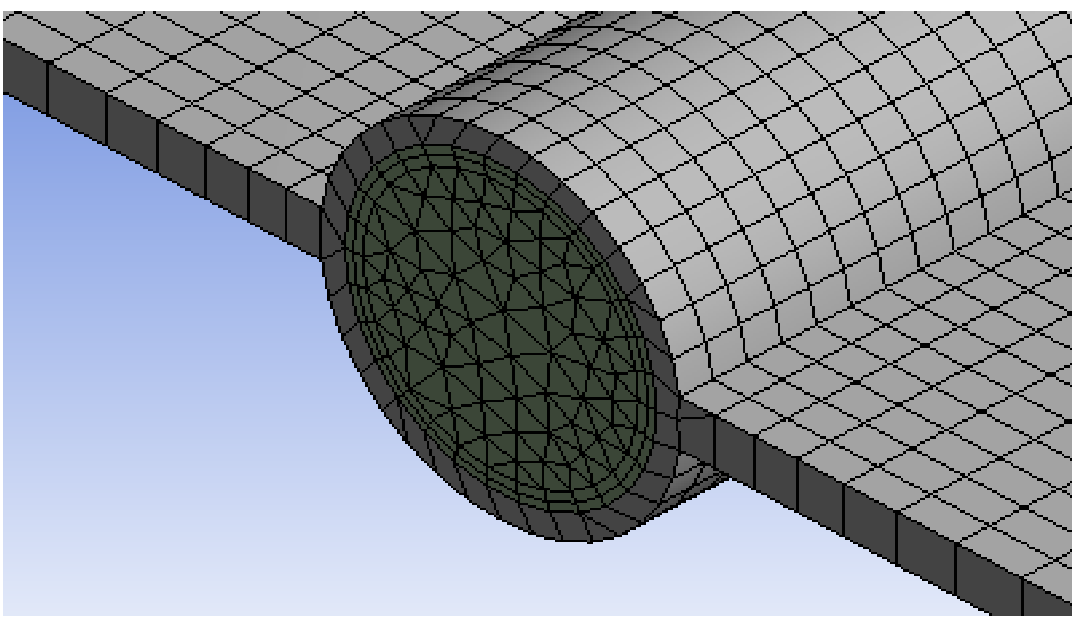

Figure 3.17 Mesh detail of the computational domain

The complete domain consists of 343956 elements, which include fluid, absorber plate and tube medium with better quality.

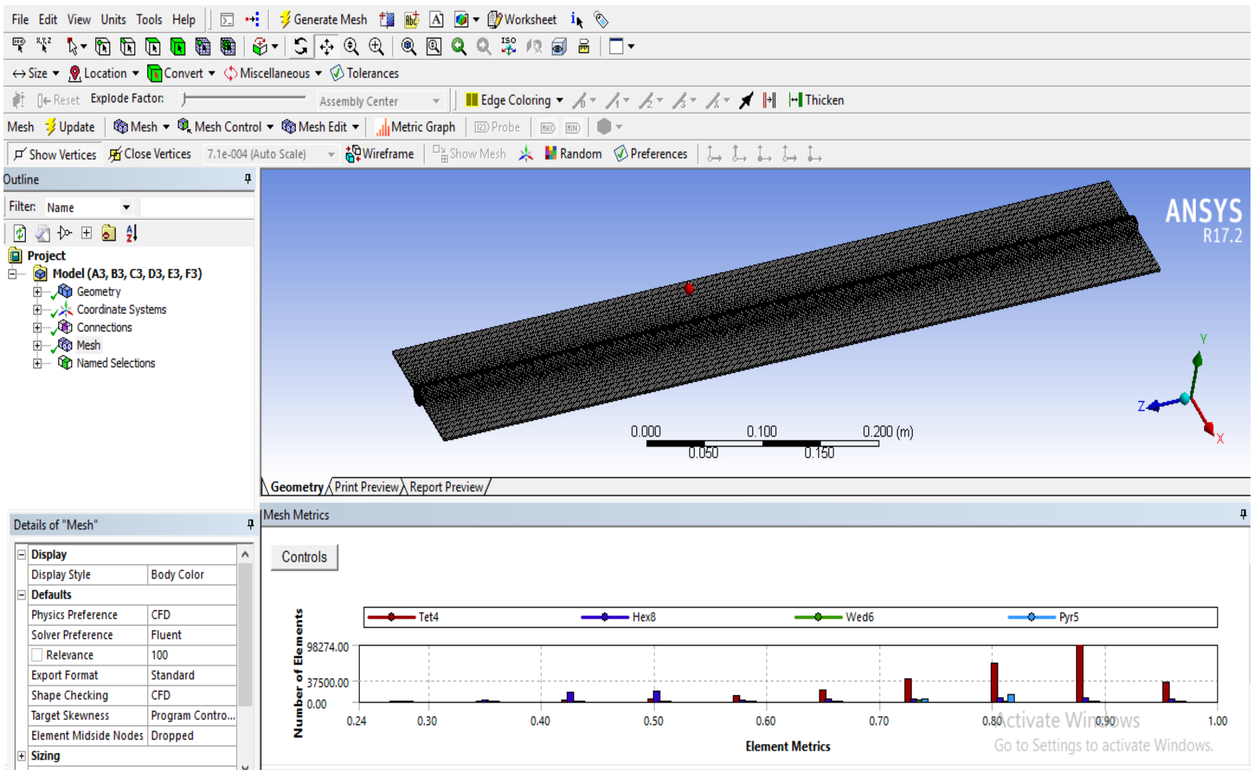

Figure 3.18 Mesh of the computational domain

3.15.3 Set up

The numerical simulation is carried out with steady state implicit pressure based solver using the fluent 7.2 code. The governing equations are solved for steady state flows and the pressure velocity coupling is done using the SIMPLE algorithm. Discretization is made using second order upwind scheme and the simulation is carried out for the laminar flow. The convergence was affected when the energy residuals fell below 1.0 e^{-6} in the domain.

Boundary conditions

Appropriate boundary conditions were impressed on the computational domain, as per the physics of problem. For the inlet, a ‘velocity inlet’ boundary condition is specified and ‘outflow’ condition is specified at outlet for fluids (i.e. water and nanofluids). Top surface of the absorber is exposed to heat flux (radiation) considering glass transmittance while the wall and bottom surfaces are subjected to convection.

Heat transfer coefficient of 11.8 W/m^{2}K and temperature of 297.096 K at 1:00 pm. In viscous models at the wall, the velocity is set to zero in accordance with the no-slip conditions. Flow chart used for comparison of temperature for various velocity in Ansys fluent workbench is given as shown below.

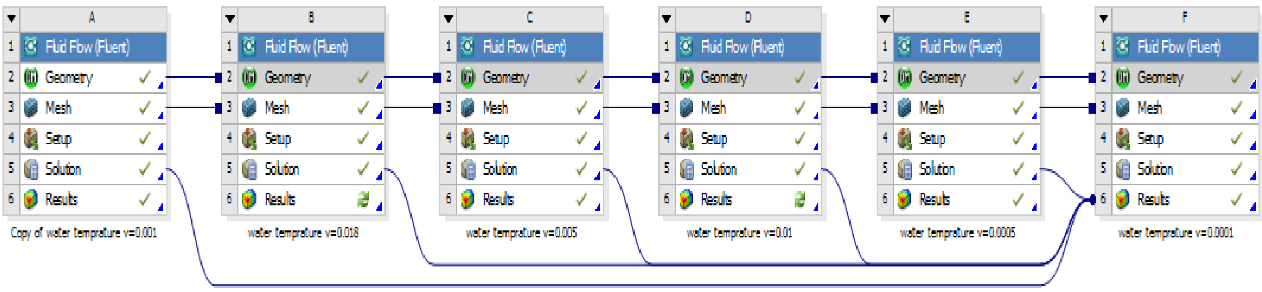

Figure 3.19 Flow chart network for comparison

3.15.4 Solution

The solution is generated by setting the initial value of temperature 300 K and velocity 0.0005 m/s for the solution to converge. The solution converge after 74 iteration.

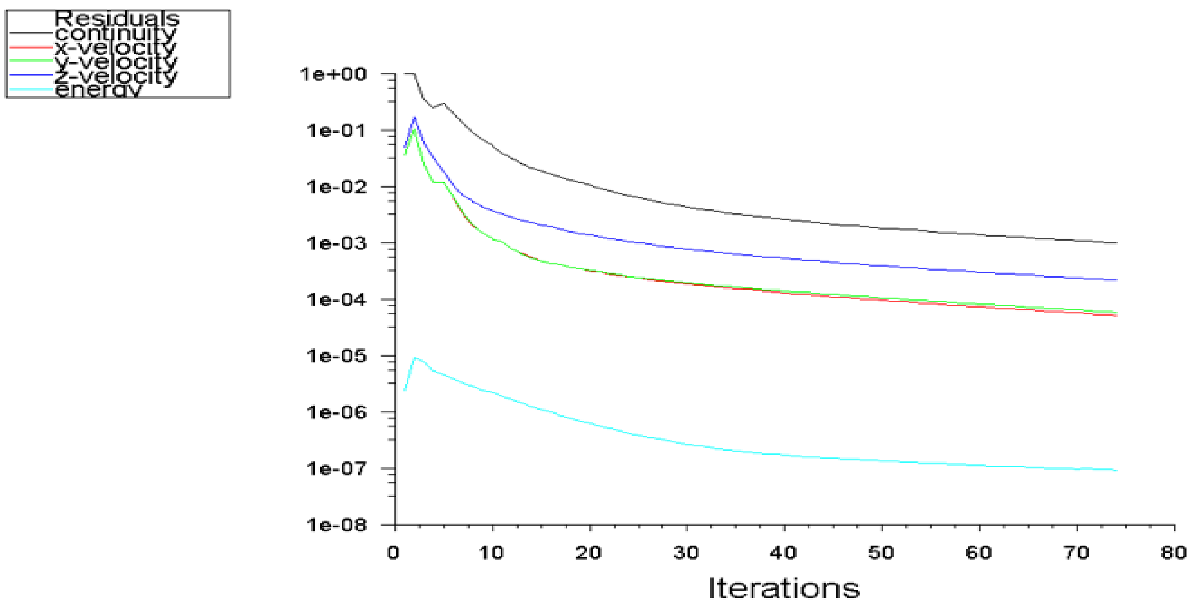

Figure 3.20 Scaled residuals for CFD simulation of SFPC at velocity of V = 0.01 m/s and I_t = 803.17 W/m^2 at 1:00 pm.

CHAPTER FOUR

RESULTS and DISCUSSIONS

4.1.0 Solar radiation estimation

For solar radiation estimation, the data gathered are analyzed and evaluated by using the MS Excel program. In this study, the data for the last five consecutive years are taken for analysis. Since there is no enough global radiation data for all year, the sunshine hour is collected and global, diffuse and beam solar radiation on the horizontal and tilted surface is calculated.

Sunshine duration or **sunshine hours** is a climatological indicator, measuring the duration of sunshine in a given period (usually, a day or a year) for a given location on earth, typically expressed as an averaged value over several years. It is a general indicator of cloudiness of a location and thus differs from insolation, which measures the total energy delivered by sunlight over a given period.

Table 4.1 Sunshine hour duration of Adama City.

Years	Months											
	Jan	Feb	Mar	Apr	May	Jun	July	Aug	Sep	Oct	Nov	Dec
2014	10.2	10.3	6	8.2	7.5	7.2	9.5	9.9	8.6	10.9	9.6	10.5
2015	10.4	9.3	10.6	9.8	8.3	5.8	8.6	9.2	8.5	8.7	10.1	8.6
2016	6.8	9.7	10.1	6	7	7	10.4	11.3	9	10.6	10.4	10.5
2017	10.5	8.7	10.7	11.4	10.7	9.1	8.7	10.5	8.4	8.4	10.2	6.9
2018	10.5	9.5	9.1	8.3	6.2	7.4	6.7	6.6	8.3	9.1	9.4	10.9

Sunshine duration is usually expressed in hours per year, or in (average) hours per day. The first measure indicates the general sunniness of a location compared with other places, while the latter allows for comparison of sunshine in various seasons in the same location.

Another often-used measure is the percentage ratio of recorded bright sunshine duration and daylight duration in the observed period. Table 8 shows the sunshine hour duration for last five consecutive years from nearby meteorology agency and Fig.4.1 shows the variation of sunshine hour for different years for Adama, Ethiopia. The average sunshine hour is minimum in summer season and maximum in winter season.

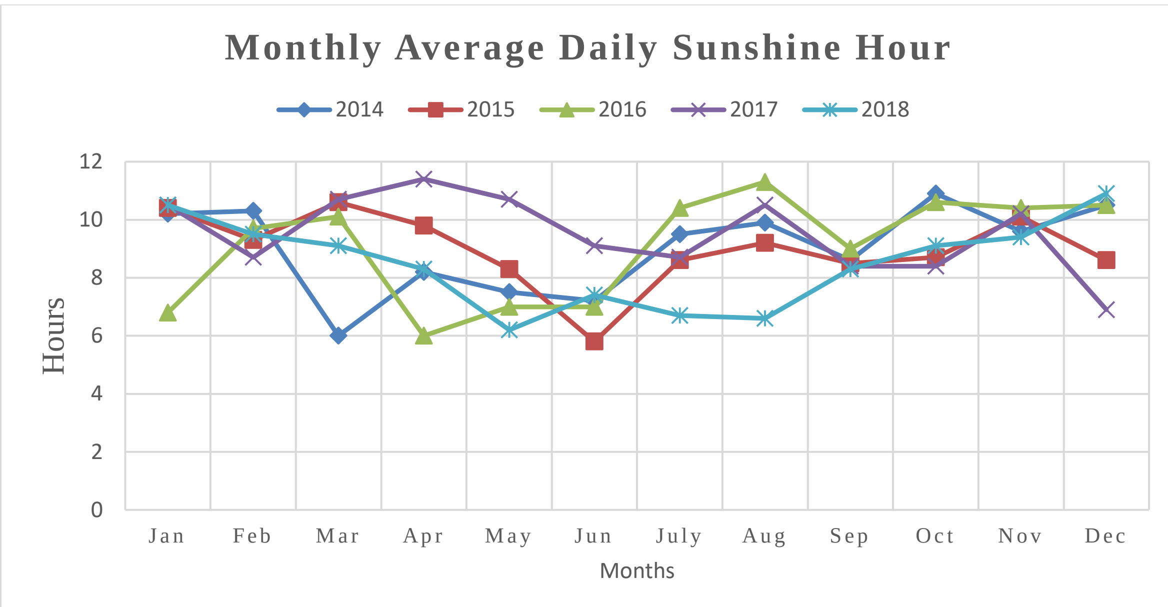

Figure 4.1 Shows the sunshine hour duration for Adama City for last five years.

The sunshine hours was maximum in winter season and minimum in summer season for all years as shown in Fig.4.1. Therefore, the minimum solar radiation in summer season is expected.

4.1.1 Solar radiation on horizontal surface

Global radiation is the total irradiance from the sun on a horizontal surface on Earth. It is the sum of direct irradiance (after accounting for the solar zenith angle of the sun *z*) and diffuse horizontal irradiance. This is calculated in MS excel using sunshine hour data for each year and the average global solar radiation (GSR) for year 2018 is shown in Fig.4.2.

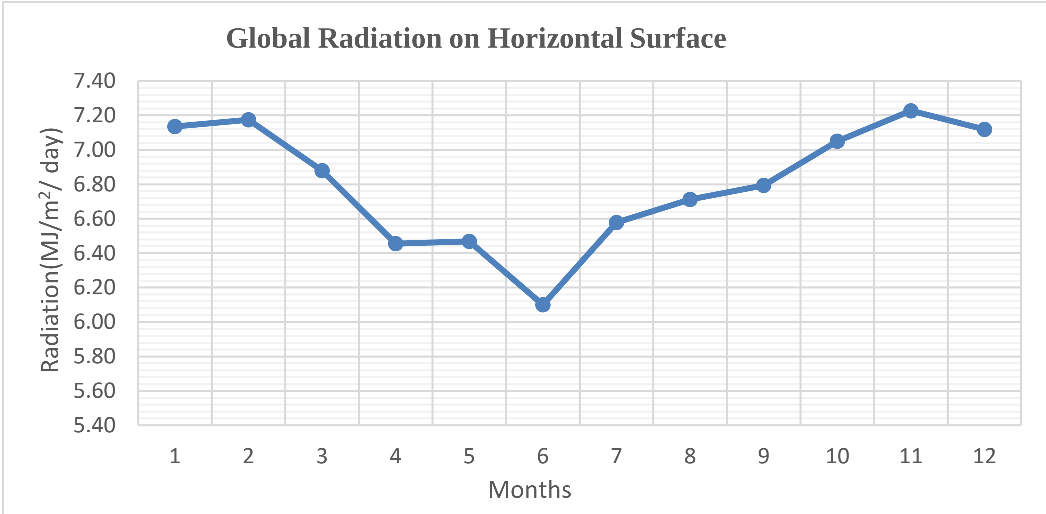

Figure 4.2 The global solar radiation on horizontal surface for 2018.

From Fig.4.2 the average global solar radiation on horizontal surface was minimum in June and maximum in November. The average annual daily global radiation was calculated from the daily global radiation for each year and shown in the Figure 4.3.

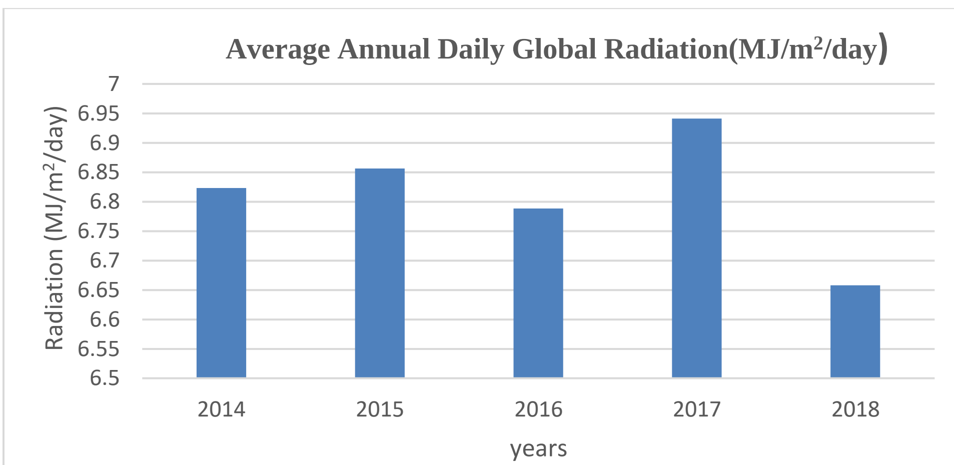

Figure 4.3 Annual global solar radiation for five years (2014-2018).

The maximum average annual daily global radiation was in 2017 which is 6.94 MJ/m^2/day and the minimum the maximum average annual daily global radiation was in 2018 which is 6.65 MJ/m^2/day. The year 2018 solar radiation was used thought the study due- to its nearest future and lower among all. The values of solar radiation on horizontal surfaces are listed in Appendix (Table A1).

4.1.2 Comparison of measured and estimated global solar radiation on horizontal surface

The comparison was carried out only for the year 2018 since there is no measured data for the other years. The calculated GSR was based on the representative day of months. While the measured global radiation on the horizontal surface was measured at, NMAE & CMSC station using a pyrometer.

The result shows the maximum measured global solar radiation is 204.74 W/m^2 and happen in February where as the minimum GSR is 157.53 W/m^2 in November. In case of calculated GSR the maximum and minimum GSR is 123.57 in August and 182 W/m^2 in December respectively. The range of values related to measured GSR was 178.47 ± 4.26 W/m^2 and that of calculated was 154.28± 7.72 W/m^2. The validation of calculated result and measured result interms of uncertainity error in percentage was 2.13% and 7.17% respectively.

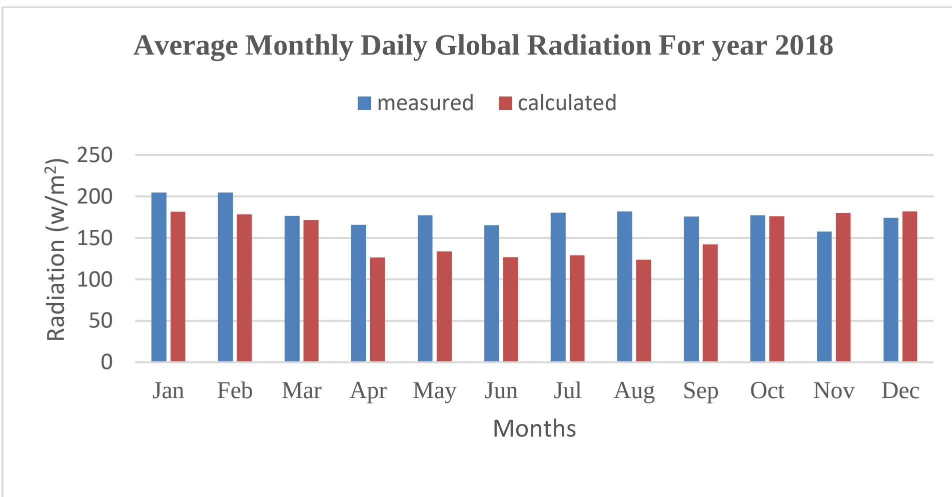

Figure 4.4 Comparison of measured and estimated global solar radiation in W/m^2.

4.1.3 Global and diffuse solar radiation on horizontal surface

Diffuse sky radiation is solar radiation reaching the Earth's surface after having been scattered from the direct solar beam by molecules or particulates in the atmosphere. The diffuse solar radiation was achieved for Adama city in the year 2018 and its graph follow the same shape as that of GSR.

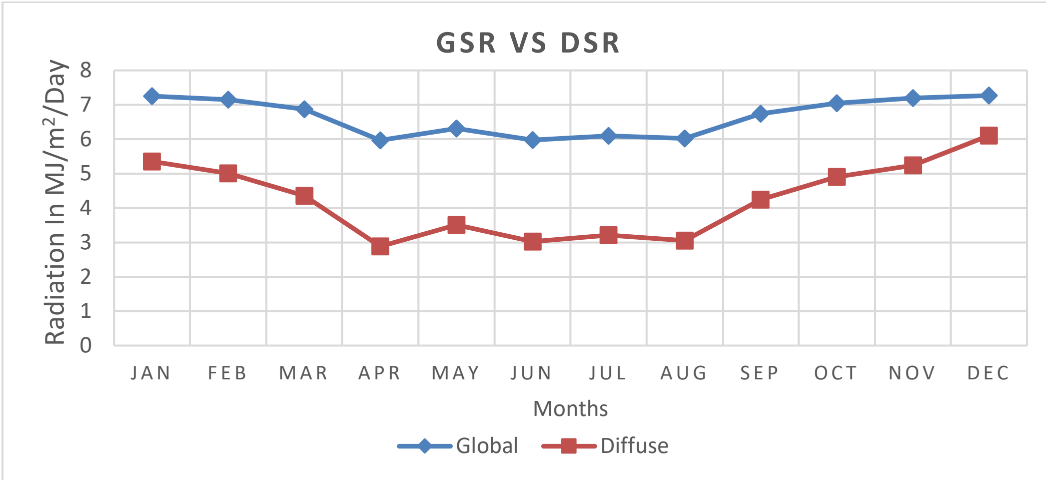

Figure 4.5 Global solar radiation and diffuse solar radiation

4.1.4 Monthly average hourly global radiation on horizontal surface

The monthly average daily global radiation on horizontal surface was given in Fig.4.6. the monthly average daily global radiation on horizontal surface was based on representative day of the given month.

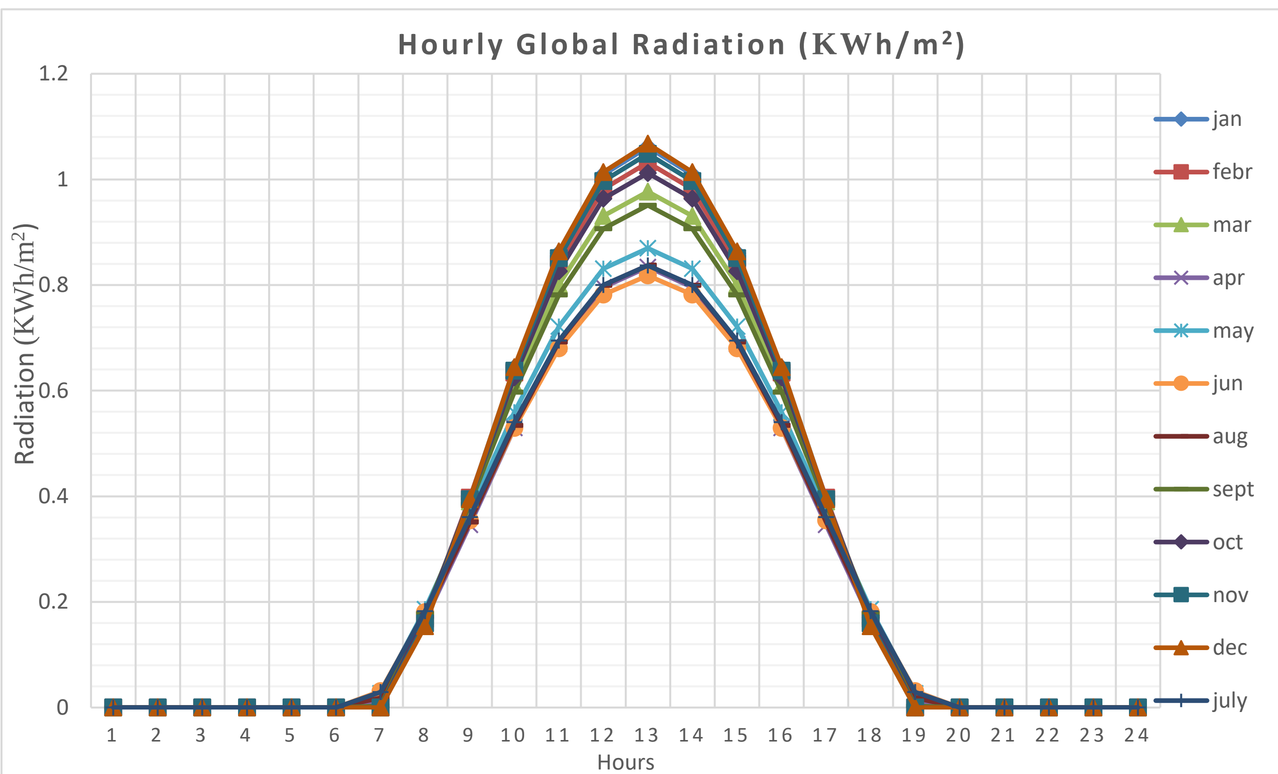

Figure 4.6 Average hourly global radiation on horizontal surfaces

There was high solar radiation in October, December and November whereas low solar radiation in May, June and July as shown in Fig. 4.6. The monthly average hourly global radiation on tilted surface was shown in Fig.4.7.

4.1.4 Solar radiation on tilted surface

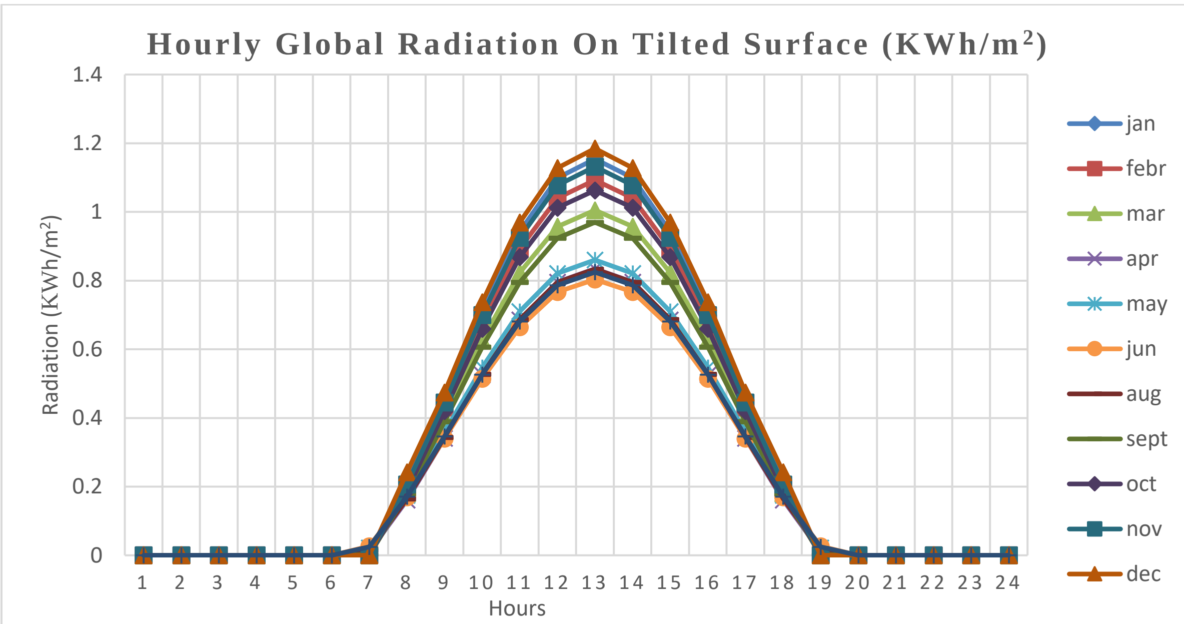

Figure 4.7 The average hourly global radiation on tilted surface for year 2018.

Fig.4.7 shows the monthly average hourly global radiation on tilted surface was maximum in December and minimum in June. The hourly global radiation on tilted surface is calculated from global and diffuse radiation on horizontal surface considering the ground reflectance for dry bare land and assuming same for all months (0.2).

4.2 The thermodynamics performance of flat-plate solar thermal collector using different nanofluid.

4.2.1 Density of nanofluids

Before the investigation of nanofluid SFPC performance carried out analytical analyses have been done on four types of metal oxides nanofluids namely: SiO_2, TiO_2, Al_2O_3, and CuO to made basis in theoretical comparison with the experimental investigation in literature. Density is an important thermo-physical property of working fluid and must be considered.

As shown in the Fig.4.8 the theoretical density of nanofluids is calculated from equation (3.54) and greater than that of water in all cases. The density rises linearly as volume concentration increases. Additionally, the density of CuO is higher than the other nanofluids as shown in the Fig.4.8.

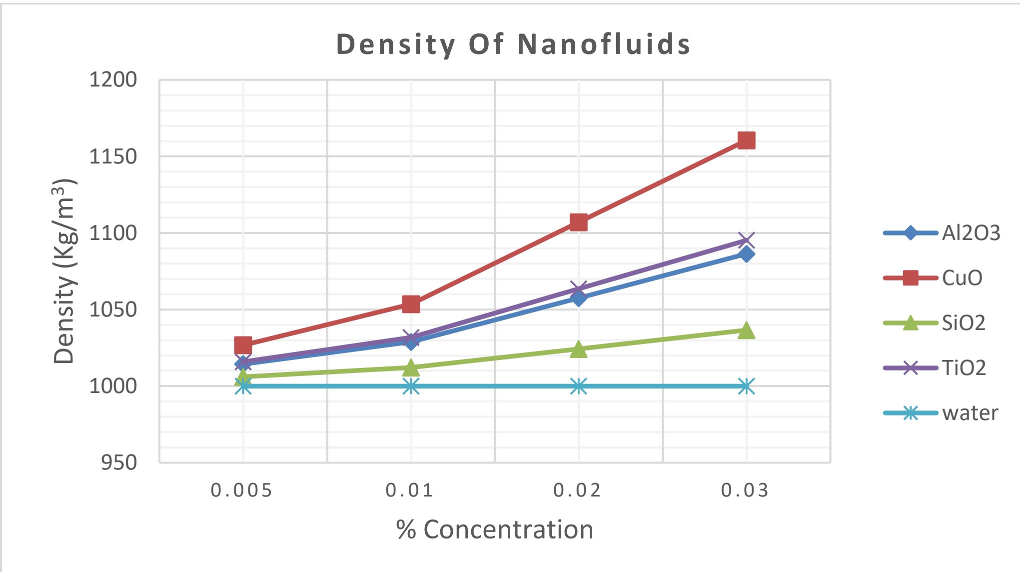

Figure 4.8 Density of nanofluids

The analytical result achieved was almost similar to the experimental result found by (Madhu & Rajasekhar, 2017).

4.2.2 Specific heat

The specific heat of nanofluids is necessary to evaluate the performance of SFPC using nanofluids. It is the amount of energy that must be added, in the form of heat, to one unit of mass of the substance in order to cause an increase of one unit in its temperature. The specific heat of nanofluids are inversely proportional to the volume concentration of nanoparticles as shown in Fig.4.9 and this result is related to that of (Madhu & Rajasekhar, 2017) . According to the literature CuO nanofluids has least specific heat and water has highest specific heats. Liquid water has one of the highest specific heats among common substances, about 4182 J/K/kg at 20°C. The smaller specific heats directing to smaller amount of energy needed to raise temperature of nanofluids.

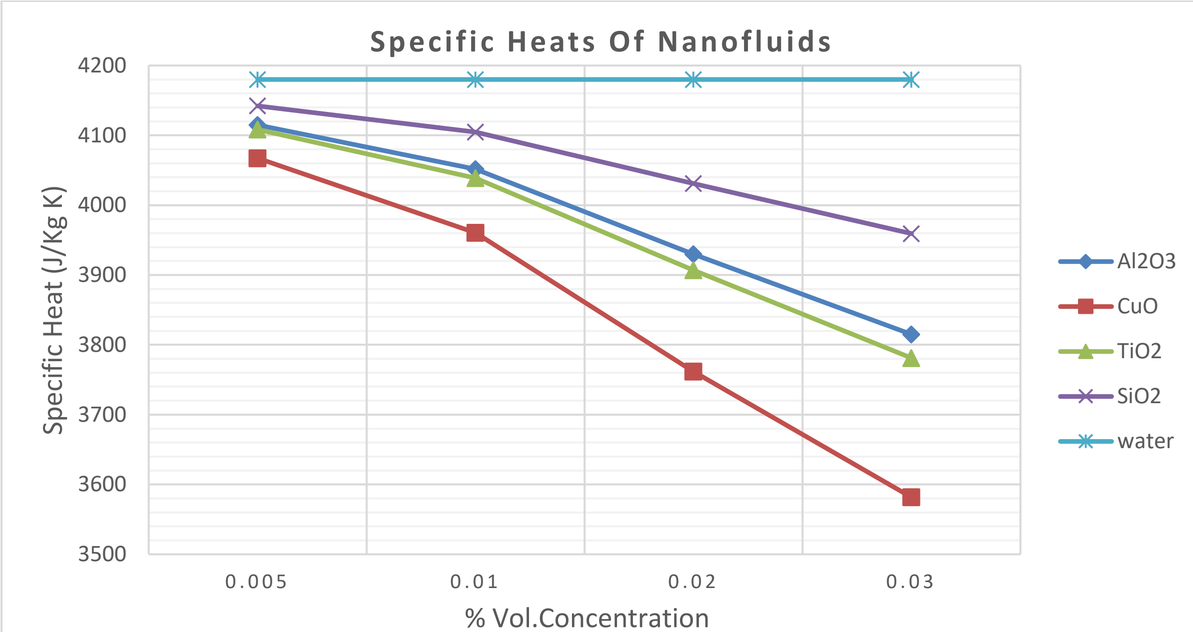

Figure 4.9 The effects of different volume concentration of nanoparticles on specific heats.

4.2.3 Thermal conductivity

The thermal conductivity of nanofluids are calculated by using Maxwell Equation (3.54) which can be applied to the homogeneous and low volume fraction liquid-solid suspensions. It was found that by using the theoretical model the thermal conductivity of nanofluids highly increases with rise in volume fraction as shown in Fig.4.10. The result achieved was similar to the experiment result found by (Mariappan, 2012) .

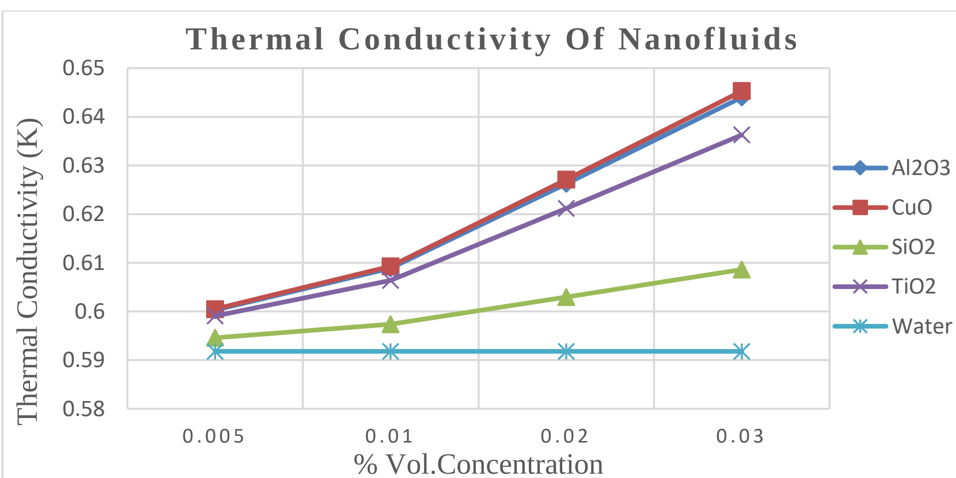

Figure 4.10 Effect of concentration on the thermal conductivity.

4.3 The x-ray diffractometer (XRD) result

The instrument used is Shimadzu XRD -700 X-ray diffractometer . The XRD results shows that the high and sharp intensity of alpha and gamma phase Al_2O_3 as shown in Fig.4.11. This reflects the α-phase Al_2O_3 dominates the γ-phase Al_2O_3. This XRD result is almost similar with that of (Rajaeiyan, 2013) in which the particles sizes found to be 27-32 nm as stated in literature.

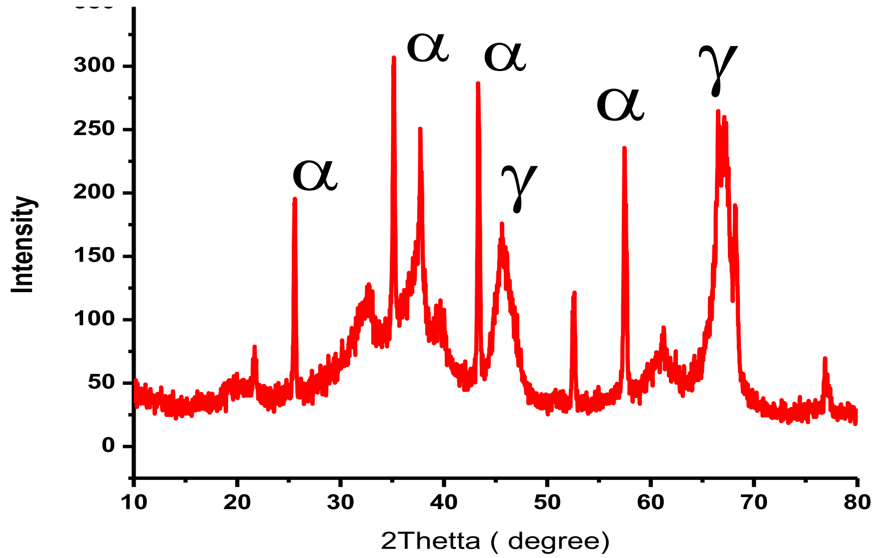

Figure 4.11 XRD results of Al_2O_3 calcined at 1000℃.

4.4 The computational fluid flow (CFD) results

4.4.1 The temperature contours at different inlet velocity

The analysis is carried out for different time conditions i.e. 9am,10am,11am,12noon and 1pm of the day and six different velocity $V_1 = 0.0001$ m/s, $V_2 = 0.0005$ m/s, $V_3 = 0.001$ m/s, $V_4 = 0.005$ m/s, $V_5 = 0.01$ m/s, $V_6 = 0.018$ m/s.

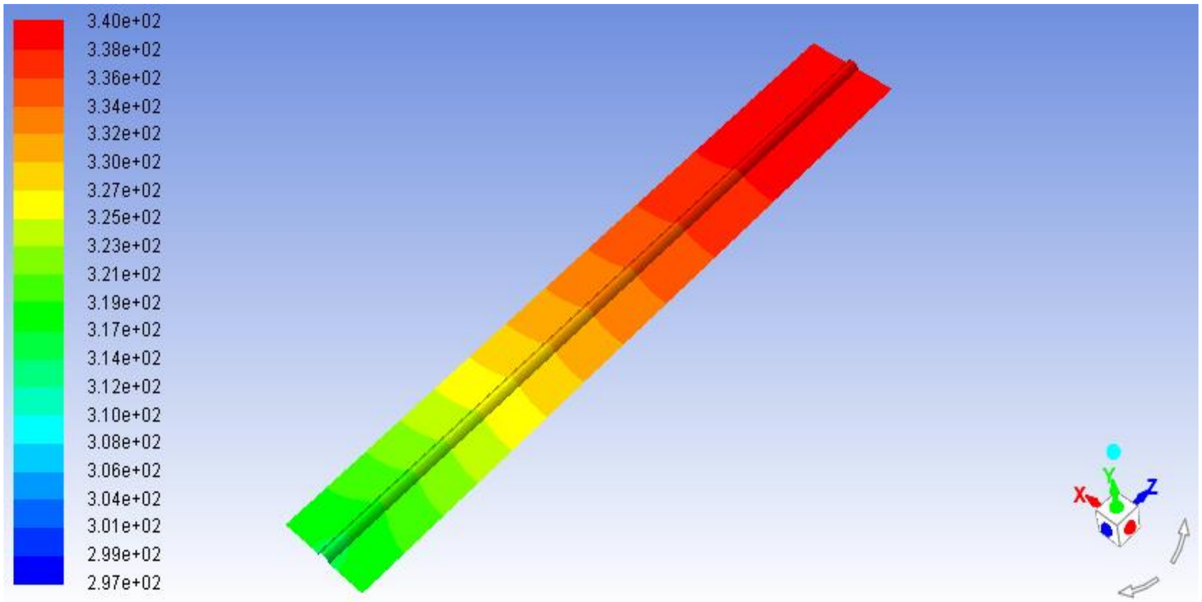
3.40e+02
3.38e+02
3.36e+02
3.34e+02
3.32e+02
3.30e+02
3.27e+02
3.25e+02
3.23e+02
3.21e+02
3.19e+02
3.17e+02
3.14e+02
3.12e+02
3.10e+02
3.08e+02
3.06e+02
3.04e+02
3.01e+02
2.99e+02
2.97e+02
X
Y
Z
(a)

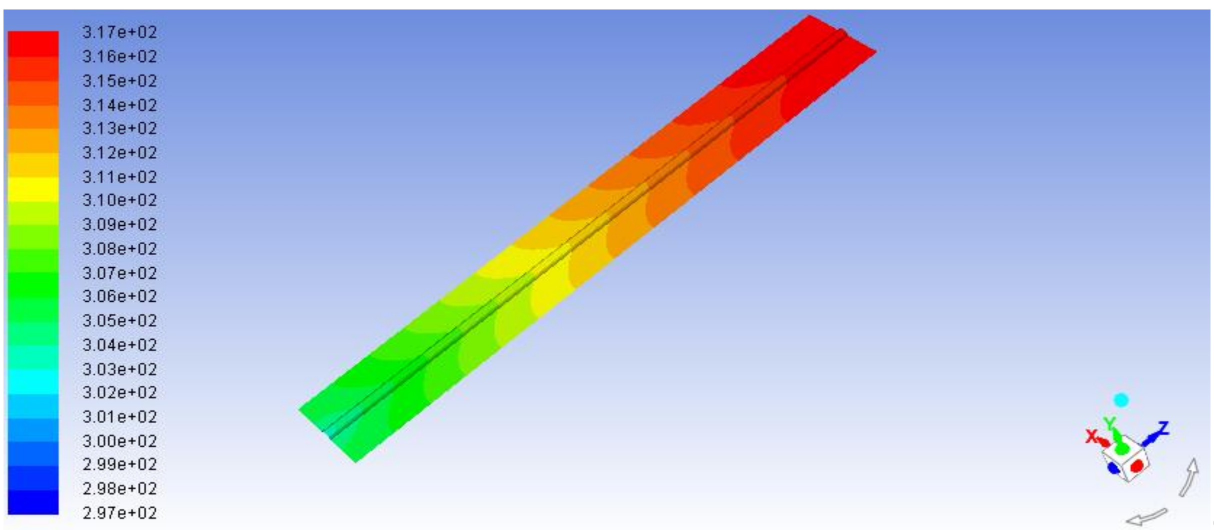
3.17e+02
3.16e+02
3.15e+02
3.14e+02
3.13e+02
3.12e+02
3.11e+02
3.10e+02
3.09e+02
3.08e+02
3.07e+02
3.06e+02
3.05e+02
3.04e+02
3.03e+02
3.02e+02
3.01e+02
3.00e+02
2.99e+02
2.98e+02
2.97e+02
X
Y
Z
(b)

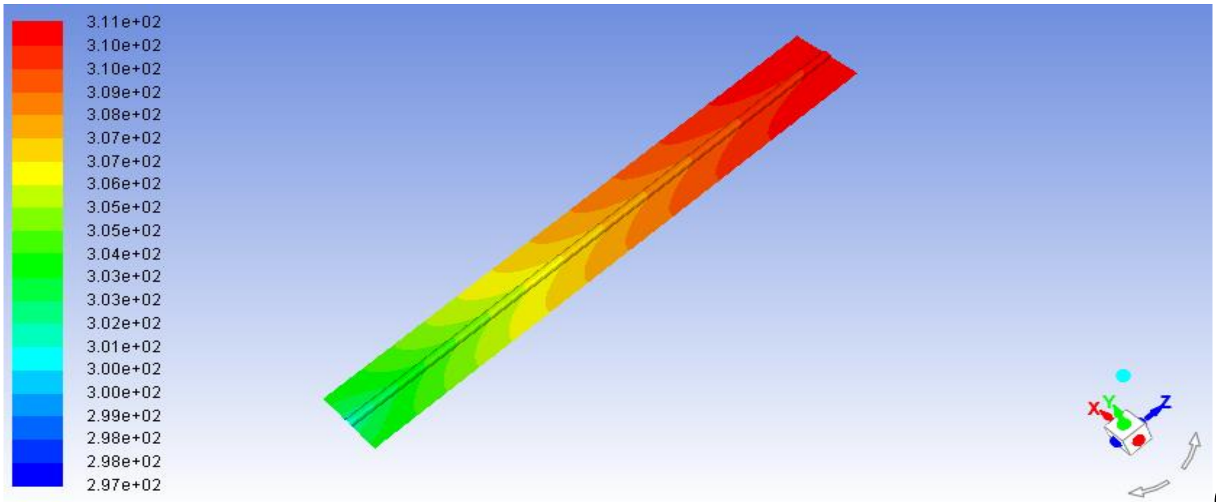

(c)

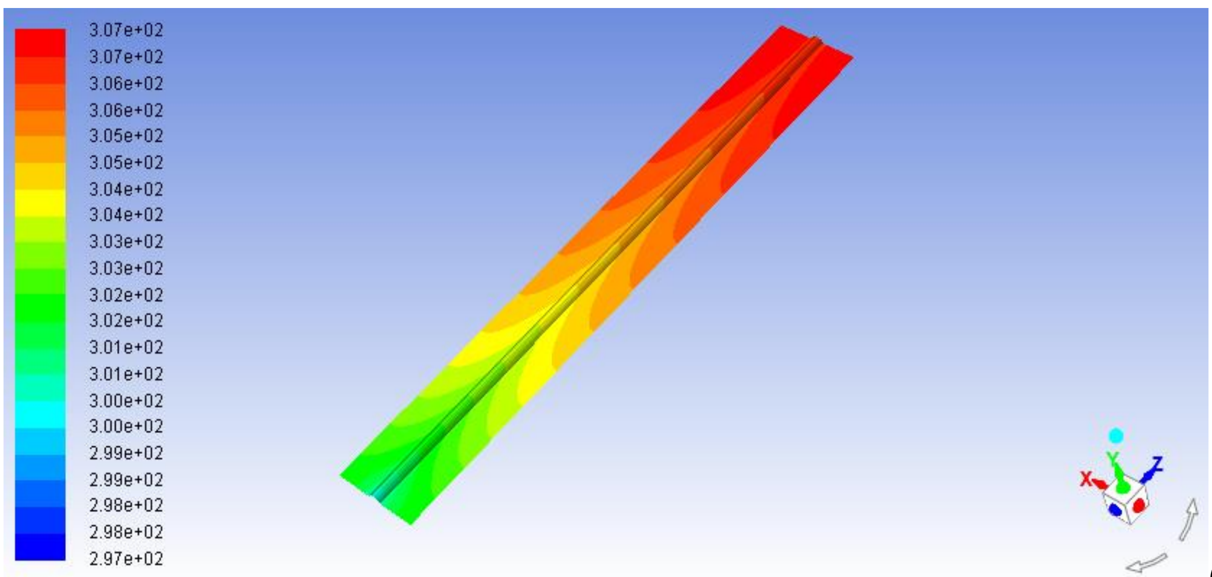

(d)

Figure 4.12 Water Temperature distribution on absorber plate for (a) V_1 = 0.001 m/s, (b) V_2 = 0.005 m/s, (c) V_5 = 0.01 m/s and (d) V_6 = 0.018 m/s.

The water temperature distribution along absorber plate for various velocity are as shown in Fig.4.12 and the contours are matching the result obtained by (Karanth, Vasudeva, & Yagnesh, 2011) and (Maouassi, 2017) in the literature. However, the numerical results are slightly differ; which may be due the difference in geometrical dimension and parameters.

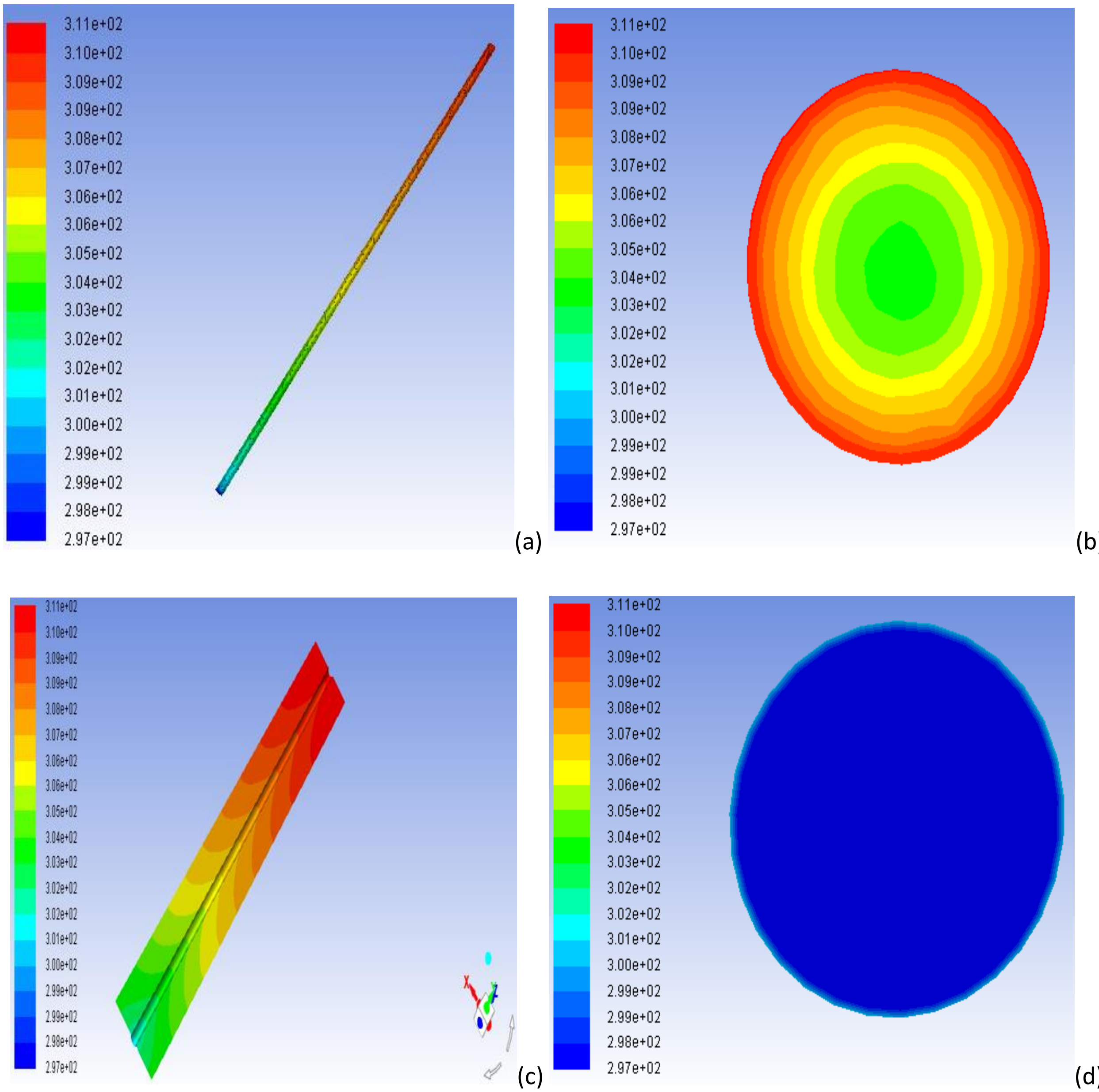

Figure 4.13 Temperature distribution for V = 0.01m/s and It = 803.17 W/m^2 a) water part, (b) outlet, (c) bottom surface of absorber plate and (d) inlet.

4.4.2 The absorber plate and water temperatures at different inlet velocity

The temperature distribution in the fluid and absorber plate are given in Fig.4.14 and Fig.4.15. The profile are similar to the results of some Authors i.e. Karanth et al., (2011), (Maouassi, 2017) and in the literature.

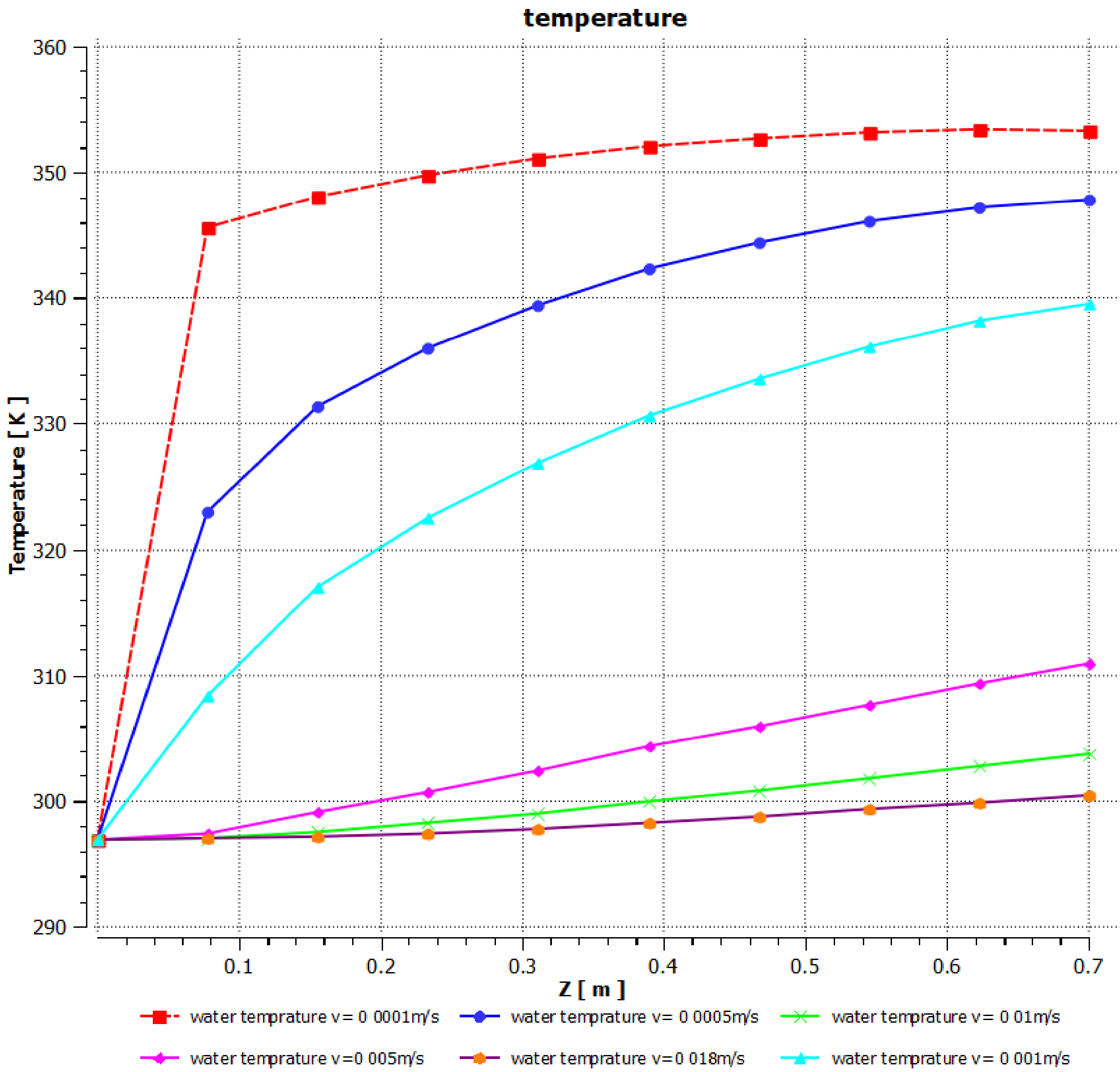

Figure 4.14 Water temperature at different inlet velocity and I_t = 803.17 W/m^2.

The results in Fig.4.14 Shows as the velocity inlet (mass flow rate) increases the temperature of the fluid decreases and the water temperature increases across flow length. However, the numerical value difference from literature may be due to the geometry difference and some changes in parameters.

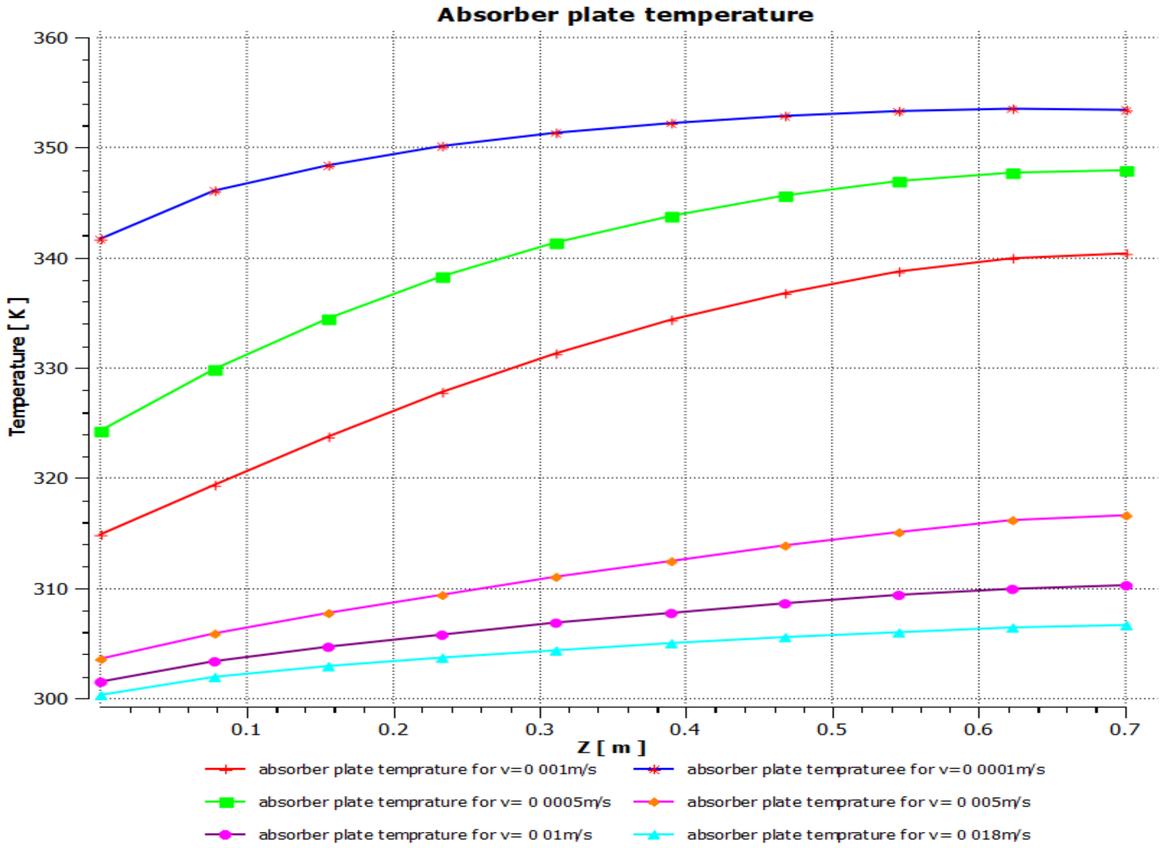

Figure 4.15 The absorber plate temperature across flow length corresponding to 1:00 pm and varying inlet velocity.

4.4.3 Comparison between absorber plate and water outlet temperature

Fig.4.16 shows the absorber plate temperature is greater than the water temperature. The line 10 and line 11 indicates the absorber plate and water temperature respectively.

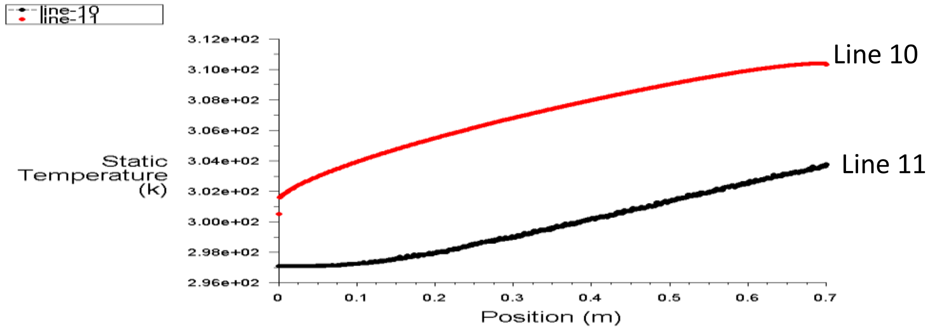

Figure 4.16 Comparison between absorber plate and water temperature.

4.4.4 Temperature distribution along the flow length

The distribution of water temperature for $\dot{m} = 0.003434 kg/s$ (single riser) with solar radiation is shown in Figure below. The result can be related to the literature (A.A., K., S., & S.A., 2016) nearly similar results keeping the collector area difference.

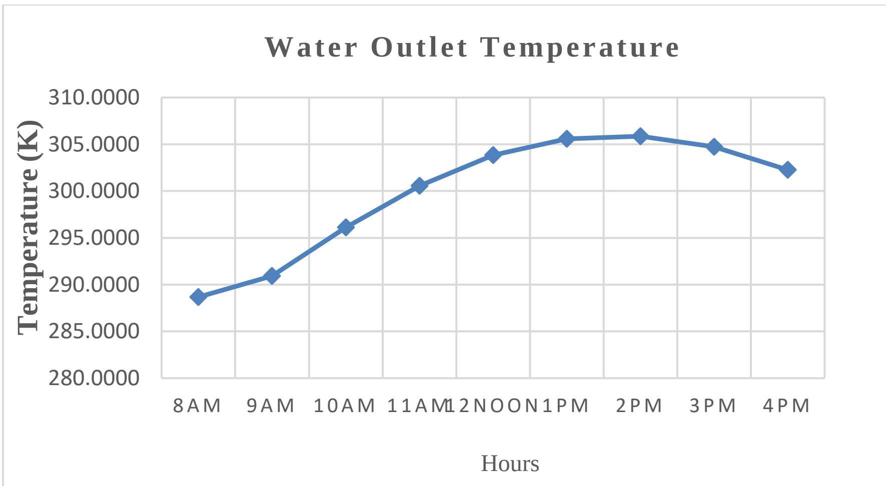

Figure 4.17 The water outlet temperature at $\dot{m}$ = 0.003434 kg/s for June 11, 2018.

Fig.4.17 showed the hourly temperature distribution of water for open loop SFPC system. The result showed that the conventional solar flat plate collector increases the water temperature by 19 ℃.

4.4.5 Comparison of different nanoparticles hourly solar flat plate colletor outlet temperature with that of solar flat plate colletor using water.

The hourly outlet temperature for different nanofliuds based solar flat plate collector are given in Fig.4.18 and compare with that of the water based solar flat plate collector. The gragh of hourly global solar radiation, inlet temperature and outlet temperature for 1% CuO, 1% Al_2O_3, and water are shown in Fig.4.18.

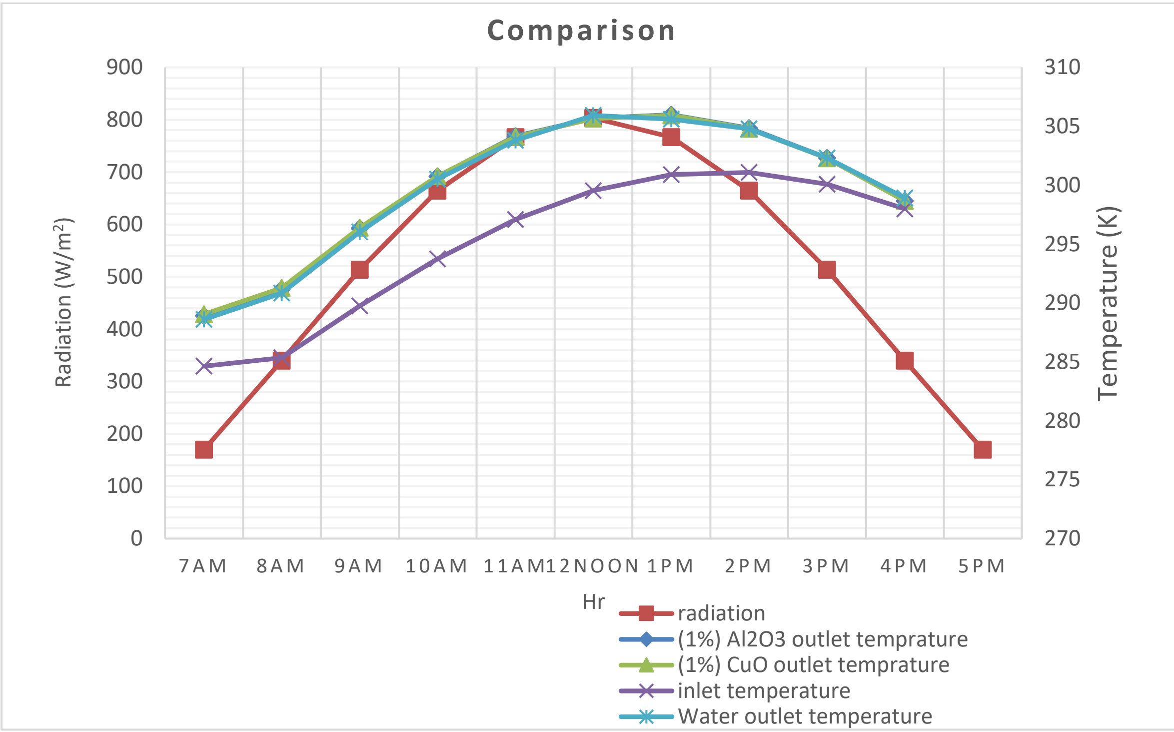

Figure 4.18 Comparison of outlet temperatures of alumina and copper oxide as working fluid with water.

The outle temperature in all cases are increased as shown in Fig.4.18. However, the result seems overlapped. This can be due to the open loop system and size of the collector as well. Additionally as shown in Fig.4.18 the solar radiation increased during morning and decreased during after noon. The solar radiation is maximum at noon time.

4.5 The average nusselt number for different nanoparticles and concentration.

Fig. 4.19 showed the average nusselt number versus Reynolds number for different Al_2O_3 concentration. Similarly for CuO, SiO_2, and TiO_2 the graph of nusselt number versus Reynolds number are given in Fig. 4.20, 4.21 and 4.22 respectively.

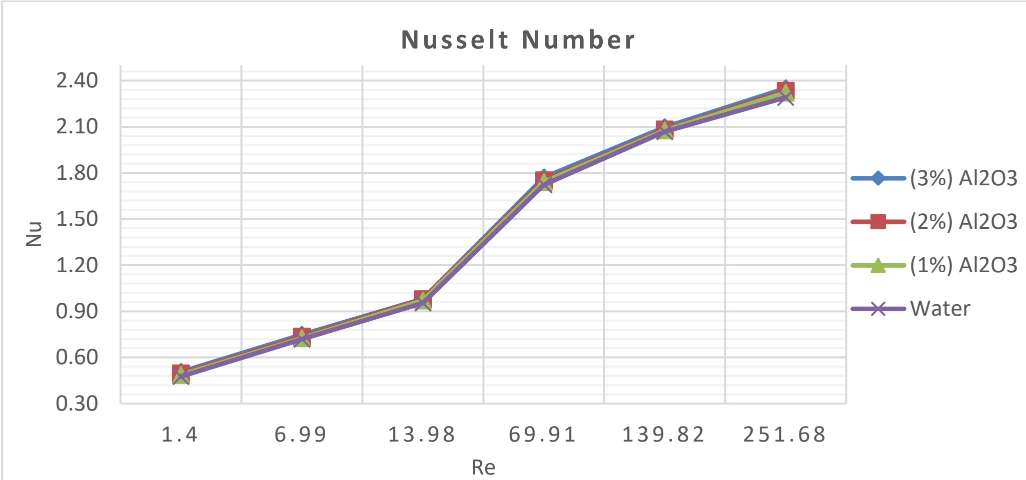

Figure 4.19 Nusselt number vs reynolds number for water and aluminum oxide solutions (1%, 2% and 3%).

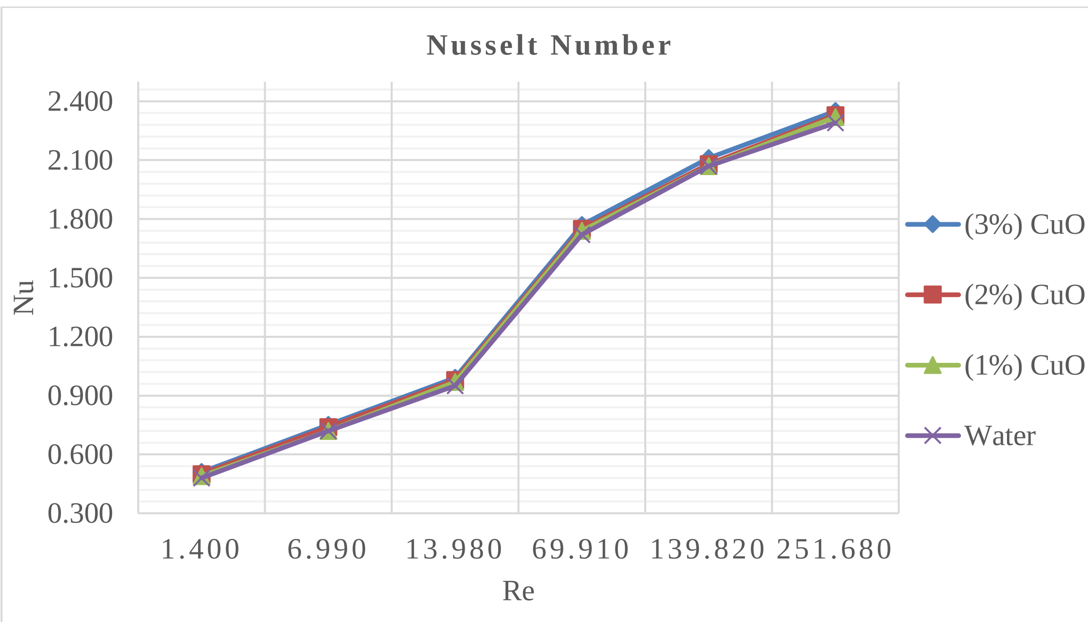

Figure 4.20 Nusselt number vs reynolds number for water and copper oxide solutions (1%, 2% and 3%).

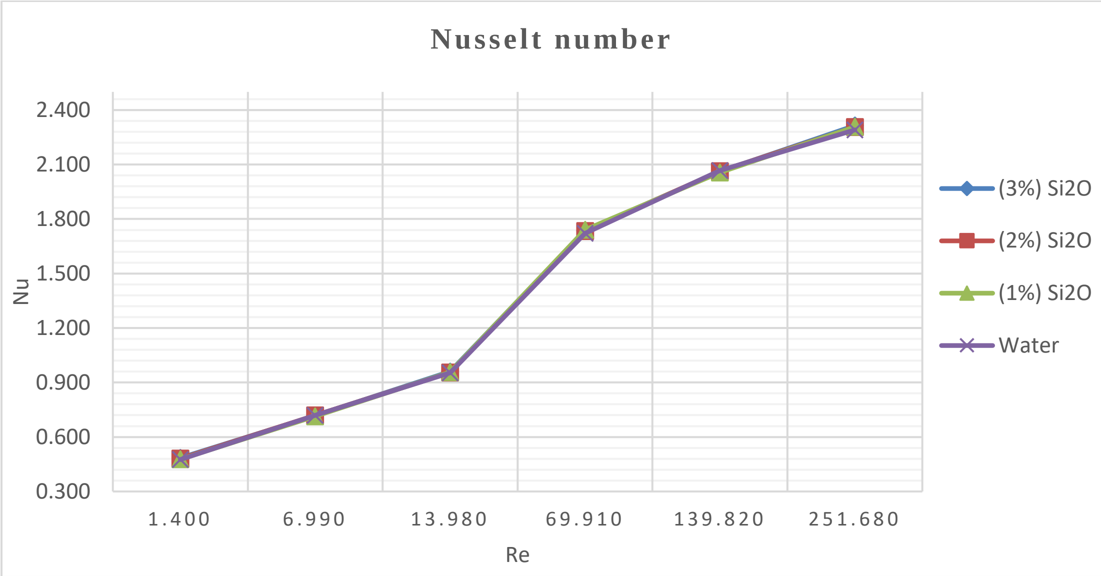

Figure 4.21 Nusselt number vs reynolds number for water and silicon oxide solutions (1%, 2% and 3%).

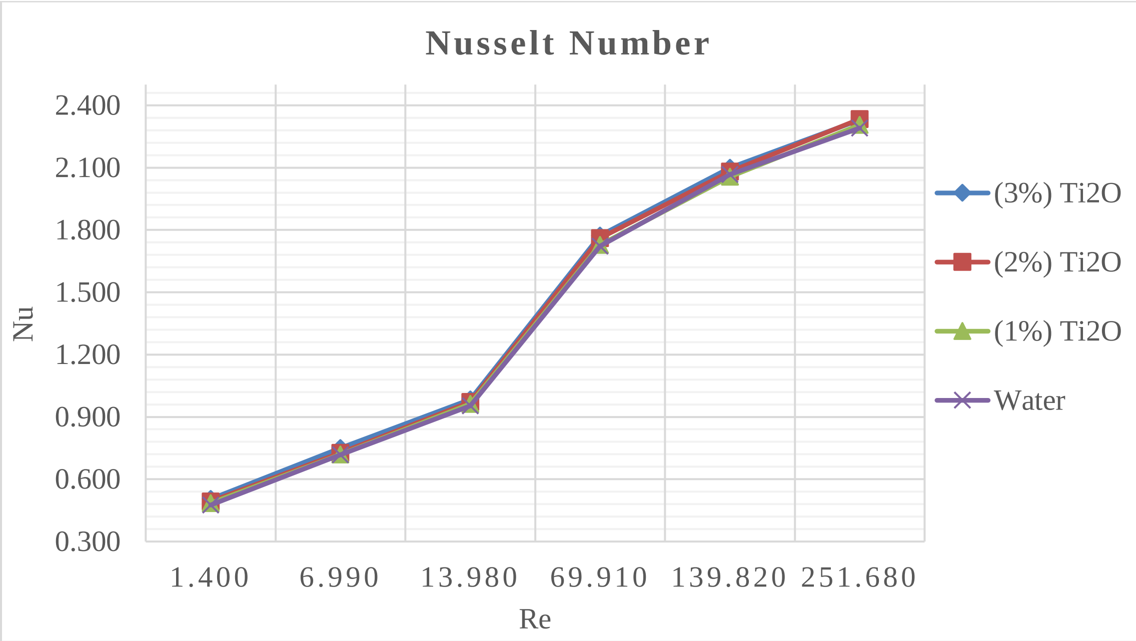

Figure 4.22 Nusselt number vs reynolds number for water and titanium oxide solutions (1%, 2% and 3%).

As shown in Fig.4.19 the average Nusselt number (heat transfer coefficient) of Al_2O_3 is greater than that of water by 1.3813%, 2.2859% and 3.3429% for 1%, 2% and 3% vol. concentration of Al_2O_3 respectively.

Similarly, 1.1477%, 2.1602% and 4.1423% increment for 1%, 2% and 3% vol. concentration of CuO as shown in Fig. 4.20. In addition, 0.2342%, 0.4266% and 0.6887% improvement for Si_2O under similar vol. concentration with CuO and Al_2O_3. Finally the average Nusselt number (heat transfer coefficient) of Ti_2O is greater than that of water by 0.4774%, 3.2021%, and 3.3011% for 1%, 2% and 3% vol. concentration respectively as shown in Fig.4.22.The numerical values are listed in Appendix (Table A10-A13). For the higher concentration, the variation is significant however, for lower concentration the graph is steeper. This is due to the open loop system and the small size of collector. In open loop system the fluid intering the collector leaves the collector and do not recycle in the system. As a result the temperature the working fluid can harvest from the collector become less.

Generally, the heat transfer coefficient increases with increase in concentration. The SFPC using nanofluids has better heat transfer enhancement than that of SFPC using water. The result also reveal that the SFPC with CuO has the best thermal performance enhancement as shown in Fig.4.23. The CuO nanofluids has higher performance of 19.29, 20.31 and 83.37% more than Al_2O_3, TiO_2 and SiO_2 nanofluids respectively. similarly the Al_2O_3 has performance of 1.25 and 79.39% more than TiO_2 and SiO_2 nanofluids respectively. lastly the TiO_2 has 79.13% more thermal performance than SiO_2.

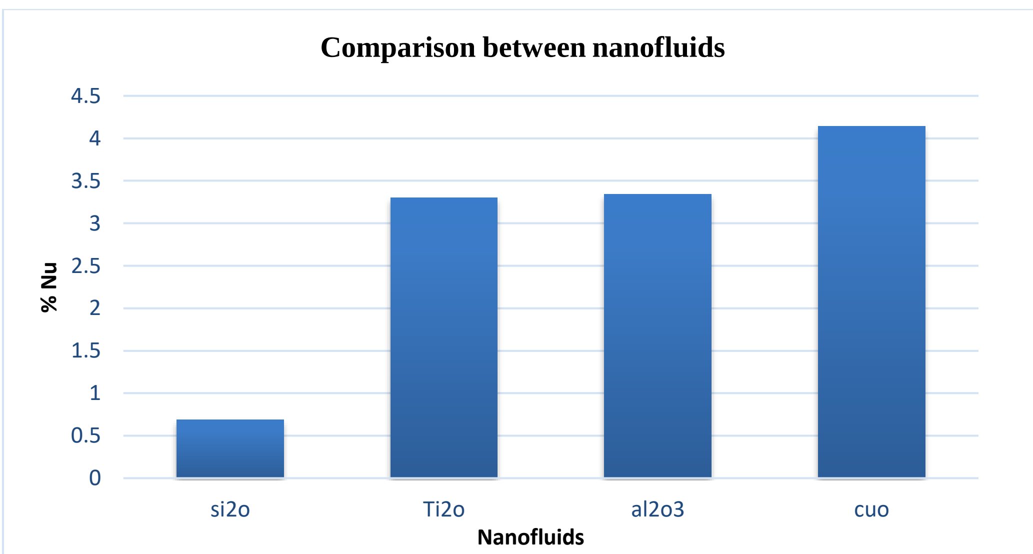

Figure 4.23 The nusselt number comparison for different nanofluids for 3% volume concentration at V_{in} = 0.01 m/s for June 11, 2018.

4.6 Pressure drop

The pressure drop versus flow length graph for different vol.concentration of Al_2O_3 and SiO_2 was shown in Fig.4.24 and 4.25 respectively. Whereas for 1% vol. concentration the pressure drop versus flow length graph was given in Fig.4.24.

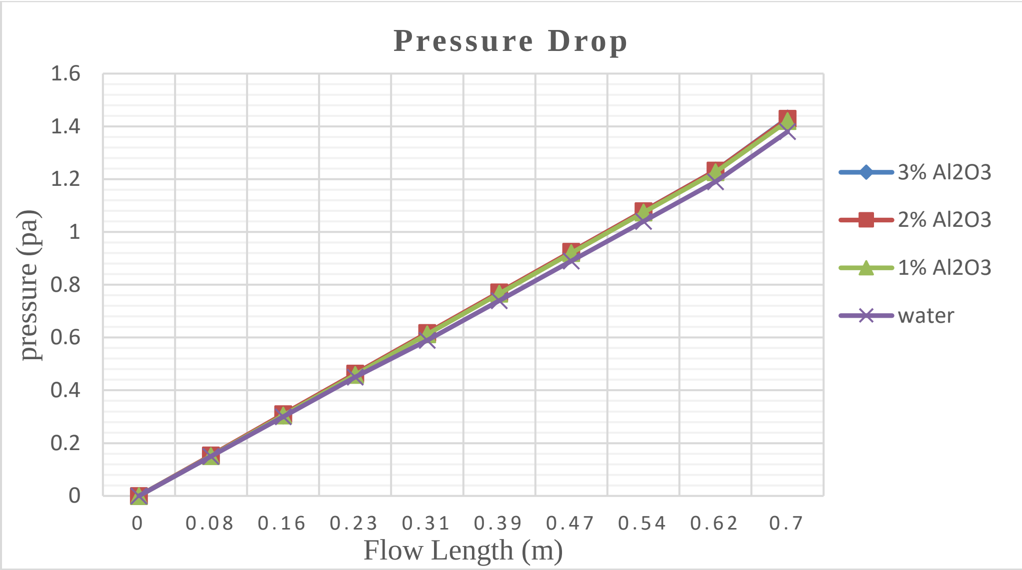

Figure 4.24 The pressure drop with different Al_2O_3 concentration.

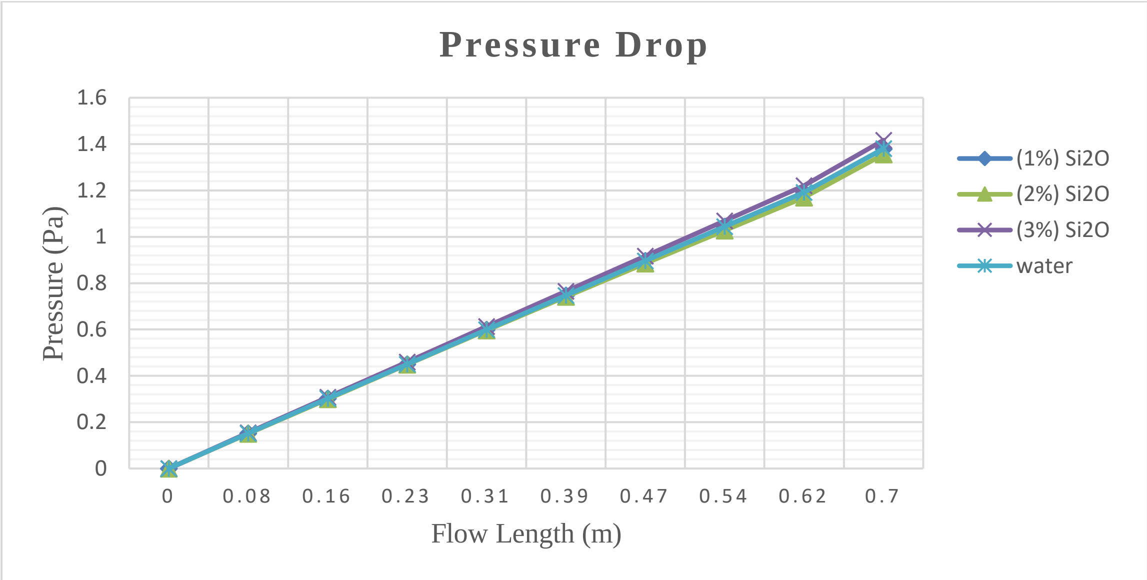

Figure 4.25 The pressure drop with different SiO_2 concentration.

There is slight increase in pressure drop due to increase in volume concentration of nanoparticles. This increment have no effect on the pump power requirement. The result is similar in all nanofluids cases the pressure drop is insignificant at lower concentration as shown in Fig.4.24 & Fig.4.25.

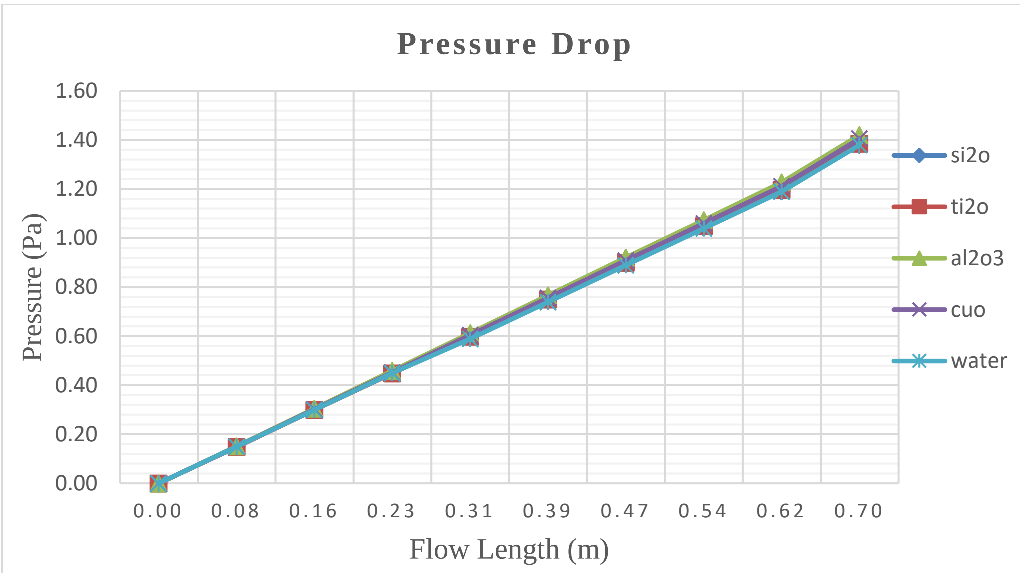

Figure 4.26 The pressure drop with different nanofluids of (1%) volume concentration.

The higher-pressure drop experiences using nanofluid because of its higher density, as explained by (Faizal.M., (2014). However, at higher concentration this may not happen. Similarly, for different nanofluids the pressure drop is almost similar and has no significant effects on the pumping power as shown in Fig.4.26.

4.7 Theoretical efficiency for open loop system

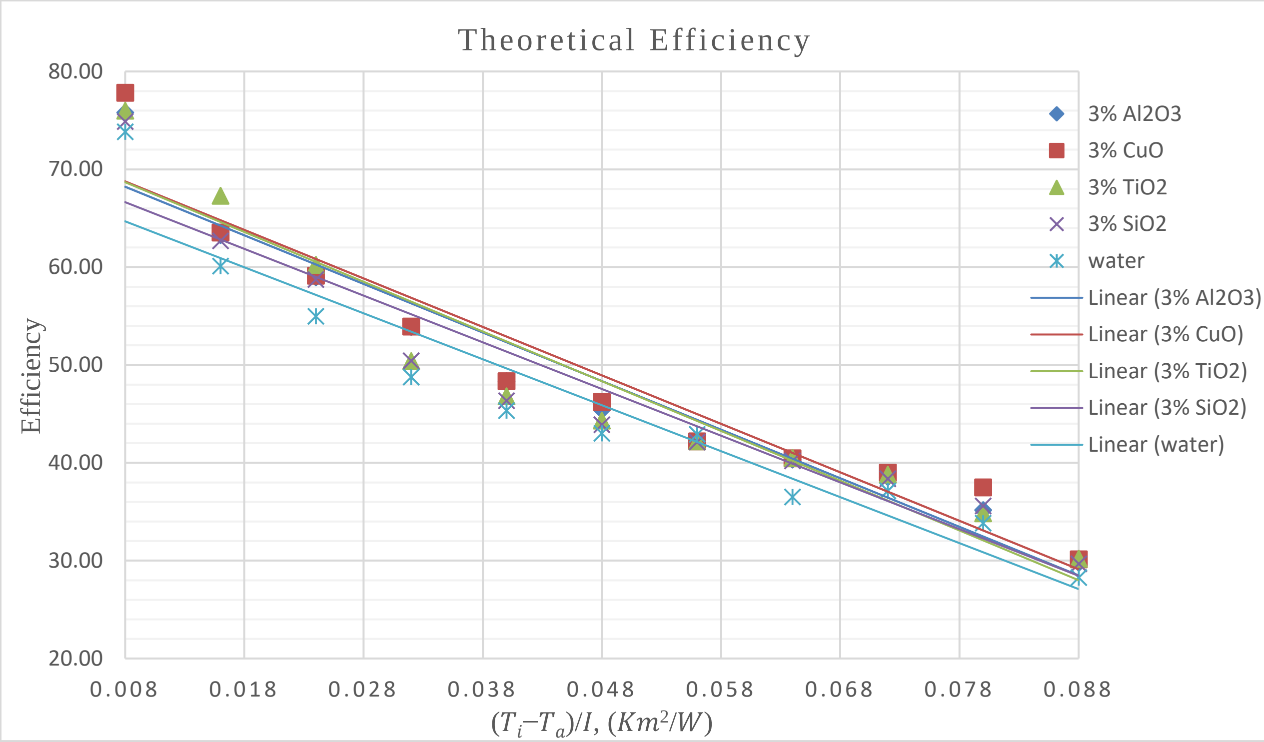

Figure 4.27 Efficiency of various nanofluids-based SFPC and water SFPC.

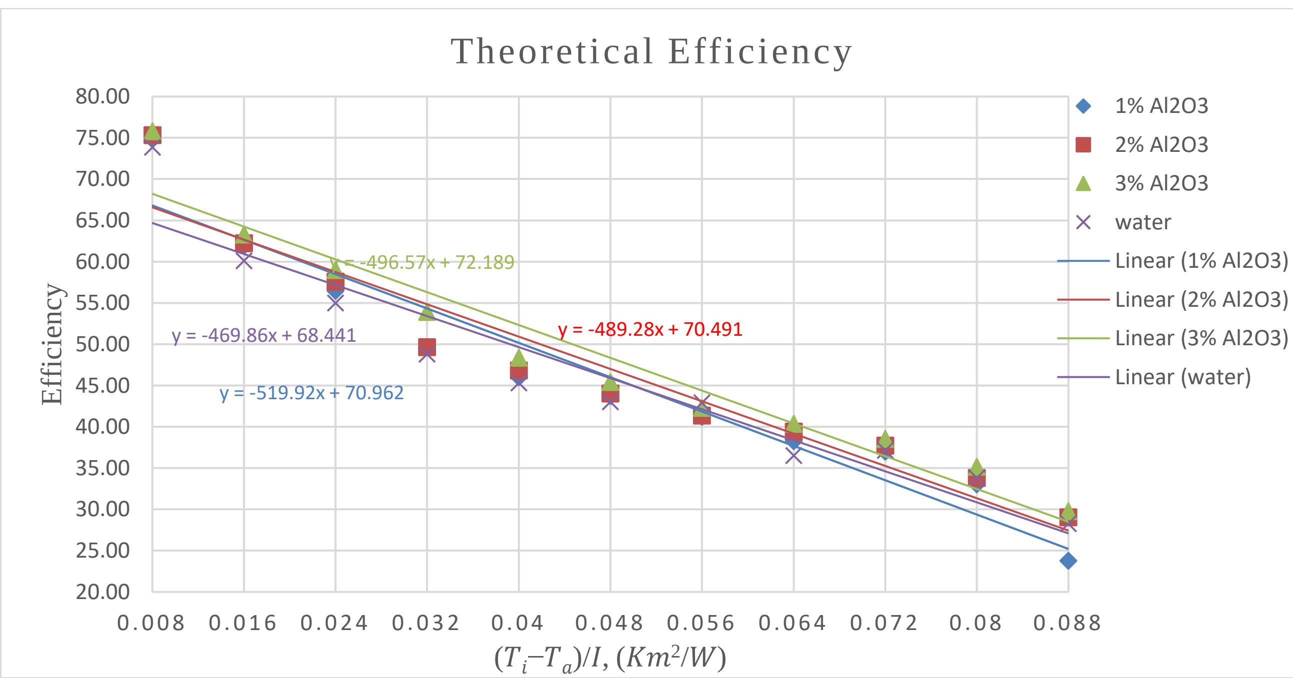

Figure 4.28 Efficiency of various vol. concentration Al_2O_3 nanofluids-based SFPC and water SFPC.

The theoretical efficiency decreases with heat loss parameter $\frac{T_i - T_a}{I}, \left(\frac{K\,m^2}{W}\right)$ as shown in Fig.4.27 and Fig.4.28. The efficiency of CuO nanofluid-based SFPC is 77.82% and greater than the others where as SiO_2 nanofluid-based SFPC is 74.87%, which is less than other collector except water-based SFPC. Figure 4.28 shows that increasing concentration of nanofluids maximize the efficiency of collector. From both graph one can understand that the graph is steeper at the bottom right corner this happen because the nanofluids have low specific heat than water.

4.8 Efficiency for closed loop solar flat plate colletor system

The instantaneous efficiency of SFPC is affected by ambient temperature, solar radiation, and outlet temperature of collector. Due to the effectiveness of the heat exchanger, the inlet temperature of the collector increases unlike that of open loop collector. The outlet temperature was measured using K-thermocouple in hourly basis. The instantaneous efficiency versus heat loss parameter is given in Fig.4.30. The graphs of experimental and numerical results is similar in shape; however, there is the difference in value as shown in Fig.4.31. This variation comes from the difference in system by itself (open loop and closed loop), convection, radiation, side and bottom losses, and pipe loss.

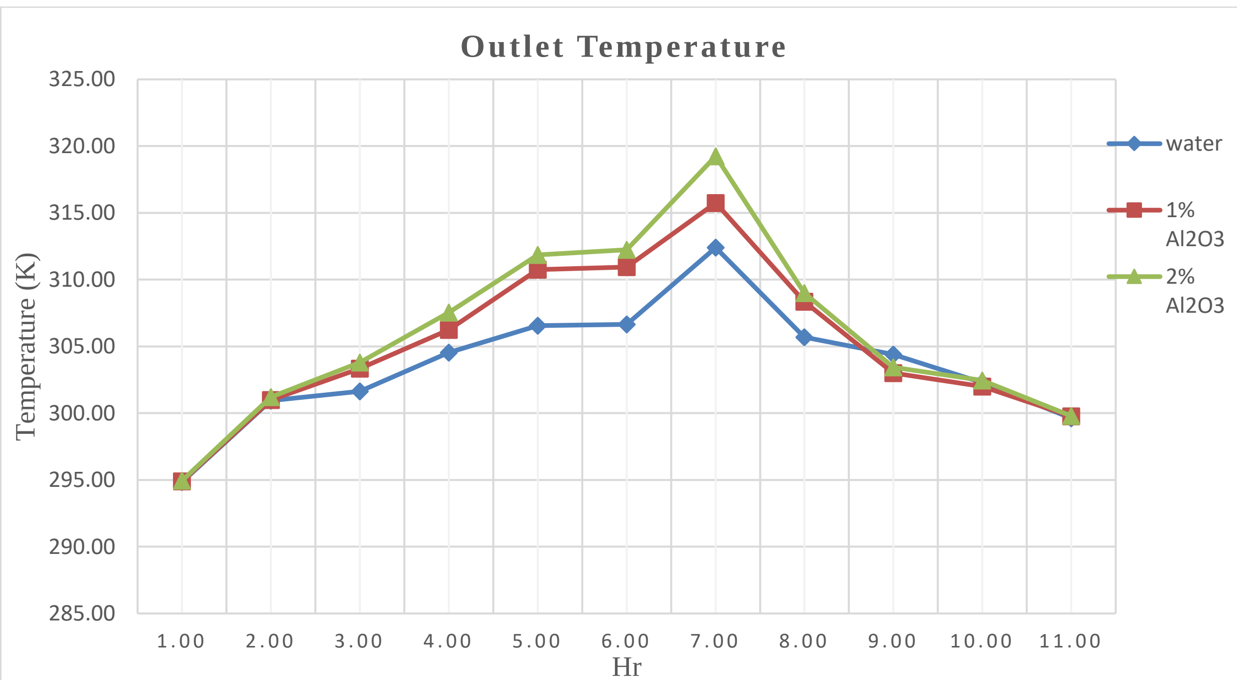

Figure 4.29 Outlet temperature of water from collector (Experimental)

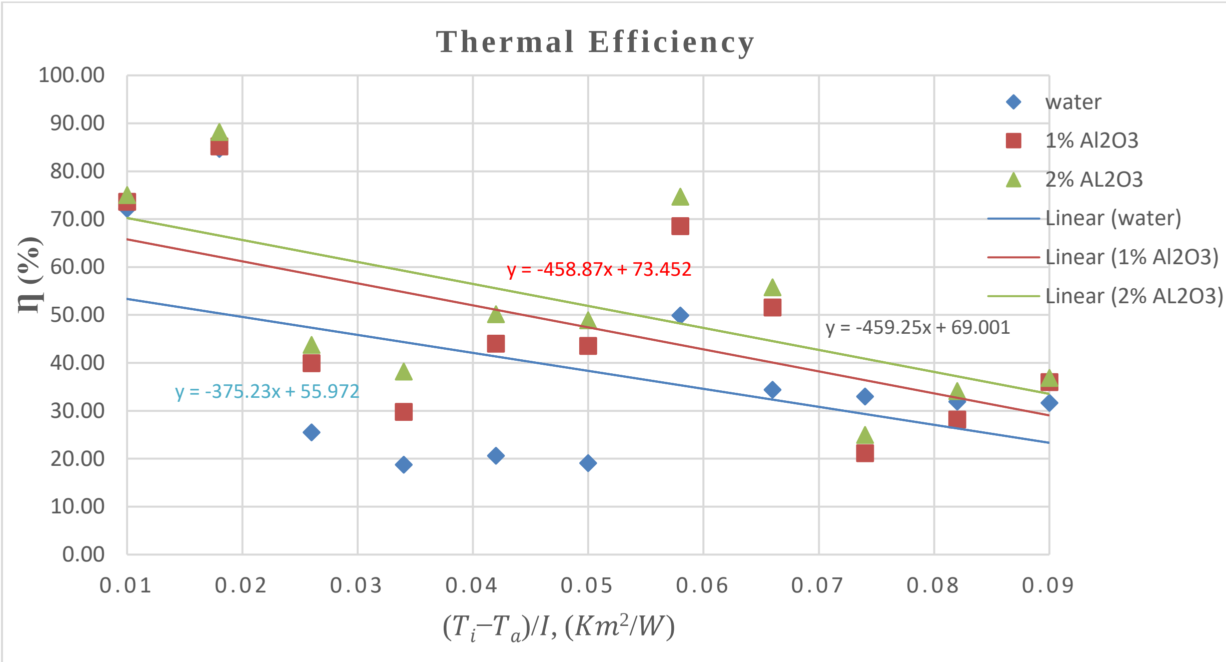

Figure 4.30 Thermal efficiency of collector (Experimental)

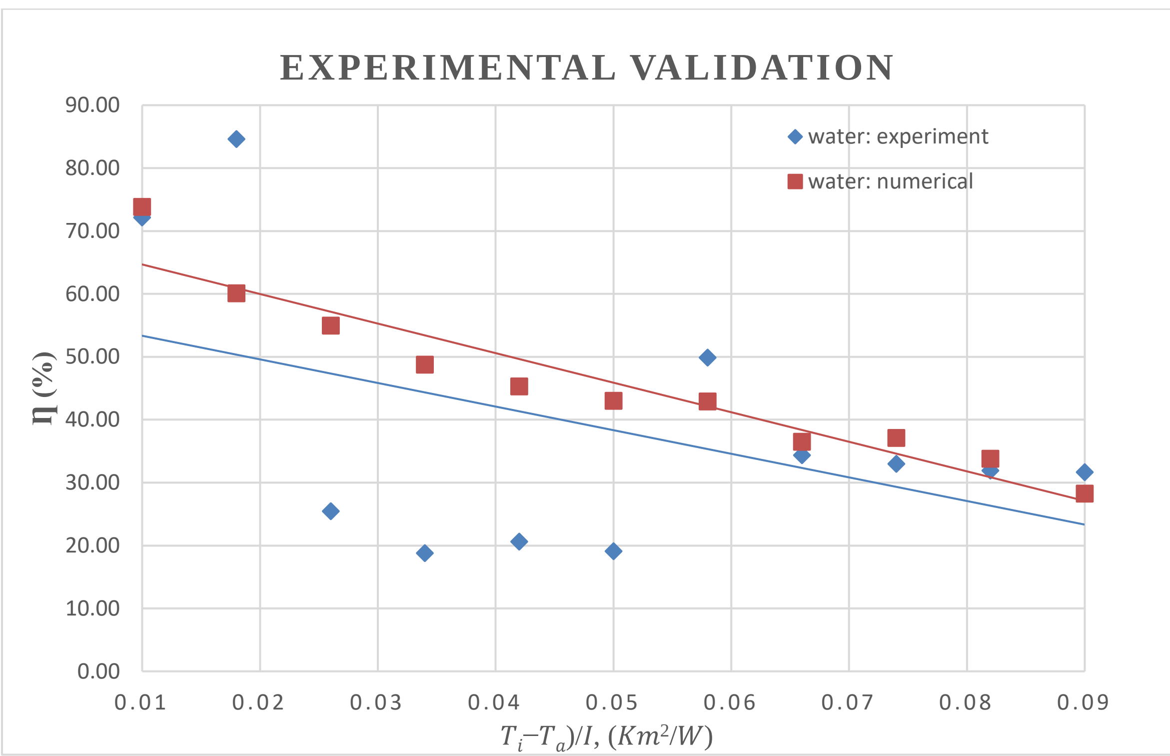

Figure 4.31 Comparison between numerical and experiment values $\dot{m} = 0.0137\ kg/s$.

The experimental result shows the efficiency of flat plate collector using water as working fluid is about 19.12% at noon. After using nanofluid as working fluid in amount of 1% volume concentration of Al_2O_3, the efficiency increased to 43.56% whereas for 2% Al_2O_3 increased to 48.87% as shown in Fig.31.

The experimental range of values of efficiency ($\eta \pm \sigma$) for water, 1% Al_2O_3, and 2% Al_2O_3 based solar flat plate collector are 35.14 ± 7.56, 43.46 ± 6.58, and 47.56 ± 4.33, respectively. The uncertainity error of the efficiency of collectors in percentage was 1.32, 1.51, and 1.55% for water, 1% Al_2O_3 and 2% Al_2O based SFPC, respectively as shown in Fig 4.30. The difference between the experimental and numerical validation interms of uncertainity was 1.32 and 2.31%, respectively as shown in Fig 4.31.

The efficiency of collector using water is less due to the fact that water has less thermal conductivity than nanofluids. The experimental values are given in table form in Appendix (Table A6). The efficiency of water based SFPC is lower smaller than the other nanof;uid based solar flat plate collector because of higher thermal conductivity in nanofluids.

CHAPTER FIVE

ECONOMIC and ENVIRONMENTAL ANALYSIS

5.1 Embodied energy analysis

Embodied energy is only the energy used to manufacture the solar collector neglecting the distribution, disposal, maintenance and other phases of collectors. The 70% of the collector-embodied energy comes from the manufacturing of the collector. So that the analysis is done with the reduction in area as parameters that influencing the weight and embodied energy of the collector. The reduction in area of the collector for different nanofluids is given by

$$A_p = \frac{\dot{m}c_p(T_{out}-T_{in})}{I_T\eta} \quad \text{...(5.1}$$

Table 5.1 Area reduction of collectors of different nanofluids.

Different Nanofluids collectors	**Area in m²**		
	1%	**2%**	**3%**
Al_2O_3	0.012023	0.012110	0.012429
CuO	0.012036	0.012116	0.012532
TiO_2	0.012012	0.012091	0.012328
SiO_2	0.012000	0.012078	0.012177

Two major materials are used in the solar collector namely glass and copper with the weight ratio of 27 kg glass and 9 kg copper for a 36 kg collector. The embodied energy indices are 15.9 and 70.6 MJ/kg for the glass and the copper, respectively (Otanicar, 2010). For 3% vol. concentration, the weight and embodied energies for this study are calculated based on the above ratio and tabulated in Table 5.1. Table 5.1 shows the reduction of area for different nanofluids SFPC compared to conventional SFPC. As shown in tables the CuO collector have higher area reduction.

5.1.1 Economic analysis

Currently the electricity cost in Ethiopia is \$0.09/kWh, which is annually \$259.2 for 8 hrs of daily operation. The residential 120 VAC electric tank-less water heater 33.5 kW power is \$165. So that totally \$424.2 electricity cost can be saved by using solar water heater.

Table 5.2 Cost of various SFPC

No.	Area based cost					
	Materials	Price in dollar($)				
		water	Al_2O_3	CuO	TiO_2	SiO_2
1.	copper tube	50.0000	47.8530	47.8507	47.8550	47.8571
2.	copper plate	333.3300	319.0170	319.0016	319.0301	319.0444
3.	wood	33.3300	31.8988	31.8973	31.9001	31.9016
4.	glass	16.6700	15.9542	15.9534	15.9549	15.9556
	Independent cost($)					
5.	pump	66.6700	66.6700	66.6700	66.6700	66.6700
6.	elbow	50.0000	50.0000	50.0000	50.0000	50.0000
7.	plastic pipe	16.6700	16.6700	16.6700	16.6700	16.6700
8.	valves	33.3300	33.3300	33.3300	33.3300	33.3300
9.	Nanoparticles (100gm)	-	15	17	14	12
10.	sealant	8.0000	8.0000	8.0000	8.0000	8.0000
11.	coating	6.6700	6.6700	6.6700	6.6700	6.6700
Total		614.67	611.063	613.043	610.0801	608.0987
	Electricity cost saving per year($)					
12.	424.2					
Years until electricity savings = costs		1.449	1.4405	1.445	1.438	1.4335

The cost saving of nanofluids SFPC is greater than the water SFPC due to their higher efficiency. Table 5.2 shows the cost saving and payback period of each solar collectors. Accordingly, the return period for nanofluids SFPC are less than that of water solar collector. The CuO SFPC has better energy saving solar collector, which is 4.4387% of total embodied energy of conventional SFPC.

Table 5.3 Weight and embodied energy of different collector.

Different Nanofluids solar heater and water solar heater	**Weight(kg)**		**Embodied energy (MJ)**			**Energy Saving (%)**
	Glass	**copper**	**glass**	**Copper**	**Total**	
Water	4.1250	1.3750	65.5870	97.0750	162.6625	-
Al_2O_3	3.94189	1.31397	62.6760	92.7663	155.4423	4.4387
CuO	3.94037	1.31346	62.6520	92.7303	155.3823	4.4756
TiO_2	3.94338	1.31446	62.6997	92.8009	155.5006	4.4030
SiO_2	3.94561	1.31520	62.7352	92.8531	155.5883	4.0350

The manufacturing of the CuO nanofluids-based solar collector results in around 61.065 kg less CO_2 emissions compared to a conventional solar collector as shown in Table 5.4. Similarly, Table 13 demonstrates the damage cost of various nanofluid-based solar collector and water based solar collector. The damage cost of nanofluid-based solar collector is lower than that of water based solar collector.

Table 5.4 Embodied energy emissions from various working fluid solar collectors

	Solar heater water	**Al_2O_3**	**CuO**	**TiO_2**	**SiO_2**
Embodied energy(MJ)	162.6625	155.4423	155.3823	155.5006	155.5883
Emissions (kg)					
Carbon dioxide, CO_2	98.7361	94.3535	94.3171	94.3889	94.4421
Sulfur oxides, SOx	0.0490	0.0468	0.0468	0.0468	0.0468
Nitrogen oxides, NOx	0.0856	0.0818	0.0817	0.0818	0.0818

Table 5.5 Annual damage costs for various working fluid solar collectors

	Cost (USD/kg)	Damage costs (USD)				
		Solar heater water	**Al_2O_3**	**CuO**	**TiO_2**	**SiO_2**
Carbon dioxide, CO_2	0.0300	2.9621	2.8306	2.8295	2.8317	2.8333
Sulfur oxides, SOx	11.2400	0.5503	0.5259	0.5257	0.5261	0.5264
Nitrogen oxides, NOx	17.0500	1.4588	1.3941	1.3935	1.3946	1.3954
Total (USD)	-	4.9712	4.7506	4.7487	4.7523	4.7550

The water and nanofluids solar flat plate collector saved about 3.0882 kg and 3.1468 kg of coal respectively with the dimension of collector used in this study. Table 5.6 shows the amount of coal saved replacing the coal by solar water and nanofluid-based SFPC. As a result, the pollutant released to environment is reduced as shown in Table 5.6.

Table 5.6 Comparison between the solar water heater energy saving with energy from coal.

	Coal	**Water-based SWH**	**Al_2O_3(1%)-based SWH**
Energy (MJ)	29.306/ kg of coal	30.9076 MJ per day = 1.054 kg coal saved	31.147 MJ per day = 1.074 kg coal saved
CO_2 emission(kg)	2.93/ kg of coal	3.0882	3.1468
SO_2 emission(kg)	0.0123/ kg of coal	0.012964	0.01321

CHAPTER SIX

CONCLUSIONS, RECOMMENDATIONS and FUTURE WORKS

Conclusions

In this study, the flow and heat transfer characteristics of four nanofluids (i.e. Si_2O, Ti_2O, Al_2O_3 and CuO) in SFPC are studied and compared with that of water. The study is done for different inlet velocity (i.e. $V_1 = 0.001$ m/s, $V_2 = 0.005$ m/s, $V_5 = 0.01$ m/s and $V_5 = 0.018$ m/s) or (1.4 – 252) in terms of Reynolds number and for 1%, 2% and 3% volume concentration. The conventional flat plate collector rises the water temperature by 19 ℃.

The numerical simulation results shows that, the conventional flat plate collector rises the water temperature by 19 ℃. Adding the nanoparticles into base fluid increases the heat transfer (Nusselt number). Accordingly, 0.6887%, 3.3011%, 3.3429%, 4.1423% increment in Nusselt number was achieved using 3% of Si_2O, Ti_2O, Al_2O_3 and CuO respectively compared to that of water. The CuO nanoparticle has greater improvement than other nanoparticles and Si_2O has lower improvement than the other nanoparticles. Increasing the concentration of nanoparticles rises the heat transfer coefficients. For instance, 1.1477%, 2.1602% and 4.1423% increment of Nusselt number for 1%, 2% and 3% vol. concentration of CuO achieved. Therefore, the heat transfer coefficient and nusselt number depends on the nanoparticles and volume concentration of nanoparticles. In another angle, using nanofluids or increasing the nanoparticles volume concentration will have insignificant influence on the pressure drop.

The efficiency of flat plate collector using water as working fluid is about 19.12% at noon. After using nanofluid as working fluid in amount of 1% volume concentration of Al_2O_3, the efficiency increased to 43.56% whereas for 2% Al_2O_3 increased to 48.87%.

The CuO SFPC has better energy saving solar collector, which is 4.4387% of total embodied energy of conventional SFPC. The manufacturing of the CuO nano-fluids-based solar collector results in around 61.065 kg less CO_2 emissions compared to a conventional solar collector. In addition, the return period for nanofluids SFPC are less than that of water solar collector

Recommendations

Mostly nanofluids performance will decrease after used for long period. Therefore, changing the circulating fluid after usage period is recommended. Additionally, safety is required while replacing the working fluid.

Future works

This study can be considered as the starting point or foundation for coming studies and findings as well. For future researches, this study can be a more viable in household, industrial and other energy sectors for better energy saving and cost saving opportunities. The expected suggestions and recommendations are as follows:

- ✓ In this study, it has assumed the laminar flow and steady flow of fluid. study on the flow of fluid in SFPC for turbulent and transient flow also recommended.
- ✓ This study more focus on the CFD simulation of flat plate collector not includes the thermal energy storage enlarge. Therefore, it has suggested that including the energy saving in thermal storage increase the energy saving in the system.
- ✓ The similar study in evacuated tube, parabolic trough and other collector are recommended and taken as future work.

REFERENCES

Abbas, S. S., & Ali, A. A. (2017). Experimental and Numerical Study the Heat Transfer of Flat Plate Solar Collector by Using Nanofluid under Solar Simulation,. *ARPN Journal of Engineering and Applied Sciences, Vol. 12, No. 13,*.

Ahmad M. Saleh. (2012). Modeling of Flat-Plate Solar Collector Operation in Transient States Purdue. *University Fort Wayne, Indiana,* .

Akhatova J. S., A., S. Z., Mirzaevb, A. S., H., S. S., T., & E. T., J. (2017). Study of The Possibilities of Thermal Performance Enhancement of Flat Plate Solar Water Collectors By Using of Nanofluids as Heat Transfer Fluid. *Applied solar energy,*.

Ald Vieira, d. R. (2012). *Fundamentals of Renewable Energy Processes,.* Elsevier Academic Press.

Ali, H. A.-W., Miqdam, T. C., Hussein, A. K., K., S., & Javad, S. (2018). Numerical study on the effect of operating nanofluids of photovoltaic thermal system (PV/T) on the convective heat transfer,. *Case Studies in Thermal Engineering,*.

Ali, N. J. (2018). A Review on Nanofluids: Fabrication, Stability, and Thermo-physical Properties,. *Journal of Nanomaterials Article ID 6978130,*, 33.

Ali, R., Yousefnejad, M., Mahdi, H., & Amir, H. M. (2016). Experimental Study of nanofluid effects on heat transfer in closed cycle system in shell and tube heat Exchangers at Isfahan power plant,. *Energy Equipment and Systems,*.

Alok Kumar. (2014). Performance of Solar Flat plate by using Semi- Circular Cross Sectional Tube, . *International Journal of Engineering Research and General Science Volume 2, Issue* .

Alok Kumar. (2014). Performance of Solar Flat plate by using Semi- Circular Cross Sectional Tube,.

Amina, B., Miloud, A., Sami, L., Abdelylah, B., & J.P., s. (2016). Heat transfer enhancement in a parabolic trough solar receiver using longitudinal Fins and nanofluids,. *journal of thermal science vol.25, no. 5 :410-417*.

Aminreza, N., Ebrahim, H., & M., M. (2016). Experimental investigation of efficiency of square flat-plate solar collector using SiO2/water nanofluid. *Case Studies in Thermal Engineering,DOI: 10.1016/j.csite.2016.08.006*.

Anin, V. ,., & Natarajan, E. (2017). Performance Enhancement Studies in a Thermosyphon Flat Plate Solar Water Heater with CuO Nanofluid,. *THERMAL SCIENCE: Vol. 21, No. 6B, 2*, 2757-2768.

AntonyJ, P., S., Dhinesh k., & D., B. (2017). A Performance Comparision of Nanofluids Using Solar Flat Plate Collector and Flow is Simulated in Computational Fluid Dynamics (CFD) Analysis,. *BAOJ Nanotech , 3: 23: 017, Volume 3; Issue 1; 017*.

Baccoli, R., Mastino, C., Innamorati, R., Serra, L., Curreli, S., Ghiani, E., . . . Marini, M. (2015). A mathematical model of a solar collector augmented by a flat plate above reflector: Optimum inclination of collector and reflector,. *ScienceDirect Energy Proc*.

Bekele, A. (2007). Large Scale Application Of Solar Water Heating System In Ethiopia.

Billy, A. S. (2010). Effect of Absorber Plate Material on Flat Plate Collector Efficiency. *University Malaysia Pahang1*.

Blaga, A. (1978). Use of plastics in solar energy applications. *Solar Energy 21, No 4*, 331-339.

Bozorgan, N. S. (2015). Performance evaluation of nanofluids in solar energy. A review of the recent literature. *springer*, 2-15.

Brunelli A., G. P. (2013). *Nanopart. Res., 15 (6), 1684.DOI:10. 1007/s11051-013-1684-4,* .

Stanciu C., D. A. (2016). Analysis of a flat plate collector for hot Water Domestic use – a sensitivity study,. *IOP Conference Series: Materials Science and Engineering,*.

Canivan, J. (2009). *solar water heater.*

Dawit, G. G., & Robi, P. S. (2016). CFD and experimental investigation of flat plate solar water heating system under steady state condition. *Renewable energy*, 26.

Dawit, k. (2016). Design and analysis of solar thermal system for hot water supply to Minilk II hospital new building.

Debashis, D. P. (2017). A review of nanofluid preparation, stability, and thermo-physical properties,. *Wiley Periodicals, Inc.,*.

Delfani, S., Karami, M., & Akhavan, M. A. (2014). Experimental investigation on performance comparison of nanofluidbased direct absorption and flat plate solar collectors. *Int. J. Nano Dimens., 7(1): 85-96, Winter 2016,DOI: 10.7508/ijnd.2016.01.010*.

Dimitrios, P. (2015). Solar Water Heating Systems Study Reliability, Quantitative Survey and Life Cycle Cost Method. *Department of Mechanical Eng., University of Strathclyde in Glasgow.*

Duffie and Beckman. (1991). *Solar Engineering of Thermal Processes. 4th edition,.* New York: J. Wiley and Sons,.

Ehsan, E.-B., Mohammad, C. M., Hamid, N., & Somchai, W. (2016). Experimental and Numerical Investigation of Nanofluids' Heat Transfer Characteristics for Potential Application in Solar Heat Exchangers,. *International Journal of heat exchanger.*

Ekramian E., E., S. Gh., E., & M., H. (2014). Numerical Investigations of Heat Transfer Performance of Nanofluids in a Flat Plate Solar Collector,. *International Journal of Theoretical and Applied Nanotechnology Volume 2, ISSN: 1929-1248 DOI:,*.

Faizal, M. S. (2014). Energy economic and environmental analysis of a flat-plate solar collector operated with SiO2 nanofluid,. *Clean Techn Environ Policy DOI 10.1007/s10098-014-0870-0,*.

Kabeel A.E., Z. O. (2014). Enhancement of modified solar still integrated with external Condenser using nanofluids: An experimental approach, . *Energy Conversion and Management, 78 (2014) 493–498*.

Kumaresan G. and S.Venkatachalapathy. (2014). Heat transfer studies on circular heat pipes using CuO nanofluids,. *international journal of mechanical and production engineering ISSN: 232-2092, vol.2, issue* .

Gutu Birhanu, D. A. (2016). Computational Fluid Dynamic Simulation and Experimental Testing of a Serpentine Flat Plate Solar Water Heater, . *International Journal of Scientific & Engineering Research, Volume 7, Issue 10,* .

Al-Waelia H.A, A.,, Chaichanb, M. T., Kazemc, H. A., & K. Sopiana, J. S. (2018). Numerical study on the effect of operating nanofluids of photovoltaic thermal system (PV/T) on the convective heat transfer, . *Case Studies in Thermal Engineering,*.

Zhu H.-t., Y.-s. L.-s. (2004). *Colloid Interface Sci. 277 (1), 100–103. DOI: 10.1016/j.jcis.2004.04.026.*

Haitao Zhu, c. a. (2011). Preparation and thermal conductivity of CuO nanofluid via a wet chemical method. *Nanoscale Res Lett. 2011; 6(1): 181.*

Hamed, A. F. (2017). Investigation of the Effect of Different Nanofluids in a Solar Collector,. *Engineering, Technology & Applied Science Research Vol. 7, No. 4, , 1741-1745 1741*.

Hawwash A.A.,, K., A., S., A.-R., & S.A., O. (2016). Nada Experimental Study of Alumina Nanofluids Effects on Thermal Performance Efficiency of Flat Plate Solar Collectors,. *Journal of Engineering Technology (JET) DOI: 10.5176/2251-3701_4.1.183,*.

He Qinbo, S. Z. (2015). Experimental investigation on the efficiency of Flat-plate solar collectors with nanofluids,. *Applied Thermal Engineering,*.

Himangshu Bhowmik and Ruhul Amin. (2017). Efficiency improvement of flat plate solar collector using reflector,. *Energy Reports 3*, 119–123.

http://slideplayer.com/slide/images/Types+of+solar+collectors.

https://images.search.yahoo.com/yhs/search?p=. (n.d.).

https://images.search.yahoo.com/yhs/search?p=Types+of+solar+collectors&fr=yhs-trp-001&hspart. (n.d.).

Huminic, G., & Huminic, A. (2013). Experimental and Numerical Investigations of the Thermal Performances of Wickless Heat Pipes Using Nanofluids,. *Termotehnica 1,*.

Incropera, D. B. (n.d.). *Fundamental of heat and mass transfer Sixth edition.*

Incropera, F. P., & DeWitt, D. P. (2007). Fundamentals of Heat and Mass Transfer (6th ed.),. Hoboken: Wiley.ISBN 978-0-471-45728-2,.

International Energy Agency. (2014).

kiran J.A, R., k., K., s., & Rao, S. (2015). Numerical Analysis and Validation of Heat Transfer Mechanism of Flat Plate Collectors,. *Science Direct International Conference On Computational Heat and Mass Transfer,*.

Eastman J.A., U. S. (1997). Enhanced thermal conductivity through the development of nanofluids. *Materials Research Society Symposium-Proceedings, Materials research Society, Pittsburgh, PA, USA, Boston, MA, USA, vol.457:pp.3-11,*.

Jims, G. J., & Koshy, P. M. (2014). Experimental Analysis of a Flat Plate Solar Collector System for Small-Scale Desalination Applications. *Advanced Materials Research Vols. 984-985 (2014) pp 800-806,doi:10.4028/www.scientific.net/AMR.984-985.800*.

John, R. C., & Howell, B. R. (1982.). *Solar Thermal Energy System.* USA,.

Mavani A.M. and Patel J.R.. (2014). Effect of Nanofluids and Mass Flow Rate of Air on Heat Transfer Rate in Automobile Radiator by CFD Analysis,. *Volume: 03 Issue: 06 | Jun-*.

Muhammed K. A., Y. a. (2015). Analysis of Heat Transfer Performance of Flat Plate Solar Collector using CFD,. *International Journal of Science, Engineering and Technology Research (IJSETR), Volume 4, Issue 10,*.

Vasudeva K. Karanth1 and Jodel A. Q. Cornelio. (2017). CFD Analysis of a Flat Plate Solar Collector For Improvement in Thermal Performance with Geometric Treatment of Absorber Tube,. *International Journal of Applied Engineering Research ISSN 0973-4562 Volume 12, N*.

Karanth, K., Vasudeva, M., & Yagnesh, M. S. (2011). Numerical Simulation of a Solar Flat Plate Collector using Discrete T ransfer Radiation Model (DTRM) – A CFD Approach. *Proceedings of the World Congress on Engineering 2011 Vol III*.

Knoema Corporation{US}. ({1970-2016}). Ethiopian co2 emmisions per capita.

Lee JH, H. K. (2008). Effective viscosities and thermal conductivities of aqueous nanofluids containing low volume concentrations of Al2O3 nanoparticles. . *Int J Heat Mass Trans. 2008;51:2651–656. doi: 10.1016/j.ijhea*.

Li, Y. (2009). "A review on development of nanofluid preparation and characterization,. *" Powder Technology, vol. 196, no. 2,*, pp. 89–101,.

Li, Y., Zhou, J., Tung, S., Schneider, E., Xi, & S. (2009).). A review on development of nanofluid preparation and characterization,. *Powder Technology, vol. 196, no. 2*, 89–101.

Lida Ebrahimi Vafaeia and Melike Sahb. (2017). Predicting efficiency of flat-plate solar collector using a Fuzzy inference system, . *Science Direct, Procedia Computer Science 120* , Page (221–228).

Elmir M., R. a. (2012). Numerical simulation of cooling a solar cell by forced Convection in the presence of nanofluid, . *sciverse science direct, 594-603*.

Sarafraz M.M., F. H. (2016). Heat transfer, pressure drop and fouling studies of multi-walled Carbon nanotube nano-fluids inside a plate heat exchanger,. *Experimental Thermal and Fluid Science,*.

Madhu, P., & Rajasekhar, G. (2017). Measurement of Density and Specific Heat Capacity of Different Nanofluids. *, International Journal of Advance Research, Ideas and Innovations in Technology*, 169.

Mahesh, V. K. (2016). Investigation of a New Flat Plate Collector Performance for Solar Water Heating System . *International Conference on Global Trends in Engineering, Technology and Management (ICGTETM-2016)* .

Malvi, C., Gupta, A., Gaur, M. K., Crook, R., & Dixon-Hardy, D. (2017). Experimental Investigation of Heat Removal Factor in Solar Flat Plate Collector for Various Flow Configurations. *International Journal of Green Energy, 14 (4). pp. 442-448. ISSN 1543-5075*.

Mangesh Thakare and M. V. Khot. (2016). Performance investigation of formed tubes of Different Geometry for a Flat-plate solar collector, . *International Journal of Current Engineering and Technology E-ISSN 2277 – 4106, P-ISSN 2347 – 5161,* .

Maouassi, A. (2017). Numerical study of nanofluid heat transfer SiO2, through a solar flat plate collector. *International Journal of Heat and Technology*, 8.

Mariappan, V. (2012). experimental investigation on thermophysiical property of Al2O3/DMAC nanofluids. *NSTI-nanotech*, 589.

Marjan, B. N., H. A., M., Sadeghi, O., & Swar, A. Z. (2017). Influence of nanofluids on The efficiency of Flat-Plate Solar Collectors (FPSC),. *E3S Web of Conferences 22, 00123 DOI: 10.1051/e3sconf/20172200123 ASEE17.*

Mohamed. (2016). Comparison between the parabolic and dish solar collectors by using MATLAB.

Jaydev, S. B. (2016). Experimental Investigation of Hybrid Nanofluid on Thermosiphon Type Wickless Heat Pipe Heat Exchanger Thermal Performance,. *IJARIIE- ISSN (O)-2395-4396, Vol-2 Issue-4,*.

Nang, K. C., Imtiaz, C., H.H., M., & H., A. (2016). Theoretical analysis to determine the efficiency of a CuO-water nanofluid based-flat plate solar collector for domestic solar water heating system in Myanmar. *olar Energy 155:608-619,DOI: 10.1016/j.solener.2017.06.055*.

Narasimhe, G., Gowda, B. B., & R.Chandrashekar. (2014). Investigation of Mathematical Modelling to Assess the Performance of Solar Flat Plate Collector. *International Journal of Renewable Energy Research , Vol.4, No.2*.

Natarajan, E., & Sathish, R. (2009). Role of nanofluids in solar water heater. *spring-verlaglondon limited 2009*.

Otanicar, T. P. (2010). Nanofluid-based direct absorption solar collector,. *J Renew Sustain Energy 2:033102,*.

Garrido P., R. B. (2004). *Int. J. Miner.Process., 73 (2–4), 131–144. DOI: 10.1016/S 0301-7516 (03)00069-3,* .

Proceedings of Energy Conference . (September 2002). *UNCC.* Addis Ababa.

Srivastav R, H.,, H., Balakrishnan, P., Saini, V., Kumar, D. S., Rajni, K. S., & Thirumalini, S. (2018). Study of Heat Transfer Characteristics of Nanofluids in an Automotiv Radiator,. *IOP Conference Series: Materials Science and Engineering,.*

Elansezhian R., & Vandaarkuzhali, S. (2014). Performance Evaluation of Air Conditioning System Using Nanofluids,. *Australian Journal of Basic and Applied Sciences,*.

Rajaeiyan, A. M.-M. (2013). comparison of sol geo and co precipitation methods on the structural properties and phase transformation of gamma and alpha aluminium oxide nanoparticles. *springer*, page 177.

Rehena, N., & M. A., A. (2015). Thermal performance of nanofluid filled solar flat plate collector. *International Journal of Heat and Technology 33(2):17-24,DOI: 10.18280/ijht.330203*.

Rehena, N., Salma, P., & MA Alim. (2014). heat transfer by nanofluids in solar collector,. *Science Direct procedia engineering 90 364-370*.

Irfan S., S., Mehdi, S. N., M.M, I., Mehar, A., & Kumari, N. L. (2015). Performance Analysis of Solar Flat Plate Collector,. *International Journal of Mechanical and Production Engineering, ISSN: 2320-2092, Volume- 3, Issue-5,*.

Rajasekaran S., M.Chandrasekar, & T.Senthil, K. (2015). Performance Analysis of Coated Solar Flat Plate Collector,. *International Conference on Energy Efficient Technologies for Automobiles (EETA' 15), Journal of Chemical and Pharmaceutical Sciences, SSN: 0974-211*.

Saleh, S., Meibodi, A. K., Hamid, N., Omid, M., & Somchai, W. (2015). Experimental Investigation on Thermal Efficiency and Performance. The Of A Flat Plate Solar Collector Using SiO2/ (EG)-Water Nanofluid,. *International Communications*.

Samuel, S. (2018). Enhancement of Performance of Thermal Solar Collectors Using Nanofluids,. *International Journal of Energy and Power Engineering, ; 7(1-1):*, 1-8.

Saravanan, S., & Krishna, N. (2016). Experimental investigation on the flat plate solar water heater with glass as absorber material . *International Journal of Engineering Trends and Technology (IJETT) – Volume-40 Number-3* .

Suhaib, U. I. (2014). Preparation, Sedimentation, and Agglomeration of Nanofluids,. *chemical engineering technology,*.

Sujit, K. V., Arun, K. T., & Durg, S. C. (2017). Experimental evaluation of Flat plate solar collector using nanofluids,. *Energy Conversion and Management 134 103–115*.

Tagliafico I.A., S. F. (2014). Dynamic thermal models and CFD analysis for flat plate thermal solar collectors – a review,. *Renew and Sust Energy Rev, Vol. 2, No. 30, pp. 526-537. DOI: 10.1016/J.RSER.2013.10.023.*

Thomas, T. (2011). Numerical simulation of solar flat plate collector. *International hellenic university*.

Tiwari, G. N. (2016). *Handbook of Solar Energy, Theory, Analysis and Applications.* Delhi New Delhi India: Indian Institute of Technology.

Tomas, M. (2009). Detailed Modeling Of Solar Flat-Plate Collectors With Design 1 Tool Kolektor 2.2,. *Eleventh International IBPSA Conference Glasgow, Scotland July 27-30,*.

Sankaranarayanan V., C.,, G., Iniyan, S., & Suresh, S. (2013). Performance of CuO/Water Nanofluid as Outer Fluid in the Tube in Tube Condensing Unit of Air Conditioner: Experimental Study,. *Journal of Nanofluids, Vol. 2,*, 213–220.

Xie, W. Y. (2011). "A Review on Nanofluids: Preparation, Stability Mechanisms, and Applications" . *Hindawi Publishing Corporation Journal of Nanomaterials, Volume 2012, Article ID 435873,*, 17 .

Hung Y.H. (n.d.). physical and thermal properties of metal oxides.

Hepbasli Z., S., R., S., M.A., S., A., & N.A, R. (2016). Energy and exergy efficiency of a flat Plate solar collector using pH treated Al2O3 nanofluid,. *Journal of Cleaner Production 112 3915e3926*.

Zhongyang, L., Cheng, W., Wei, W., & Gang, X. (2014). Performance improvement of a nanofluid solar collector based on direct absorption collection (DAC) concepts. *International Journal of Heat and Mass Transfer 75:262–271,DOI: 10.1016/j.ijheatmasstransfer.2014.03.072*.

Zhongyang, L., Cheng, W., Wei, W., Gang, X., & Mingjiang, N. (2014). Performance improvement of a nanofluid solar collector based on direct absorption collection (DAC) concepts,. *International Journal of Heat and Mass Transfer 75 262–271*.

APPENDIX

Table A8. Solar radiation on horizontal surface.

Years	Months											
	Jan	Feb	Mar	Apr	May	Jun	Jul	Aug	Sep	Oct	Nov	Dec
2014	7.30	7.25	6.03	6.69	6.34	6.17	6.76	6.88	6.81	7.16	7.21	7.29
2015	7.24	7.18	7.17	6.99	6.58	5.57	6.58	6.79	6.78	6.97	7.24	7.12
2016	6.59	7.22	7.15	5.58	6.17	6.09	6.85	6.94	6.88	7.16	7.25	7.29
2011	7.30	7.08	7.17	7.04	6.94	6.69	6.61	6.93	6.76	6.91	7.25	6.63
2018	7.26	7.15	6.87	5.97	6.31	5.98	6.10	6.03	6.74	7.05	7.19	7.27
Aver.	7.14	7.17	6.88	6.45	6.47	6.10	6.58	6.71	6.79	7.05	7.23	7.12

Table A9. Diurnal temperature variation for Adama, Ethiopia year 2018.

	Ambient Temperature for representative day's of the months											
time (hr)	17-Jan	16-Feb	16-Mar	15-Apr	15-May	11-Jun	17-Jul	Augst 16	15-Sep	15-Oct	14-Nov	10-Dec
0.00	17.3186	20.9728	20.6924	22.5103	20.4103	16.7661	16.1231	19.9728	19.7974	19.8128	23.8165	20.6023
1.00	16.9386	19.7782	20.1551	22.2229	19.9626	16.1058	15.5937	19.6782	19.4198	19.3189	23.3795	20.4188
2.00	16.5586	19.4836	19.6178	21.9354	19.5148	15.4456	15.0643	19.3836	19.0422	18.8251	22.9425	20.2353
3.00	16.1786	19.1890	19.0805	21.6480	19.0670	14.7853	14.5349	19.0890	18.6647	18.3312	22.5054	20.0519
4.00	15.7986	18.8955	18.5431	21.3605	18.6193	14.1250	14.0055	18.7944	18.2871	17.8374	22.0684	19.8684
5.00	15.4186	18.4598	18.0058	21.0731	18.1715	13.4648	13.4762	18.4998	17.9095	17.3435	21.6314	19.6849
6.00	15.0386	18.2056	17.4685	20.7856	17.7237	12.8045	12.9468	18.2052	17.5319	16.8497	21.1944	19.5014
7.00	14.6586	17.9999	16.9312	20.4982	17.2760	12.1442	12.4174	17.9106	17.1544	16.3558	20.7574	19.3145
8.00	14.2786	17.6211	16.3939	20.2107	16.8282	11.4840	11.8880	17.6160	16.7768	15.8620	20.3203	19.1345
9.00	14.9897	18.0957	17.1311	20.9331	17.2423	12.2017	12.3907	18.2342	17.2705	16.4897	20.8766	19.6716
10.00	18.6124	22.1066	21.2713	24.3488	19.9559	16.6008	15.6512	21.2876	20.0911	20.1124	24.0853	22.1298
11.00	21.9132	25.7610	25.0436	27.4610	22.4349	20.6089	18.6219	24.0697	22.6610	23.4132	27.0088	24.3697
12.00	24.6616	28.8039	28.1846	30.0523	24.4962	23.9462	21.0954	26.3862	24.8008	26.1616	29.4431	26.2346
13.00	26.6616	31.0228	30.4751	31.9420	25.9999	26.8394	22.8992	28.0754	26.3612	28.1616	31.2182	27.5946
14.00	27.7858	32.2629	31.7552	32.9980	26.8394	27.7399	23.9072	29.0195	27.2332	29.2858	32.2182	28.3547
15.00	27.9436	32.4375	31.9355	33.1468	26.9577	27.9315	24.0492	29.1524	27.3561	29.4436	32.3500	28.4617
16.00	27.1280	31.5346	31.0034	32.3778	26.3460	26.9411	23.3152	28.4650	26.7211	28.6280	31.6277	27.9083
17.00	25.3961	29.6171	29.0241	30.7449	25.0470	24.8381	21.7565	27.0052	25.3726	26.8961	30.0937	26.7330
18.00	21.5455	25.2217	24.3454	26.9501	22.0086	19.9722	18.3561	23.6442	22.9845	22.4134	26.5650	24.0139
19.00	20.7748	24.5953	23.9415	26.5051	21.6888	19.3626	17.5507	23.1929	22.6154	21.9751	26.0851	23.6732
20.00	20.0040	23.9688	23.5376	25.0602	21.3689	18.7531	16.7453	22.7415	22.1574	21.9751	25.6051	23.3326
21.00	19.2333	23.3423	23.1337	25.6152	21.0490	18.1436	15.9398	22.2901	21.6798	21.5368	25.1251	22.9920
22.00	18.4625	22.7158	22.7298	25.1702	20.7291	17.5341	15.1344	21.8387	21.1245	21.0985	24.6452	22.6514
23.00	17.6918	22.0894	22.3259	24.7252	20.4092	16.9245	14.3289	21.3874	20.7705	20.6602	24.1652	22.3108

Table A10. Nusselt number for water and Aluminum oxide.

		Nusselt number					Nu (%)			
Velocity	Reynolds number	3% Al_2O_3	2% Al_2O_3	1% Al_2O_3	water	10% Al_2O_3	10% Al_2O_3	1% Al_2O_3	2% Al_2O_3	3% Al_2O_3
0.0001	1.400	0.506	0.496	0.487	0.476	0.588	0.235	0.024	0.043	0.063
0.0005	6.990	0.747	0.736	0.726	0.718	0.823	0.146	0.011	0.025	0.040
0.001	13.980	0.980	0.978	0.971	0.953	1.058	0.110	0.019	0.026	0.028
0.005	69.910	1.771	1.751	1.742	1.722	1.852	0.075	0.012	0.017	0.028
0.01	139.820	2.097	2.083	2.076	2.067	2.191	0.060	0.004	0.008	0.015
0.018	251.680	2.350	2.334	2.322	2.291	2.439	0.065	0.014	0.019	0.026
Average	-	-	-	-	-	-	0.115	0.014	0.023	0.033

Table A11. Nusselt number for water and Copper oxide.

		Nusselt number					Nu (%)			
Velocity	Reynolds number	3% CuO	2% CuO	1% CuO	water	10% CuO	10% CuO	1% CuO	2% CuO	3% CuO
0.0001	1.400	0.510	0.500	0.490	0.480	0.650	0.359	0.020	0.050	0.068
0.0005	6.990	0.750	0.740	0.720	0.720	0.950	0.323	0.004	0.027	0.043
0.001	13.980	0.990	0.980	0.970	0.950	1.280	0.341	0.018	0.024	0.038
0.005	69.910	1.770	1.750	1.740	1.720	2.500	0.454	0.012	0.018	0.030
0.010	139.820	2.110	2.080	2.070	2.070	3.100	0.501	0.003	0.008	0.018
0.018	251.680	2.350	2.330	2.320	2.290	3.440	0.500	0.011	0.017	0.026
Average	-	-	-	-	-	-	0.413	0.011	0.022	0.041

Table A12. Nusselt number for water and Silicon oxide.

		Nusselt number					Nu (%)			
Velocity	Reynolds number	3% Si_2O	2% Si_2O	1% Si_2O	water	10% Si_2O	10% Si_2O	1% Si_2O	2% Si_2O	3% Si_2O
0.0001	1.400	0.485	0.481	0.477	0.476	0.552	0.161	0.003	0.011	0.019
0.0005	6.990	0.717	0.719	0.713	0.718	0.830	0.155	0.007	0.001	0.002
0.001	13.980	0.961	0.955	0.957	0.953	1.119	0.174	0.004	0.002	0.008
0.005	69.910	1.735	1.733	1.741	1.722	2.295	0.333	0.011	0.006	0.008
0.010	139.820	2.063	2.064	2.057	2.067	2.873	0.390	0.005	0.001	0.002
0.018	251.680	2.315	2.306	2.308	2.291	3.199	0.396	0.007	0.007	0.010
Average	-	-	-	-	-	-	0.268	0.002	0.004	0.007

Table A13. Nusselt number for water and Titanium oxide.

		Nusselt number					Nu (%)			
Velocity	Reynolds number	3% Ti_2O	2% Ti_2O	1% Ti_2O	water	10% Ti_2O	10% Ti_2O	1% Ti_2O	2% Ti_2O	3% Ti_2O
0.0001	1.400	0.504	0.493	0.485	0.476	0.618	0.300	0.019	0.037	0.061
0.0005	6.990	0.749	0.727	0.719	0.718	0.913	0.271	0.001	0.013	0.043
0.001	13.980	0.984	0.972	0.963	0.953	1.231	0.291	0.010	0.020	0.032
0.005	69.910	1.772	1.761	1.728	1.722	2.436	0.415	0.003	0.022	0.029
0.01	139.820	2.099	2.081	2.057	2.067	3.029	0.465	0.005	0.007	0.015
0.018	251.680	2.330	2.334	2.306	2.291	3.360	0.467	0.007	0.019	0.017
Average	-	-	-	-	-	-	0.368	0.005	0.032	0.033

Table A14. Experimental data

Experimental Result													
		T_{amb} in K during different testing fluids			T_{out} (K)			Q_{out} (W)			Collector Efficiency		
Time (hr.)	Radiation (W/m^2)	water	1% Al_2O_3	2% Al_2O_3	water	1% Al_2O_3	2% Al_2O_3	water	1% Al_2O_3	2% Al_2O_3	water	1% Al_2O_3	2% Al_2O_3
7:00am	178.45	292.35	292.35	292.35	294.85	294.90	294.95	36.06	36.78	37.50	72.16	73.61	75.05
8:00am	389.49	294.55	294.55	294.55	300.95	300.99	301.22	92.31	92.88	96.20	84.64	85.17	88.21
9:00am	606.47	298.65	298.65	298.65	301.65	303.35	303.80	43.27	67.79	74.28	25.48	39.92	43.74
10:00am	795.36	301.65	301.65	301.65	304.55	306.25	307.55	41.83	66.34	85.09	18.78	29.79	38.21
11:00am	924.06	302.85	302.85	302.85	306.55	310.75	311.85	53.36	113.94	129.81	20.62	44.04	50.17
12:00noon	969.71	303.05	303.05	303.05	306.65	310.95	312.25	51.92	118.27	132.69	19.12	43.56	48.87
1:00pm	924.06	303.45	303.45	303.45	312.40	315.75	319.25	129.08	177.40	193.27	49.89	68.56	74.70
2:00pm	795.36	300.38	300.38	300.38	305.69	308.35	309.00	76.54	114.90	124.28	34.37	51.60	55.80
3:00pm	606.47	300.51	300.51	300.51	304.39	303.00	303.45	56.06	35.97	42.46	33.01	21.18	25.00
4:00pm	389.49	299.87	299.87	299.87	302.29	302.00	302.45	34.83	30.70	37.20	31.94	28.15	34.11
5:00pm	178.45	298.52	298.52	298.52	299.62	299.77	299.80	15.83	17.99	18.42	31.68	36.01	36.87

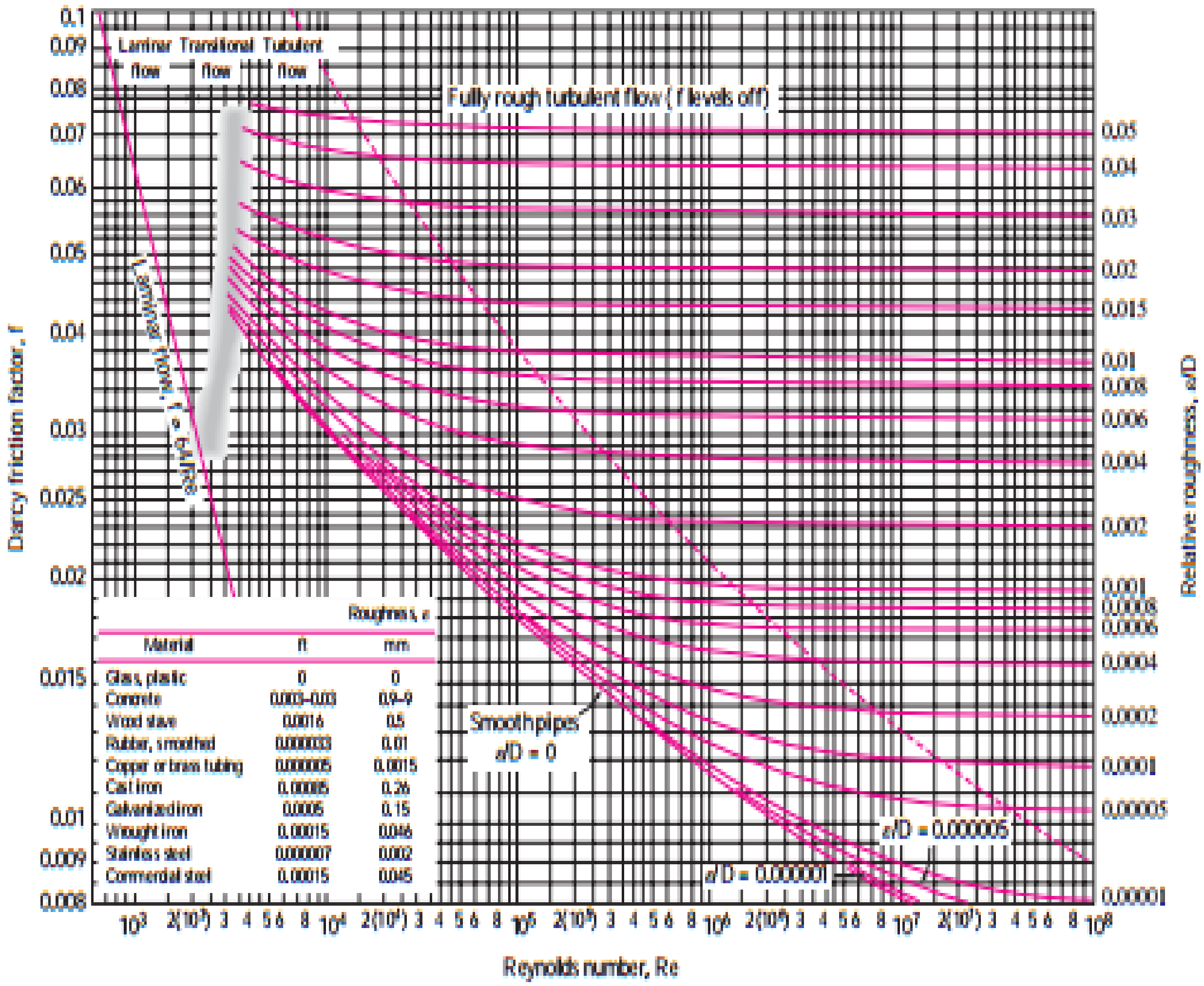

Figure A2 Darcy friction factor (***f***) graph